Report
P-19-10
June 2019

Experimental study of the transport properties of different concrete mixes

María Victoria Villar
Miguel García Gutiérrez
Beatriz Carbonell Barrios
Carlos Gutiérrez Álvarez
Rubén Iglesias Martínez
Pedro Luis Martín
Tiziana Missana
Manuel Mingarro
Jesús Morejón
Javier Olmeda
Andrés Idiart

SVENSK KÄRNBRÄNSLEHANTERING AB

SWEDISH NUCLEAR FUEL
AND WASTE MANAGEMENT CO

Box 3091, SE-169 03 Solna
Phone +46 8 459 84 00
skb.se

SVENSK KÄRNBRÄNSLEHANTERING

ISSN 1651-4416
SKB P-19-10
ID 1864466

June 2019

Experimental study of the transport properties of different concrete mixes

María Victoria Villar, Miguel García Gutiérrez,
Beatriz Carbonell Barrios, Carlos Gutiérrez Álvarez,
Rubén Iglesias Martínez, Pedro Luis Martín, Tiziana Missana,
Manuel Mingarro, Jesús Morejón

CIEMAT

Javier Olmeda, Andrés Idiart
Amphos 21 Consulting S. L.

Summary

Concrete will be used as the main construction material in SKB planned repository concepts for short- and long-lived low and intermediate level waste in Sweden. Concrete will also be one of the key engineered barriers to limit the release of radionuclides. Based on the experience acquired over the years in the SFR1 repository, SKB has recently developed a new concrete mix to improve short- and long-term performance of the concrete barriers. In the present study, concrete samples manufactured using this new mix and the previous concrete mix used in SFR1 are tested to determine their transport properties and other physical properties. Diffusion and permeability experiments were conducted at CIEMAT, Madrid (Spain), together with the characterization of other physical properties. These include porosity, pore size distribution, densities, and water content.

This report summarizes the main experimental results obtained during this experimental program between November 2017 and January 2019.

Sammanfattning

Betong utgör idag och kommer även i framtiden att utgöra det huvudsakliga konstruktionsmaterialet i SKB:s slutförvar för kort- och långlivat låg- och medelaktivt radioaktivt avfall i Sverige. Betong kommer även att utgöra en viktig komponent i de tekniska barriärernas förmåga att begränsa utsläpp av radionuklider. Baserat på de erfarenheter som förvärvats under de 30 år som slutförvaret för kortlivat radioaktivt avfall, SFR1, varit i drift har SKB nyligen utvecklat ett nytt betongrecept till förvarskonstruktionerna i den utbyggda delen av SFR, SFR3. I den föreliggande studien har transportegenskaper och andra fysikaliska egenskaper hos betongprover som tillverkats både enligt detta nya recept men även enligt det recept som användes vid uppförande av SFR1 undersökts. Arbetet genomfördes vid CIEMAT, Madrid (Spanien) och omfattade diffusions- och permeabilitetsexperiment samt karakterisering av andra fysikaliska egenskaper såsom porositet, porstorleksfördelning, densiteter och vattenhalt.

Denna rapport sammanfattar de viktigaste experimentella resultaten som erhållits under detta experimentella program mellan november 2017 och januari 2019.

Contents

1 Introduction

1.1 Background

In Sweden, low and intermediate level radioactive waste is being disposed of in the repository for short-lived low- and intermediate level radioactive waste, SFR, in Forsmark, in operation since 1988. An extension of SFR is planned to increase the storage capacity at the same site, named SFR3. SKB also plans for the construction of the repository for long-lived low and intermediate level radioactive waste, SFL, which will host legacy waste from the development of the Swedish nuclear programme as well as waste from decommissioning of the Swedish nuclear power plants. Concrete is used as the main construction material in both repository concepts and used as one of the key engineered barriers to limit the release of radionuclides. SKB has recently developed a new concrete mix to be used in the construction of the engineered barriers of SFR3. In the present study, concrete samples manufactured using this new mix and the previous concrete mix used in SFR1 are tested to determine their transport properties and other physical properties.

The concrete composition used in the 1BMA vault of the existing SFR repository was based on the use of CEM I Ordinary Portland Cement (OPC) from Degerhamn, referred to as Degerhamn Anläggningscement (SKB, 2001). The composition of the cement is given in Table 1-1.

The new concrete composition developed by SKB follows more modern standards. CEM I will still be used, but with the addition of a substantial amount of carbonate filler material. The development work of such composition is reported by Lagerblad et al. (2017). The development program undertaken by SKB comprised several activities, such as the investigation of the suitability of in-situ rock in SFR3 to be used as aggregates, concrete mix development on a laboratory scale and upscaling to concrete production plant scale, and the casting of large concrete structures representative of the concrete caissons for 2BMA.

The optimal concrete composition is detailed in Table 1-2. The w/c ratio is 0.49 and the concrete density is near 2 400 kg/m^3. A combination of commercially available filler materials (OmyaCarb 2GU and Myanit 10) is used. These filler materials are based on finely ground limestone (OmyaCarb 2GU) and dolomite (Myanit 10) with an average grain size of 2 and 8 μm respectively. In turn, the used cement (Degerhamn Plant cement) has an average size of ~20 μm. This composition is also in use for in-situ installation tests as Äspö HRL (Mårtensson and Vogt, 2019).

One important aspect of the proposed concrete mix is the control of the setting time. One of the effects of the addition of fine-grained carbonates is an acceleration of cement hydration reactions, leading to short setting times. This motivates the use of retarder as an admixture in the concrete mix. The amount of retarder that needs to be added depends on factors such as the distance between the concrete plant and the concrete pouring location, ambient temperature, or mixing water temperature (Mårtensson and Vogt, 2019). Two mixes were used in the in-situ work at Aspö HRL for Sections 1 and 2 (Mårtensson and Vogt, 2019), both following the composition in Table 1-2. The only difference was that the amount of retarder was increased in the second mix from 0.96 to 4.16 kg/m^3 of fresh concrete to avoid the problems associated with accelerated hydration of cement.

Table 1-1. Chemical and mineral composition of Anläggningscement (CEM I 42.5 N – SR 3 MH/LA). From Höglund (2001).

Component	Mass (weight %)
CaO	64
SiO_2	21
Al_2O_3	3.5
Fe_2O_3	4.6
MgO	0.7
K_2O	0.62
Na_2O	0.07
SO_3	2.2
Cl	< 0.1
Free $CaCO_3$	0.9
C_3S	64.4
C_2S	10.9
C_3A	2.5
C_4AF	13.9
$C\hat{S}H_2$	3.7
$CaCO_3$+$C\hat{S}H_2$	4.6
Alkalis, N+K	0.7

Table 1-2. Concrete mix design for Sections 1 and 2 (Mårtensson and Vogt, 2019).

Component	Commercial Product	Dosage (kg/m^3)	
		Section 1	Section 2
Cement	Degerhamn Anläggningscement	320.00	320.00
Limestone filler	Omyacarb 2-GU	130.00	130.00
Dolomite filler	Myanit 10	33.30	33.30
Water		156.80	156.80
Aggregates			
Size 16–22 mm		393.30	393.30
Size 8–16 mm		425.70	425.70
Size 4–8 mm		92.00	92.00
Size 0–4 mm		840.90	840.90
Additives			
Superplasticizer	Master Glenium Sky 558	1.30	1.30
Superplasticizer	Master Sure 910	1.70	1.70
Retarder	Master Set RT 401	0.96	4.16
Total		**2395.96**	**2395.96**

1.2 Origin of concrete samples

The samples tested in the present study have different origins. All of them were manufactured in Sweden and the hardened concrete specimens were sent to CIEMAT laboratories in Madrid (Spain).

1.2.1 Limestone-containing specimens

The first set of samples consisted of cylindrical concrete samples drilled from small cubes which were cast at Äspö HRL from the last trucks of Section 1 (ETAPP1 – Truck #7) and Section 2 (ETAPP2 – Truck #4) (Mårtensson and Vogt, 2019), see Figure 1-1. The concrete mixes of ETAPP1 and ETAPP2 samples correspond to that given in Table 1-2, with 0.96 and 4.16 kg/m^3 of retarder, respectively. The concrete in the small cubes was vibrated using a vibrating rod. Note that for the ETAPP1 specimens the concrete had started to set somewhat before casting of this cube and that the efficiency of the vibration therefore possibly not as required (Mårtensson and Vogt 2019). Right after drilling, all samples were wrapped in plastic and have been stored since then under controlled conditions at room temperature at the Swedish cement and concrete institute (CBI, Stockholm).

a) b)

Figure 1-1. *Small cube cast from concrete from truck #7 in Section 1 (a) after drilling of cores for further testing (ETAPP1), and from truck #4 in Section 2 (ETAPP2) (b).*

The third specimen was a drilled core (TAS05_09) from the wall cast at Äspö corresponding to Section 2 (Figure 1-2). Its composition is similar to the ETAPP2 specimens, i.e. with 4.16 kg/m^3 of retarder (Table 1-2). Vibration was done using a standard vibrating rod. However, vibration was not extensive as the concrete flowed very smoothly in the formwork (Mårtensson and Vogt, 2019).

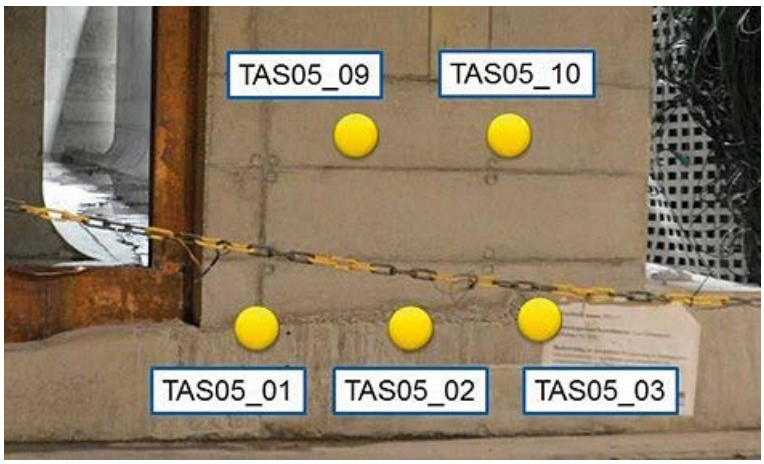

Figure 1-2. *Positions of the drilled cores (yellow circles, diameter of 10 cm). TAS05-09 and TAS05-10 drilled cores correspond to Section 2 (truck #2) concrete.*

1.2.2 OPC specimens

An OPC micro-concrete block with dimensions 25 x 25 x 10.5 cm (15.6 kg) was cast at Vattenfall R&D laboratories and cured under wet conditions for more than 1 month. The specimen was vibrated using a vibrating table. The micro-concrete composition is given in Table 1-3.

Table 1-3. OPC micro-concrete composition representative of the concrete in 1BMA but using smaller aggregates. The w/c ratio is 0.63. The mass of aggregates and superplasticizer is not specified.

Component	Commercial Product	Dosage (kg/m^3)
Cement	Degerhamn Anläggningscement	280.0
Water		176.4
Aggregates	Crushed granite	
Size 0–8 mm		1361.0
Size 4–8 mm		544.0
Additives		
Superplasticizer	Master Glenium Sky 823	3.1

Another OPC micro-concrete block cured for more than 1 month with reference BMA was produced by RISE/CBI. The concrete was vibrated in the mould placed on a vibrating table. The composition of this block is the same as the previous one (Table 1-3).

1.3 Objectives and scope

The main objective of this work is to experimentally determine the transport properties of different concrete types of interest to SKB. Transport properties include the effective diffusion coefficient of a neutral tracer, the hydraulic conductivity, the gas permeability, and the porosity and pore size distribution. Two different research groups of CIEMAT in Madrid (Spain) were in charge of the tests. One group focused on the through-diffusion tests and equilibrium porewater preparation, leaded by Miguel García Gutiérrez. The other group performed the rest of characterization work and sample preparation, leaded by María Victoria Villar.

1.4 Report structure

The report contains 9 chapters with the following content:

- Chapter 1: Introduction and background of the work presented in this report.
- Chapter 2: This section describes the different types of concrete samples studied and their preparation and conditioning.
- Chapter 3: Ultrasound analysis (only TAS 05_09 and BMA concrete samples).
- Chapter 4: Initial screening of the samples, including dimensions, density, water content and porosity determination.
- Chapter 5: Study of gas permeability.
- Chapter 6: Study of hydraulic conductivity.
- Chapter 7: Study of effective diffusion.
- Chapter 8: Presents the main outcomes and conclusions.
- Chapter 9: References.

Appendices A to E include additional information concerning the samples and diffusion data.

2 Materials

2.1 Reception of concrete specimens

2.1.1 ETAPP1 and ETAPP2 concrete

In November 2017, two boxes containing large concrete cylinders of Ø 10 x 40 cm were received at CIEMAT facilities (Figure 2-1 a–f). One of the boxes contained two ETAPP1 samples (PSU 17-4 170313 and PSU 17-6 170313) and the other one two ETAPP2 samples (PSU 17-2 170503 and PSU 17-4 170513). Both sets of samples are cores drilled from larger concrete cubes cast from the last truck of Section 1 and Section 2 concretes, as detailed in Mårtensson and Vogt (2019). ETAPP1 corresponded to the first casting carried out with the limestone concrete at Äspö HRL in Sweden (November 2016), whereas ETAPP2 came from the second casting (March 2017), in which more retarder was added as an admixture in the concrete mix to avoid rapid hydration of the concrete (for better workability). Upon visual inspection, concrete samples presented segregation, showing higher porosity in the upper half than in the lower one. Aggregates in ETAPP specimens presented particle size larger than 20 mm.

Figure 2-1. *ETAPP concrete samples in the original packing at the reception (a–b); appearance of the upper (c) and lower (d) sides of one ETAPP1 core; lateral view of ETAPP1 (e) and ETAPP2 (f) cylindrical samples.*

2.1.2 OPC micro-concrete

In January 2018, a prismatic OPC concrete block was received at CIEMAT facilities (Figure 2-2). The OPC specimen was made of a micro-concrete and had dimensions 25 x 25 x 10.5 cm (15.6 kg) containing crushed granite as aggregate with a maximum size of approximately 16 mm. It was cast on 16th November 2017 at Vattenfall R&D laboratories and cured under wet conditions until the day of transport.

2.1.3 TAS05_09 concrete

On 11th April 2018, a cylindrical concrete sample of Ø 10 x 50 cm with reference TAS05_09 was received at CIEMAT facilities. This core was horizontally drilled in a wall from Section 2 cast with limestone concrete in Äspö HRL (see Mårtensson and Vogt (2019) for more details). The sample was sent to CIEMAT in a wooden box protected by plastic bags (Figure 2-3 a). At first sight no significant cracks, voids or humidity signs were observed. Aggregate particle size was variable with diameters of approximately 3 cm max. The orientation of the core with respect to drilling was given by the indications "up, down, left, right and out/in", the outer surface being the smoothest one (Figure 2-3 b–d).

a) b) c)

Figure 2-2. *OPC block of approximately 25 x 25 x 10.5 cm wrapped in bubble plastic (a) and initial appearance (b–c).*

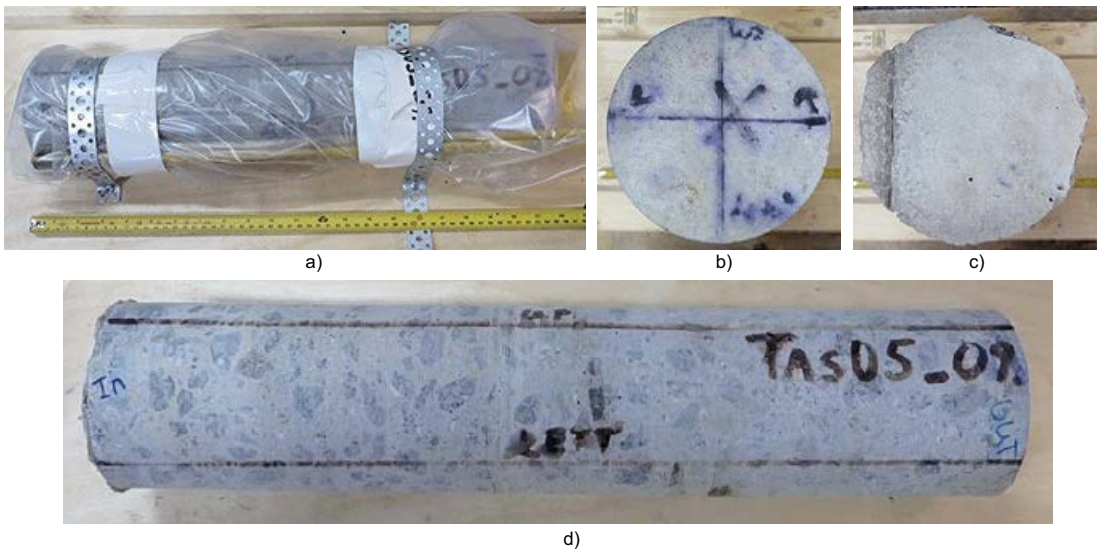

a) b) c)

d)

Figure 2-3. *TAS-05-09 concrete samples in the original packing at the reception (a); appearance of the outer (b) and inner (c) sides of the core; lateral view the cylindrical sample (d).*

2.1.4 BMA concrete

On 4th July 2018, an OPC micro-concrete block of 45 x 25 x 12 cm with reference BMA was also received. This sample was cast in May 2018 by CBI (Swedish Cement and Concrete Research Institute). The concrete block BMA came inside a wooden pallet wrapped with plastic bag. Sample surfaces were wet and presented water (Figure 2-4 a–b). The concrete block was obtained by cutting a larger concrete slab and thus the internal sides showed aggregates with a maximum diameter of ~2 cm (Figure 2-4 c).

Once the dimensions and weight of all the samples were measured, they were stored at constant temperature in a chamber of relative humidity (RH) of 80 ± 1 % with their original packaging to avoid moisture exchange. The total number of concrete samples received at CIEMAT facilities are summarized in Table 2-1, including the laboratory reference and the corresponding dimensions. Additional pictures of all the concrete samples are shown in Appendices A–D.

Table 2-1. Total of samples received at CIEMAT facilities.

Received reference	Lab. ref.	Cross-section dimensions (cm)	Height (cm)
ETAPP1. PSU 17-4 170313	ETAPP1-4	10.0 (Ø)	37.0
ETAPP1. PSU 17-6 170313	ETAPP1-6	10.0 (Ø)	37.5
ETAPP2. PSU 17-2 170503	ETAPP2-2	10.0 (Ø)	38.0
ETAPP2. PSU 17-4 170513	ETAPP2-4	10.0 (Ø)	38.0
OPC micro-concrete	OPC	25.0 x 10.5	25.45
TAS05_09	TAS	10.0 (Ø)	50.0
BMA concrete	BMA	43.0/47.5 x 26.5/27.5	13.0

a) b)

c)

Figure 2-4. *BMA concrete sample without packaging. Top (a) and lateral (b) view; appearance of the section of the sample BMA.*

2.2 Sample conditioning and preparation

2.2.1 ETAPP and TAS05_09 samples

Due to the large aggregate size, ETAPP1 and ETAPP2 concrete specimens were drilled to sub-cores of 50 mm in diameter to obtain representative sub-samples. Received cylinders were first transversally cut into two pieces using a water-refrigerated diamond disk (Figure 2-5 a–b). These half-cylinders were referenced as S and I, corresponding to the upper part of the core (S = sup with irregular surface) and the lower part (I = inf, with flat surface), and then drilled to 50 mm in diameter using a diamond drill bit (Hilti) and water as cooling agent (Figure 2-5 c) (tap water was used assuming that the leaching effect on the concrete samples is negligible given the short time of exposure). To keep the verticality of the ETAPP cores as well as to avoid any move during drilling, a cylindrical piece of metal crossed by 9 screws was used. Three screws in each level were used separated 120° and located at three vertically equally-spaced levels. The cylinder was drilled displaced from the core centre to keep a thicker zone to be used in potential future tests (Figure 2-5 d).

Cylinders were measured and weighed to obtain their bulk density (Section 4.2.1). Between tests, concrete sub-samples were stored at room temperature in a chamber with their original packaging to avoid changes in moisture content. One of the cores initially received was used for the diffusion tests and the other one for the rest of determinations (Figure 2-6 a–b).

The drilling remainders of the concrete samples were crushed with an iron mallet to grain size < 2 mm (Figure 2-6 c). The material was then quartered (Figure 2-6 d) and further ground to different grain sizes depending on its subsequent use (e.g. < 1 mm for the preparation of the equilibrium pore solution and < 0.4 mm for particle density determination).

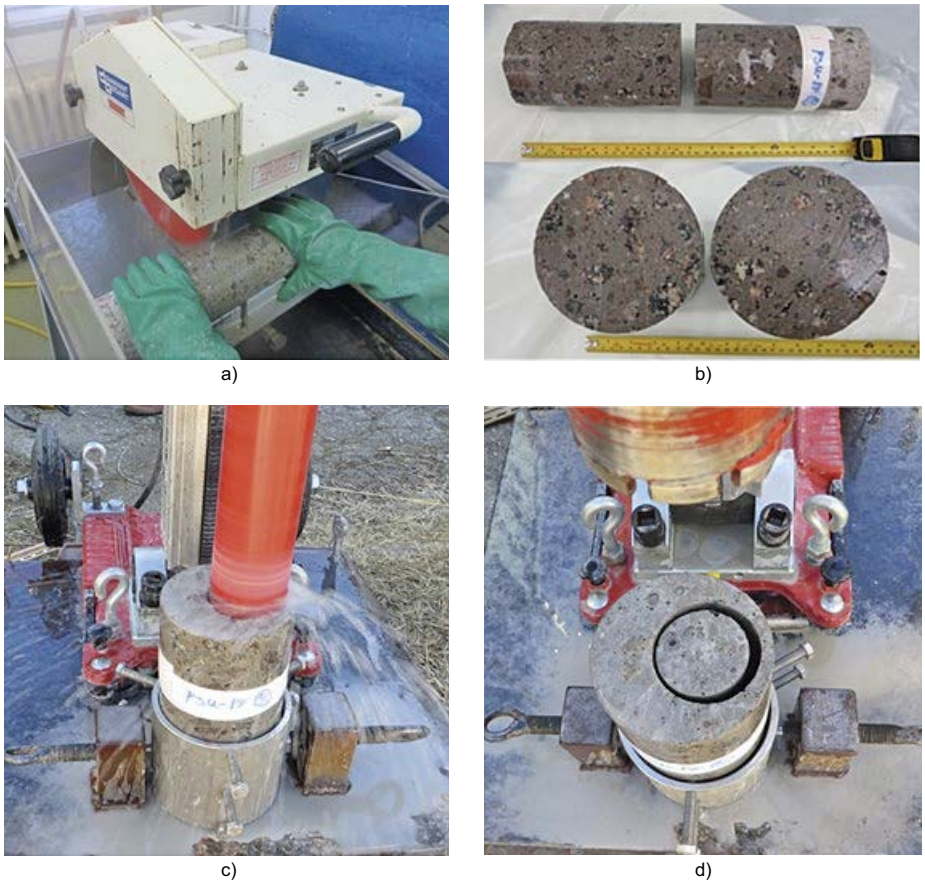

Figure 2-5. *Sample preparation: cutting ETAPP core into two pieces using a diamond disk (a–b); drilling of the ETAPP sub-cores by using a core drill bit (c–d).*

Figure 2-6. *Appearance of ETAPP1 (a) and ETAPP2 (b) cores and sub-cores after drilling. Grinding and quartering of the remainders after drilling (c–d).*

One of each ETAPP sub-cores was transversally cut in slices of 18 mm in height for the diffusion tests using a diamond disk saw (Figure 2-7 a). The other cores of each ETAPP sub-cores were transversally cut in thicker sections for gas and water permeability tests. Among these, sub-cores corresponding to the lower part of the original core were selected for gas and water permeability tests since they showed a lower quantity of large pores compared with sub-cores from the top part of the core (Figure 2-7 b–d).

Before cutting and sampling, ultrasound velocity tests were conducted on as-received TAS05_09 concrete samples to determine their homogeneity (see Section 3).

The TAS05_09 concrete core was transversally cut with a diamond saw using tap water as cooling fluid. Sub-samples of different size were obtained for different purposes. Figure 2-8 shows the appearance of the TAS05_09 sample, including a schematic view of the different cuts and tests conducted. External sides of the core (two slices of ~10 mm height) were used to prepare the pore solution in chemical equilibrium with the concrete sample for diffusion and permeability tests (Figure 2-8 c–d). These sections were selected to prepare the equilibrium solution because of their higher cement/aggregate ratio resulting from the skin effect of the formwork (Section 2.3). The inner sub-samples next to the external sides were used for dry density, water content, pore size distribution and particle density determination (Figure 2-8 e). After cutting, sub-samples for water content determination were dried for 24 h at laboratory conditions to evaporate the water from the cooling system from their surfaces. Sub-samples A, B and C were re-drilled to obtain sub-cores of 50 mm in diameter. The centre of the sample, section B in Figure 2-8 b, was selected to conduct diffusion experiments and sliced down to 6 sub-samples of 17.6–19.2 mm height (Figure 2-8 f). The other two sections, A and C in Figure 2-8 g–h, were used for gas and water permeability tests.

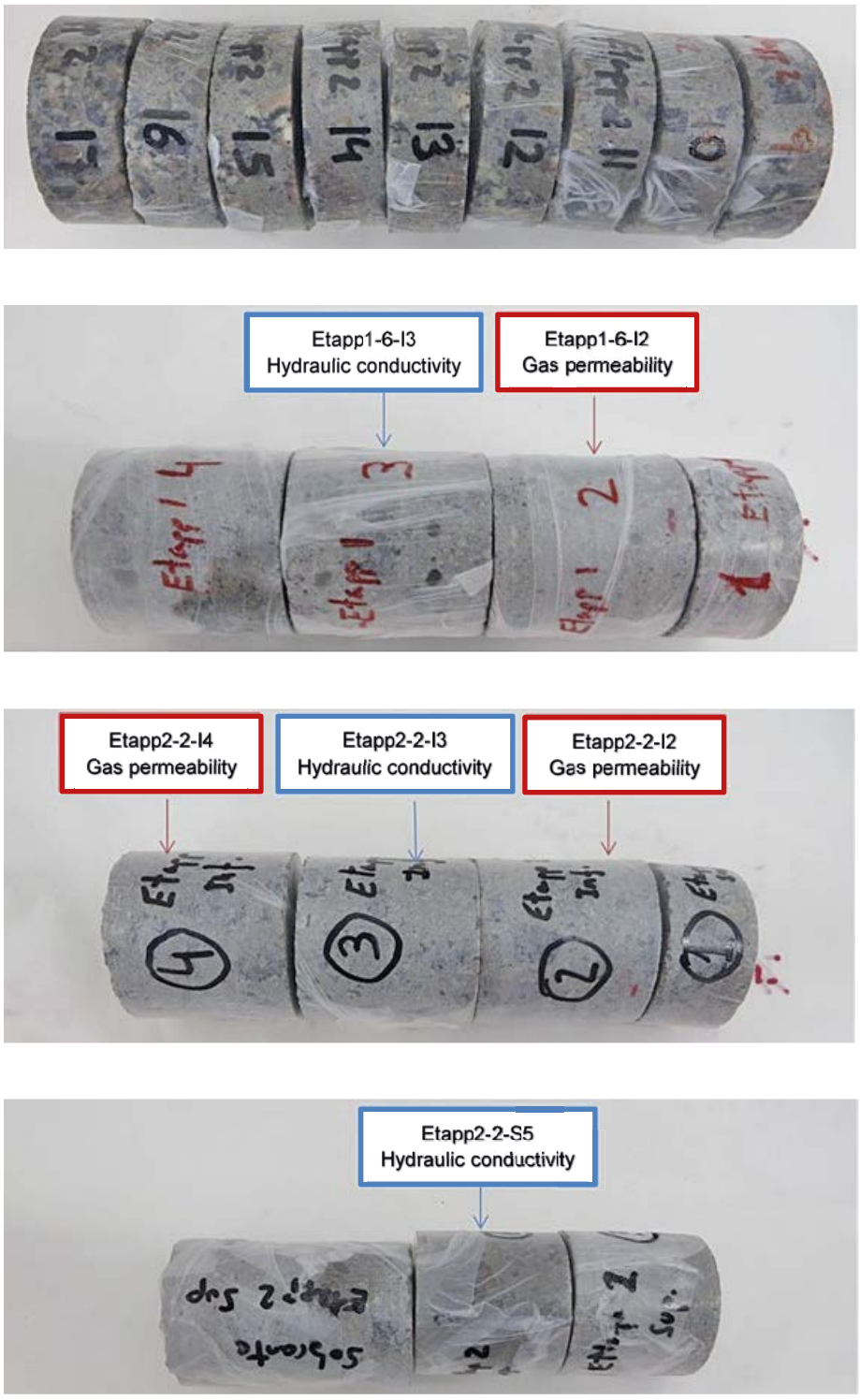

Figure 2-7. *Example of ETAPP sub-samples obtained for diffusion tests (a); Sub-samples from sub-core ETAPP1-6-I (sub-sample labelled as 1 was used for dry density and water content analyses) (b); Sub-samples from sub-core ETAPP2-2-I (sub-sample 1 was used for dry density and water content analyses) (c); Sub-samples from sub-core ETAPP2-2-S (d).*

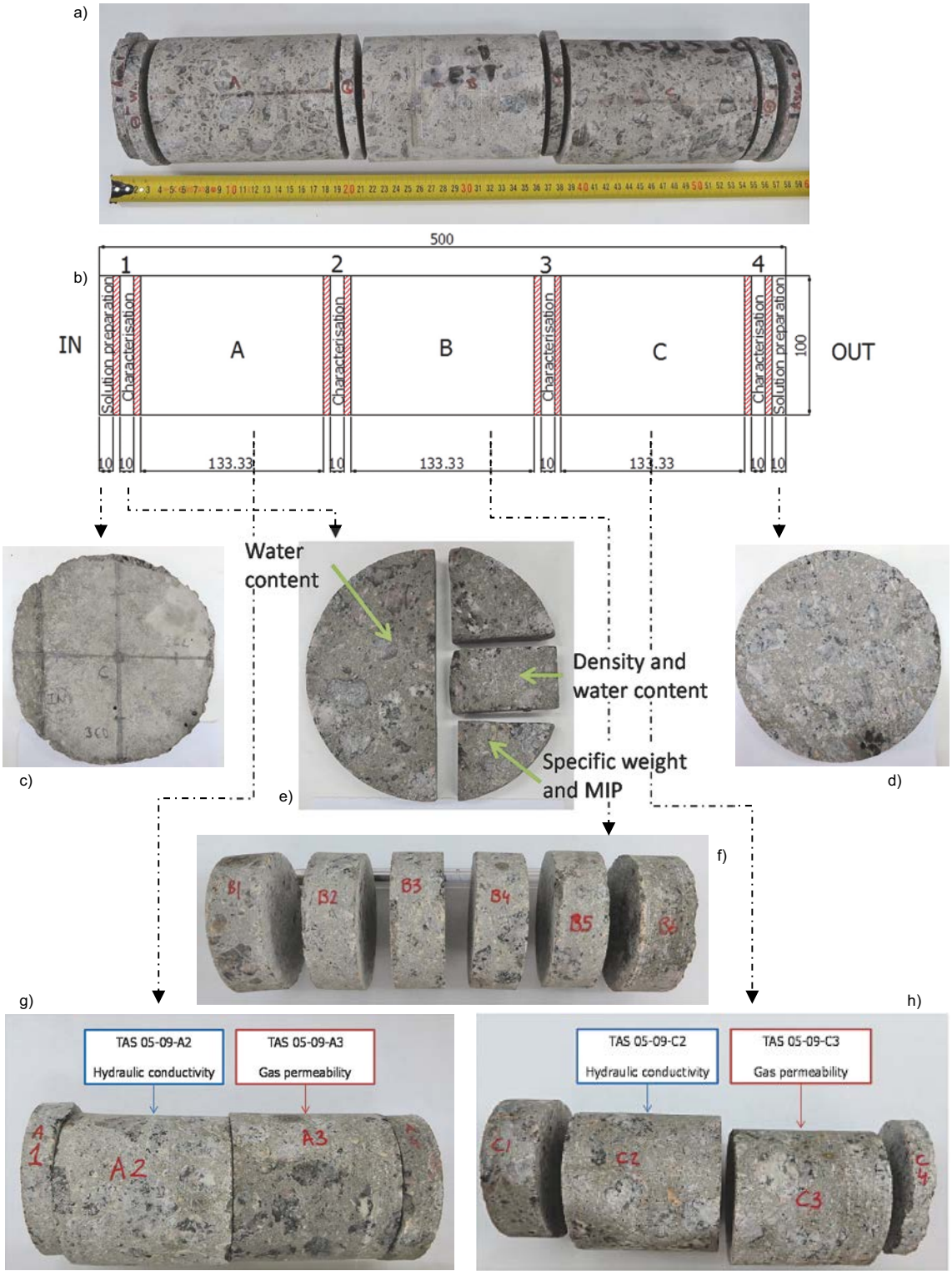

Figure 2-8. *TAS05_09 concrete core once sub-sampled (a); Distribution of sections for the different tests in core TAS05_09 (b); External sections for preparation of the equilibrium solution (c–d); Sub-sampling of a section for characterization (e); Sliced sub-samples from section B for diffusion tests (f); Sliced sub-samples from sections A and C for gas and water permeability tests (g–h).*

2.2.2 OPC and BMA concrete samples

Two cores of 50 and 38 mm in diameter were drilled for the OPC micro-concrete. The former was used for diffusion tests and the latter for the remaining analyses. Figure 2-9 a–c shows the drilling process and the final appearance of the Ø 50 mm core. Cylinders were carefully measured and weighed to obtain their bulk density (Section 4.2.1). Between tests, concrete sub-samples were stored at room temperature in a chamber with their original packaging to avoid changes in moisture content. The OPC sub-core (Ø 38 mm) was transversally cut in slices of different size for gas and water permeability tests. Sub-samples showing the least macro-porosity were selected for the permeability tests (Figure 2-9 d).

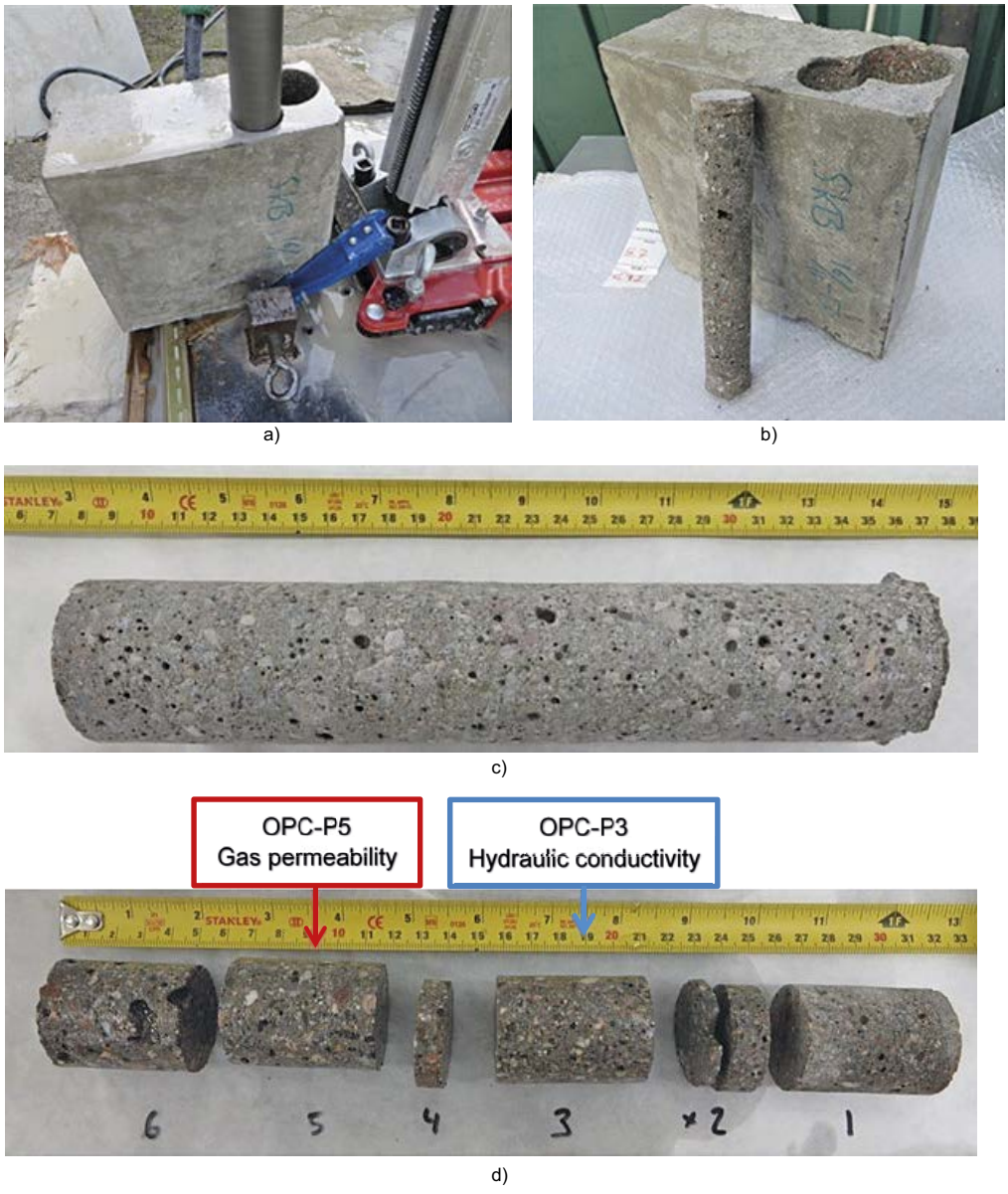

Figure 2-9. *Sample preparation: drilling of the OPC micro-concrete sub-cores by using a core drill bit with internal diameters 50 mm and 38 mm (a–b); appearance of Ø 50 mm drilled cylinder from the micro-concrete (c); sub-samples obtained from the OPC micro-concrete (OPC-38) (sub-samples labelled as 2 and 4 were used for dry density and water content analyses) (d).*

As with TAS05_09 sample, ultrasound velocity tests were conducted before cutting and sampling on as-received BMA concrete samples to determine their homogeneity (see Section 3).

Two cores were obtained by drilling the BMA concrete block with a Hilti machine using a diamond drilling crown of 50 mm in diameter and tap water as cooling fluid (Figure 2-10 a–b). The location of the two drilled cylinders is shown in Figure 2-10 c. The drilling totally crossed the block across its width. Core A, which was taken from the outer part of the block, was used for the diffusion tests and one dry density analysis, while core B was used for the physical and hydraulic characterisation (Figure 2-10 d).

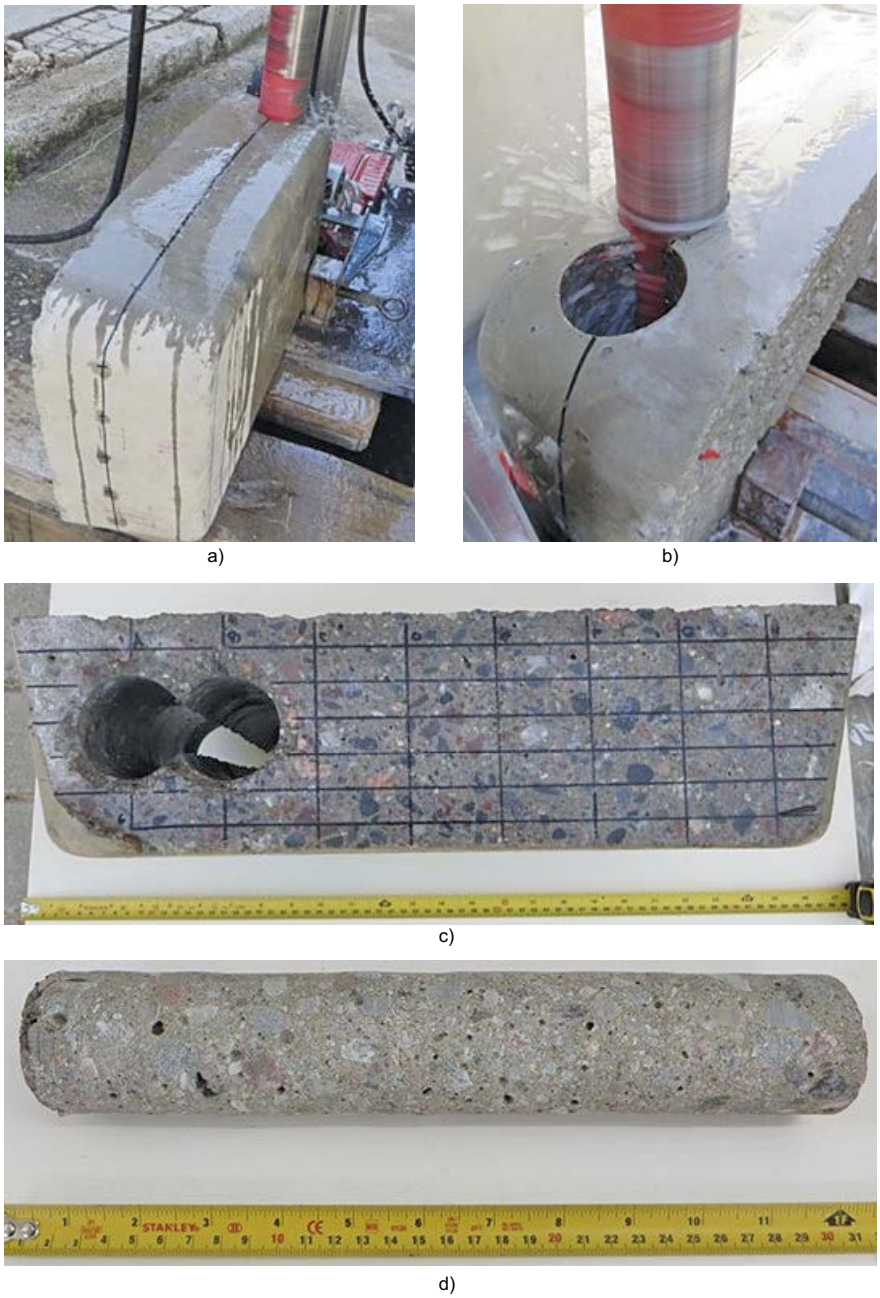

Figure 2-10. *Sample preparation: drilling of the BMA concrete block into two sub-cores by using a core drill bit with 50 mm of diameter (a–b); Location of cores A (left) and B (right) (c); Appearance of core B after removal of the excess of water from drilling (d).*

Sub-samples of both cores were obtained by cutting them transversally with a diamond disk using tap water as cooling fluid. Eleven indentical sub-samples were obtained from core A (Figure 2-11 a) and seven from core B. From the latter core, three of them with smaller size were used for dry density and water content determination (sub-samples 1, 2 and 3 in Figure 2-11 b), while sub-samples 4 and 6 for hydraulic conductivity and sub-samples 5 and 7 for gas permeability tests (Figure 2-11 b).

The external part of the BMA concrete block adjacent to core A was separated from the rest with a chisel and hammer (Figure 2-12). The central part of this fragment (circle in Figure 2-12 a) was crushed with an iron mallet to particle diameter < 2 mm. Then, with an automatic agate mortar, the material was ground to diameter size < 0.4 mm. This material was used for the particle density determinations and preparation of the equilibrium pore solution (Section 2.3). Additionally, four parts were taken from this fragment and reserved to be used in mercury intrusion porosimetry (MIP) tests (Figure 2-12 b).

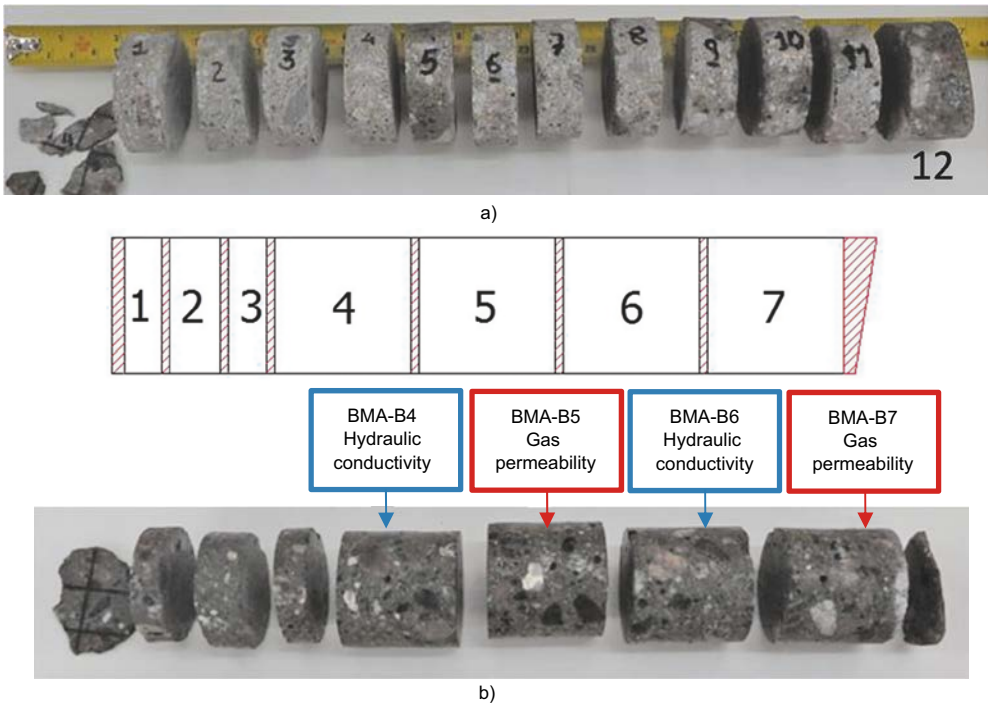

Figure 2-11. *Sub-samples of core A from BMA concrete for diffusion tests (Section 12 was used for density determination) (a); Schematic view of the different cuts and appearance of core B sub-samples for dry density and water content determination (1–3), for hydraulic conductivity (4 and 6) and for gas permeability (sub-samples 5 and 7).*

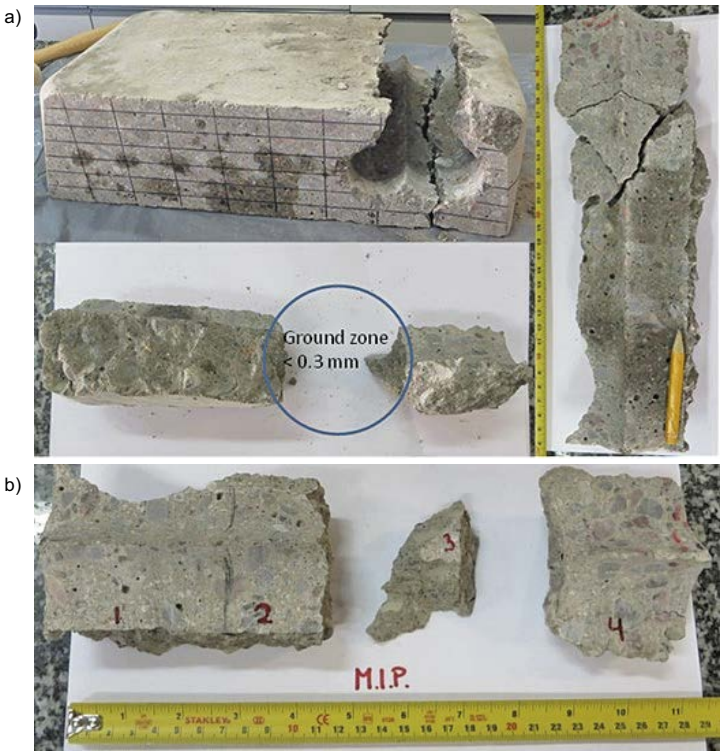

Figure 2-12. *Appearance of the BMA block after drilling and location of the ground area (a); selected fragments of the original concrete block for porosimetry (MIP) determination (b).*

2.3 Preparation of the equilibrated solution

Solutions in chemical equilibrium with concrete, representative of the concrete porewater, were used for saturating the samples and performing the diffusion and hydraulic conductivity tests. The equilibrated solutions for ETAPP1, ETAPP2, and OPC micro-concrete were obtained by contacting 20 g of crushed and ground (Ø < 1 mm) concrete into one litre of deionized and degassed water (DDW). For the TAS05_09 and BMA samples, 50 g of crushed (< 63 µm) concrete samples were contacted with one litre of DDW. When pH and electrical conductivities reached approximately constant values in time, the solution was considered in equilibrium with the solid. Figure 2-13 shows the pH evolution of the pore waters in equilibrium with concrete samples from ETAPP1 and 2, OPC micro-concrete, TAS05_09, and BMA samples.

Table 2-2 shows the chemical composition of the equilibrated solutions with ETAPP1 and 2 samples for 16 days, OPC micro-concrete sample for 25 days, TAS05_09 sample for 24 days, and BMA sample for 18 days. The equilibrium pore waters were stored in dark bottles in the glove box. Samples for diffusion experiments were saturated during ~20 days with their respective equilibrated solution prior to the start of the diffusion test.

Table 2-2. Chemical composition of the prepared equilibrated solutions (in mg/l).

Element (mg/l)	ETAPP1	ETAPP2	TAS05_09	OPC micro	BMA
Na	3.8	3.5	0.56	2.9	0.64
K	14	17	36	14	0.89
Ca	300	420	510	320	280
Mg	< 0.03	< 0.03	< 0.03	< 0.03	< 0.03
Fe	< 0.03	< 0.03	< 0.03	< 0.03	< 0.03
Al	0.85	0.64	0.99	0.75	2.30
Cl	0.65	0.36	2.70	0.73	< 1.00
SO_4^{2-}	8.2	9.3	7.8	6.2	3.5
CO_3^{2-}	26.6	23.5	32.5	31.6	61.8
SiO_2	< 0.03	< 0.03	0.34	< 0.03	1.52
Alk. (meq/l)	16.9	15.3	13.61	23.2	26.62
pH	12.36	12.39	12.40	12.39	12.40
Cond. (mS/cm)	3.75	4.27	3.80	4.42	5.48

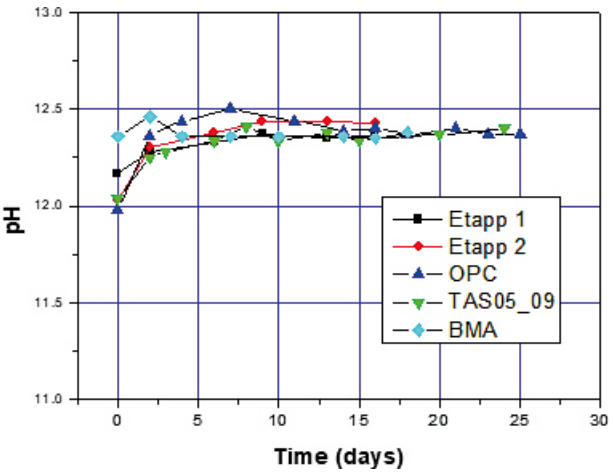

Figure 2-13. *pH evolution of the equilibrium solutions to be used for saturation of concrete samples.*

3 Ultrasound analysis

The homogeneity and quality of the concrete samples was additionally assessed by measuring the ultrasound velocity (UV) across them with a Steinkamp Ultrasonic Tester BP-5. Ultrasound testing is a non-destructive method based on the relation between the pulse velocity and the stiffness of the material. The sound velocity in concrete depends on its composition, compaction, stress state, internal structure, age and humidity, among other factors. Sound pulses across the concrete are strongly scattered because it is a heterogeneous material, and the ultrasound velocity across it is usually between 1.5 and 4.6 km/s. According to Wesche (1955), velocities between 2.5 and 3.2 km/s would correspond to low-strength concrete, between 3.2 and 3.7 km/s to average-strength concrete, between 3.7 and 4.2 km/s to high-strength concrete, and between 4.2 and 4.6 km/s to very high-strength concrete. Alcañiz-Martínez et al. (2015) proposed a concrete classification based on ultrasound velocity with values within the same ranges.

Note that these measurements were conducted on as-received TAS05_09 and BMA concrete samples and therefore prior to cutting and preparation of the concrete samples for further analyses (Section 2.2).

3.1 TAS05_09 limestone concrete

The ultrasound velocity (UV) was measured at 9 different positions along the length of the TAS05_09 core, i.e. diametrically opposed as initially marked on the core surface (along opposite lines left-right and up-down – Figure 3-1 a–b). Consequently, the distance between sensors during the measurements was 10 cm, i.e. the diameter of the sample. This falls in the limit of the minimum distance necessary for the wave length development and hence for a correct measurement.

The results show lower velocity towards the ends of the core but maintained at values between 2.36–2.42 km/s along most of the core. According to the classification proposed by Wesche (1955), these values fall within the range of a low strength concrete. Additionally, UV was also measured across the sides of the core, which corresponds to 50 cm distance (between points O, 3CU, 3CD, 3CR, 3CL and their opposite ones in Figure 3-1 b). The obtained values resulted to be all higher than 3.70 km/s, with an average velocity of 3.78 ± 0.01 km/s (from 5 measurements), corresponding to average/high-strength concrete. This is more in line with the compressive strength results presented by Mårtensson and Vogt (2019) for another drilled core from the same wall (TAS05_04), which showed an average value of 61.5 MPa.

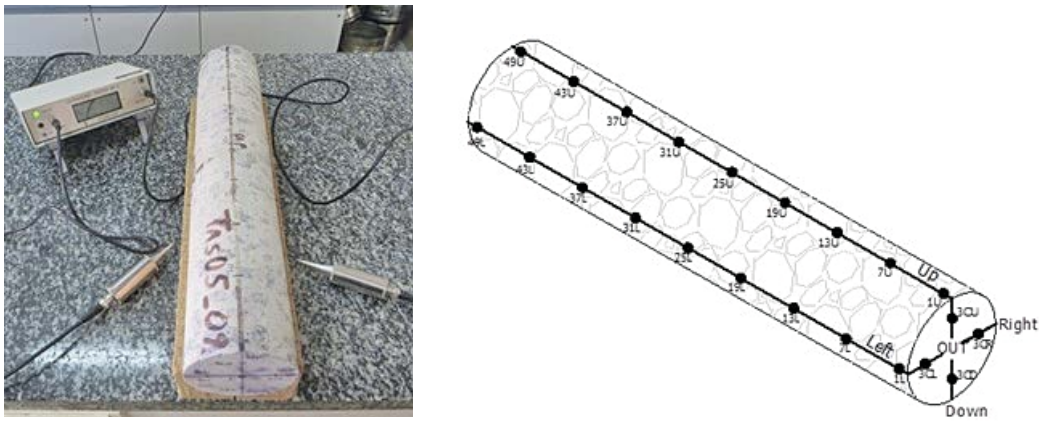

a) b)

Figure 3-1. *Ultrasound velocity device used for core TAS05_09 analysis (a); location of the measurement points along the sample (b).*

3.2 BMA concrete

The UV was measured in BMA concrete in two different directions. The first direction was across the cut surface (Figure 3-2), where perpendicular lines were drawn: A to H across the length (columns) and 1 to 6 across the height (rows). The UV was measured between the nodes of this mesh located at different distances along the same line. In addition, two measurements were made between cross nodes (1A-6H and 6A-1H) in the same pre-cut surface (Figure 3-2).

The second set of measurements were performed between opposite sides of the block (Figure 3-3 a–b), across the length and the width, placing the transducers on the perimeter line drawn at the middle height of the block (line 3 in Figure 3-2) and performing the measurement between opposite nodes, i.e. between A and A' to H and H' (across the width) and between I and I' to M and M' (across the length) (Figure 3-3 c).

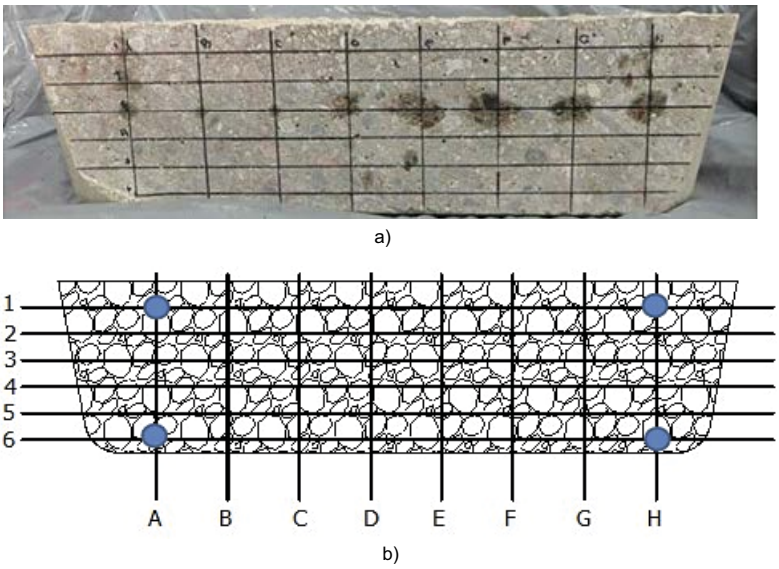

Figure 3-2. *Positions of UV measurements across the cut surface of the BMA block.*

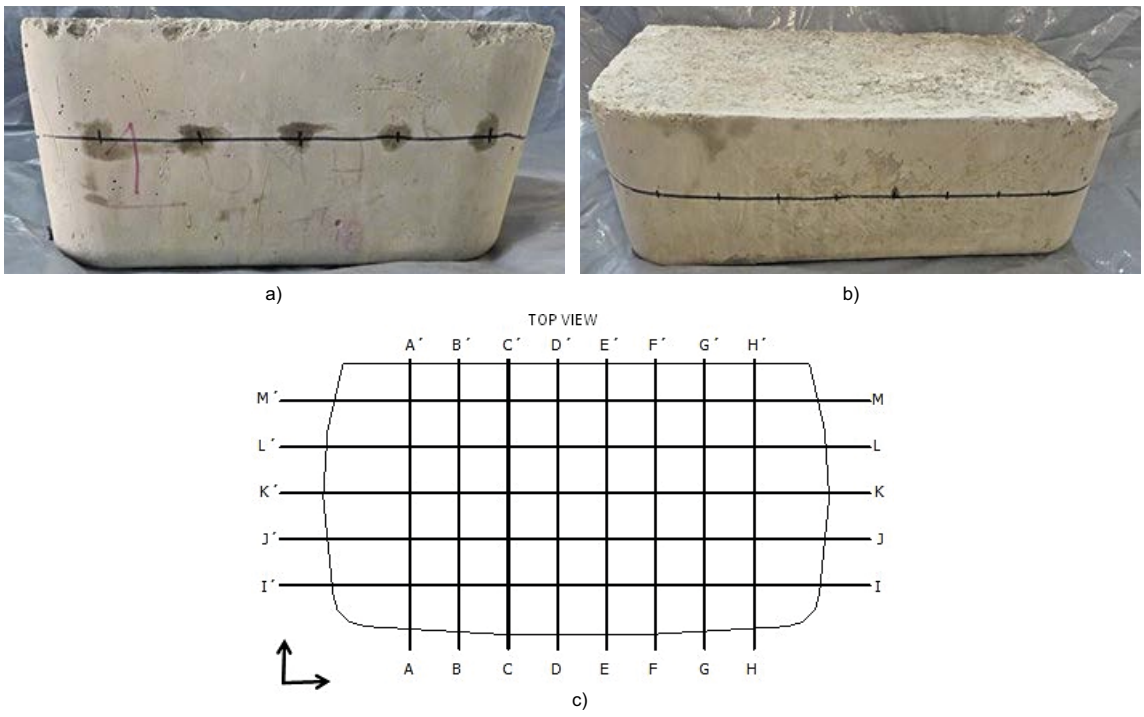

Figure 3-3. *Positions of UV measurements across the width and length of the BMA block (a–c).*

The results obtained from these two sets of measurements are shown in Figure 3-4 a–b. A gradual increase of velocity with increasing distance between nodes is observed, which could be explained by the increase of homogeneity for larger distances, since local inhomogeneities would have less weight on the results (Figure 3-4 a). For a given distance, the value obtained at different levels is very similar and only in a few instances significantly different values were obtained. These could not be related to any clear concrete feature.

Since the distances between measured dots are the same across the width and length of the sample, the results obtained in this case resulted to be the same (Figure 3-4 b). UV measurements performed across the length are slightly higher than across the width, since the distance between measurement dots is higher (~45 cm vs. ~27 cm). These values, close to 4 km/s, are considered more representative of the internal concrete characteristics than those taken on the cut surface shown above. The values obtained correspond to a high strength concrete. There is only one value clearly above the rest which cannot be related to any specific feature.

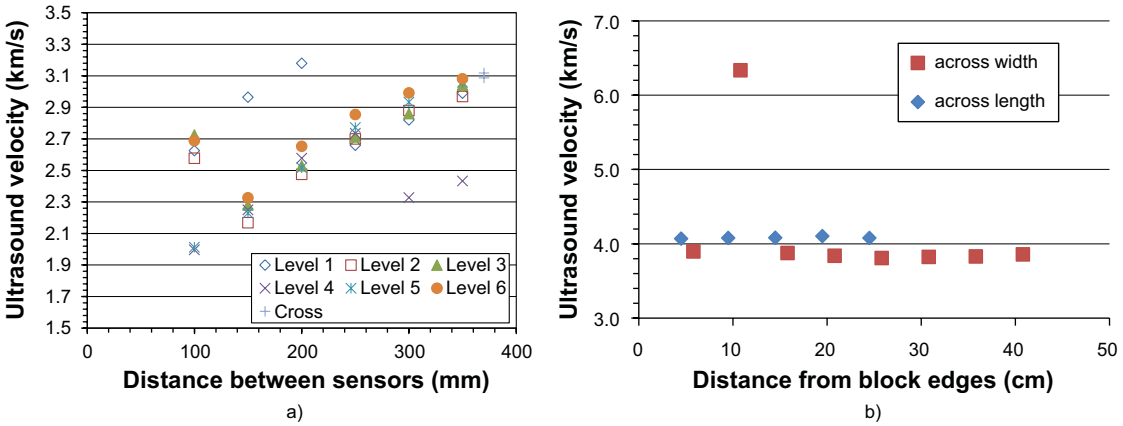

Figure 3-4. *Results of the ultrasound measurements taken from BMA block across the cut surface (a) and across the width and length (b).*

4 Initial screening

4.1 Theoretical considerations and formulae

4.1.1 Dry density, water content and particle density

The gravimetric water content (w) is defined as the ratio between the weight of water (M_w) and the weight of dry solid (M_s) expressed as a percentage (Equation 4-1). These weights were determined by oven drying at 110 ºC for 48 hours.

$$\boldsymbol{w = \frac{M_w}{M_s} \times 100} \quad (4\text{-}1)$$

The as-received bulk density (ρ) of the sub-cores and of some of the cylindrical sub-samples was determined by weighing the samples (M, in kg) including the as-received water content and measuring their volume (V, in m^3). The bulk density is defined as in Equation (4-2).

$$\boldsymbol{\rho = \frac{M}{V}} \quad (4\text{-}2)$$

Dry density (or apparent density, ρ_d) is defined as the ratio between the weight of dry sample and the volume (V) occupied by it prior to drying (4-3):

$$\boldsymbol{\rho_d = \frac{M_s}{V}} \quad (4\text{-}3)$$

Additionally, density of small sub-samples was determined by immersion in mercury. The volume of mercury displaced is obtained by weighing, assuming a mercury density of 13.6 g/cm^3. An additional water content determination was conducted on those sub-samples of already known volumes. A gram-scale model AND GF2000 was used, with a capacity up to 2 100 g and a precision of 0.01 g.

According to European Standard EN 1936 for determination of real density and apparent density, particle density (or real density) of a porous material (γ_s) is defined as the ratio between the weight of a given quantity of dry ground material (M_s) and its volume (V_s) (Equation 4.4). Particle density can be used to obtain the total porosity of a sample.

$$\boldsymbol{\gamma_s = \frac{M_s}{V_s}} \quad (4\text{-}4)$$

To obtain the particle (real) density, water and helium (He) pycnometers were used. With this technique, the weight of the displaced helium or water by a known weight of dry material is determined. Water pycnometry requires the use of deionized, de-gassed water for material suspension and pycnometers of capacity 50 cm^3. To determine this density, some fragments of the sub-samples were crushed with an iron hammer and further ground with iron pestle down to a maximum grain size of 2 mm. This ground sample was oven-dried at 110 °C during 48 h and ground again in an agate mortar to a maximum grain size of 0.4 mm. A helium pycnometer model Accupyc II 1340 was used. Three aliquots of the sample were prepared in the same way as described previously.

From the parameters determined according to previous equations, porosity ($\boldsymbol{\phi}$) and degree of saturation (S_r) can be obtained after Equations (4-5) and (4-6).

$$\boldsymbol{\phi = 1 - \frac{\rho_d}{\gamma_s}} \quad (4\text{-}5)$$

$$\boldsymbol{S_r = \frac{w \cdot \rho_d}{\phi \cdot \rho_w}} \quad (4\text{-}6)$$

where ρ_w is the density of water, assumed as 1 000 kg/m^3 in the calculations. It follows that in the case of water saturated samples ($S_r = 1$), porosity can also be estimated from Equation (4-6) as:

$$\boldsymbol{\phi = w \frac{\rho_d}{\rho_w}} \quad (4\text{-}7)$$

4.1.2 Porosity and pore size distribution

The pore size distribution of the concrete samples was determined by mercury intrusion porosimetry (MIP). This technique allows the determination of the pore size distribution by injecting mercury into the sample at different pressures while controlling the volume intruded. The pressure applied can be related to the minimum pore diameter intruded, considering the characteristics of the fluid. The ratio of the volume of mercury intruded (pore volume) to the applied pressure (which conditions the minimum pore diameter) allows distribution curves to be obtained, establishing the percentage of pores of a size included within a given range.

To minimize the alteration of the concrete microstructure during drying, the samples were put in an ice condenser of a Telstar LioQuest equipment at –50 °C for 3 hours. Subsequently, they were lyophilised for 19 hours at a temperature of –50 °C under a vacuum of 0.2 mbar to eliminate the water in the pores by sublimation. Before the MIP tests, the samples were heated to 35 °C for 2 hours in the lyophiliser and then placed in the penetrometer (i.e. the porosimeter sample holder). The porosimeter used was a Micromeritics AutoPore Series IV 9500, which allows the exploration of pore diameters between 0.006 and 600 µm. Prior to mercury injection, the sample was outgassed by applying a vacuum of 50 µm-Hg. Thereafter, the mercury injection pressure was increased from 2.7 kPa to 220 MPa in 109 steps. To determine the extrusion branch of the curve, the pressure was released in 56 steps down to a pressure of 68.6 kPa. A contact angle of mercury of 139° both on advancing and of receding on the material surface was considered.

Due to the inherent properties of mercury, this analytical technique allows to have access only to the macro-porosity (pore size > 50 nm) and part of the meso-porosity (pore sizes between 50 and 6 nm). Therefore, micro-porosity, i.e. with a pores size < 2 nm according to the classification by Sing et al. (1985), is not determined by MIP.

4.2 Results

4.2.1 Basic characterization

4.2.1.1 ETAPP samples

Once the as-received cores were cut in two parts, bulk densities (ρ) were calculated in the resulting sub-cores from weighing and measured dimensions. Additionally, bulk density of sub-samples obtained after re-drilling and cutting was also determined. Sub-samples were then dried to determine their water content and dry density. ETAPP sub-samples shown in Figure 2-8 b–c were transversally cut. The smallest part was used to determine the dry density by immersion in mercury, whereas the largest part was used to determine water content. The results are presented in Table 4-1.

Bulk density of ETAPP1 specimens ranges between 2 370 and 2 380 kg/cm^3, being comparable to 2 340–2 360 kg/cm^3 reported in Mårtensson and Vogt (2019) for the Truck #7 after 6 months of curing time. ETAPP2 bulk density values are between 2 360 and 2 430 kg/cm^3, which are also similar to 2 367–2 383 kg/cm^3 reported for the Truck #4 (Mårtensson and Vogt, 2019). In all cases, dry density determined in fragments by immersion in mercury was lower than that of the whole sub-core from which the fragment was taken. This probably reflects the heterogeneity of the material and the lack of representativity of the fragments used for dry density measurement, whose volume was between 10 and 20 cm^3. The values of density of solid particles as determined by water and He pycnometry are also included in Table 4-1. Significant differences are observed between the results of the two techniques, which can be attributed to the interaction between the ground concrete and the water, which could lead to dissolution/precipitation chemical reactions affecting the measurement (see Section 4.2.1.4). There could also be an effect of lack of representativeness of the samples used in these determinations. This is discussed in more detail in Section 4.2.1.4.

4.2.1.2 TAS05_09

The bulk density of the as-received TAS05_09 concrete sample is 2 430 kg/m^3, in agreement with the density range reported by Mårtensson and Vogt (2019) for the Section 2 Truck #2 (i.e. 2 380–2 420 kg/cm^3). From the four sections (1–4), water content, dry density and pore size distribution by MIP were measured. The material was prepared by mixing fragments of the four subsections for particle density determination. The dimensions and weights of the larger sections A, B and C were measured and the bulk densities (ρ) calculated.

Table 4-1. Characteristics of the ETAPP samples and obtained in subsamples.

Lab. reference	Height (cm)	Weight (kg)	ρ (kg/m³)	w [a] (%)	ρ_d [b] (kg/m³)	ρ_d [a] (kg/m³)	γ_s water [c] (kg/m³)	γ_s He [c] (kg/m³)
ETAPP1-4-S	18.50							
ETAPP1-4-I	18.20	3.4211	2 380				2760	2600
ETAPP1-6-S	18.85	3.5347	2 380					
ETAPP1-6-I	18.45	3.4441	2 370	6.8	2220	2120		
ETAPP2-2-S	18.80	3.4923	2 360					
ETAPP2-2-I	18.95	3.6313	2 430	4.1	2330	2310		
ETAPP2-4-S	18.70							
ETAPP2-4-I	19.05	3.6343	2420				2740	2600

a. Determined in a sub-sample; b. Deduced for the whole core from the w determined in a sub-sample; c. Averaged values from 3 measurements.

The results are presented in Table 4-2, including particle density obtained by water and He pycnometry, and plotted in Figure 4-1 a–b. TAS05_09 sample tends to contain more water and higher density towards the inner part of the specimen. As observed with ETAPP and OPC micro-concrete samples, significantly different solid density values are obtained between the two techniques. Results from water pycnometry systematically show higher values. This is discussed in more detail in Section 4.2.1.4.

Table 4-2. Water content and densities of the sub-samples of TAS05_09 concrete.

Ref.	Distance from inside (cm)	*w* (%)	ρ (kg/m³)	ρ_d (kg/m³)	γ_s water (kg/m³)	γ_s He [a] (kg/m³)
1	1.8	3.5	2490	2410	2720 ± 30	2592 ± 1
2	17.1	4.6	2450	2350		
3	32.1	4.0	2350	2260		
4	48.2	3.6	2380	2290		
A	9.4		2430			
B	23.3		2410			
C	40.3		2420			

a. Average of 3 sub-samples.

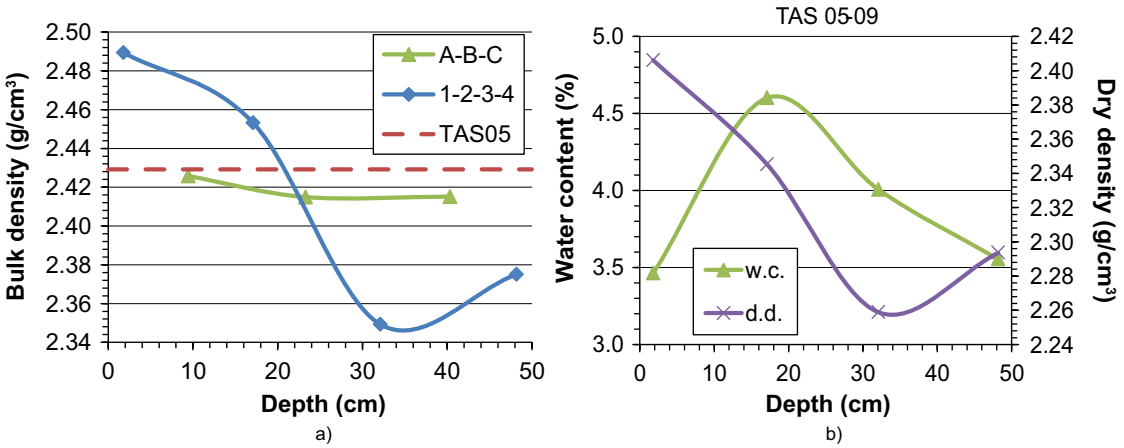

Figure 4-1. *Bulk density of TAS05_09 sub-samples obtained from weighing and dimensions measurement (A-B-C) and immersion in mercury (1-2-3-4). Dashed red line indicates the average bulk density of the as-received sample (a); Water content and dry density measured in TAS05_09 sub-samples 1-2-3-4.*

4.2.1.3 OPC and BMA samples

The bulk density of the as-received OPC and BMA blocks was not determined due to their large size and irregular shape (Table 2-1). However, as detailed in Section 2.2.2, two cores of 50 and 38 mm in diameter were drilled for the OPC micro-concrete and two cores of 50 mm were drilled from the as-received BMA block, from which bulk densities were obtained. Table 4-3 lists the dimensions, weights and calculated bulk densities from both BMA cores.

Table 4-3. Characteristics of the cores drilled from BMA block.

Reference	Length (cm)	Diameter (cm)	Weight (kg)	Bulk density (kg/m^3)
BMA Core A	27.72	5.05	1.3218	2380
BMA Core B	27.90	5.05	1.3232	2370

Core B was sliced down in 7 sections (Section 2.2.2) and bulk density of sub-samples 1, 2 and 3 (Figure 2-11 b) was determined by mercury immersion. Then, these sub-samples were oven-dried to determine their water content and calculate the dry density. Sub-sample 12 from core A (Figure 2-11 a) was also used for dry density and water content determinations. The results are summarized in Table 4-4. The higher bulk density of sample 12 from core A could be attributed to higher cement/aggregate ratio (samples from the outer part of the BMA block).

Table 4-4. Water content and densities of BMA concrete sub-samples obtained by mercury immersion and oven drying.

Sample Ref.	ID	Depth (cm)	*w* (%)	ρ (kg/m^3)	ρ_d (kg/m^3)
BMA Core B	1	1.2	5.5	2380	2260
	2	3.1	5.7	2360	2230
	3	5.0	5.7	2350	2230
BMA Core A	12	26.3	4.7	2410	2300
OPC-38	-	-	6.0	2350	2110

Additionally, all the sub-samples obtained from cores A (sample 12) and B were measured and weighed to determine their bulk density. Dry densities for sub-samples 1, 2, 3 and 12 were already obtained from their dry weight. For the rest of sub-samples, calculated dry densities were obtained by assuming a water content of 5.63 % for the whole BMA block (Table 4-5), which is the averaged value of the water content acquired from the 3 sub-samples (Table 4-4). Note that some uncertainty is attributed to these values, which assume that the water content is homogeneous within the sample. Again, results from He pycnometry are lower than the ones corresponding to water pycnometry (see Section 4.2.1.4).

Bulk densities obtained by the different methods are plotted in Figure 4-2. In general, the density of most of the sub-samples is below the average bulk density of the two cores obtained from their dimensions. Also, the bulk densities obtained by immersion from sub-samples 1, 2 and 3 are higher than those obtained from their dimensions. The fact that the samples contained cavities (large voids) in which mercury can intrude during immersion is a reasonable explanation for this difference, since the volume measured would be then consequently smaller than that obtained from the external dimensions of the sub-samples.

Table 4-5. Densities of BMA sub-samples obtained from dimensions and by water and He pycnometry.

Sample Ref.	ID	Distance to out (cm)	ρ (kg/m^3)	ρ_d (kg/m^3)	γ_s water (kg/m^3)	γ_s He [a] (kg/m^3)
BMA Core B	1	1.2	2290	2170	2730	2556 ± 3
	2	3.1	2290	2170		
	3	5.0	2230	2110		
	4	8.6	2320	2190[b]		
	5	13.9	2310	2190[b]		
	6	19.2	2320	2200[b]		
	7	24.5	2380	2250[b]		
BMA Core A	12	26.3	2430	2320		
OPC-38	-	-	2350	2210	2750	2600

a. Average of three sub-samples, b. Approximate value.

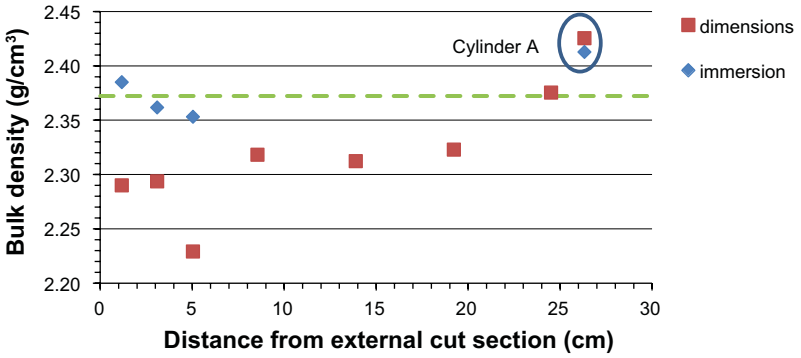

Figure 4-2. *Bulk densities of BMA cores A and B obtained by different methods. Dashed green line stands for the average bulk density of the two cores obtained from their dimensions.*

4.2.1.4 Assessment of particle (real) density

The density of solid particles has been determined by two methods, i.e. water and He pycnometry. The value obtained using water was systematically higher than that obtained with He. The fact that the concrete ground sample may react with water leading to mineral reactions, could be the reason for this difference. These differences have been observed in the past, and several researchers measured lower particle densities when using He as fluid in the pycnometer compared to water (e.g. Taylor, 1997 and references therein). Furthermore, the values obtained with He generally tend to be lower than the actual ones when materials with very small pores are tested. This discrepancy is relevant since the calculation of porosity relies upon particle density values, as described by Equation (4-5).

As an alternative to pycnometer results, particle density values were computed from the hydraulic conductivity tests (Section 6). The degree of saturation of the samples after the hydraulic conductivity tests should be close to 100 % (samples were saturated by injecting water during long time periods). Hence, the particle density of each sample was computed by considering that the final degree of saturation in Equation (4-6) at the end of the hydraulic conductivity tests should be 100 % (i.e. Equation 4-7). Combining Equation 4-5 with Equation 4-7 and after some algebra gives

$$\gamma_s = \frac{\rho_d}{1 - w\frac{\rho_d}{\rho_w}} \qquad (4\text{-}8)$$

The variables in this equation are water content, dry density and liquid density, which can be properly measured. In this way, a solid density can be calculated. Table 4-6 summarizes the obtained densities from all the studied concrete specimens by water and He pycnometry, and calculated from the hydraulic conductivity tests. As can be observed, particle (real) density thus obtained is generally comprised between the two values measured by water and He pycnometry.

Table 4-6. Summary of particle (real) densities (kg/m³) obtained in the present work for all the studied concrete samples.

Sample	γ_s water (kg/m³)	γ_s He (kg/m³)	γ_s computed (kg/m³)
ETAPP1	2760	2600	2670
ETAPP2	2740	2600	2650 ± 20
TAS05_09	2720 ± 30	2592 ± 1	2700 ± 10
OPC micro-concrete	2750	2600	2600
BMA concrete	2730	2556 ± 3	2620 ± 10

4.2.2 Porosity and pore size distribution

Intruded porosity and pore size distribution of ETAPP, TAS05_09, OPC and BMA concrete samples were determined by mercury intrusion porosimetry (MIP). Some fragments of the selected sub-samples were lyophilized according to the procedure described in Section 4.1.2. Between 1.0 and 4.5 g of material was placed in the penetrometer to carry out the analysis (the penetrometer volume ranged between 3.5–4.2 ml).

Figure 4-3 depicts the intrusion curves and Table 4-7 summarizes the total intruded porosity as well as the pore size distribution for all the studied specimens. The majority of the pore volume corresponds to diameters below 100 nm for ETAPP samples (Figure 4-3 a–b). The two signals at high pressures (5×10^4–10^5 nm) corresponding to ETAPP2 are not related to inherent porosity but also to an experimental artefact resulting from the change from the low to the high-pressure chamber of the porosimeter. This explains why the total intruded porosity of this sample is higher than the value of ETAPP1 (Table 4-7). For TAS05_09 sample, two different pore size families can be clearly observed in the spectra, whose separation could be approximately set around the pore size 1 000 nm (Figure 4-3 c–d). Macropores (4.6×10^5 nm) and mesopores (10–200 nm) size is similar for all the tested sub-samples. In general, the highest contribution to total porosity comes from the pores larger than 1 000 nm (Table 4-7). This great volume of large pores is not common in concrete and can partly be attributed to the conditioning of the sub-samples.

The pore size in the OPC sample covers a broader range (Figure 4-3 a–b). The peaks between 4 500 and 6 200 nm observed in the three curves are probably due to an experimental artefact during the measurements. BMA sub-samples present a similar spectra with most of the pores with a size below 1 000 nm (Figure 4-3 e–f). Three of the samples also presented pores in the upper pore size range. In general, the percentage of pores smaller than 1 000 nm corresponds to > 75 % for all the sub-samples studied (Table 4-7).

Table 4-8 comparatively shows the porosity obtained by MIP (intruded porosity) and the total porosity estimated from dry density and solid particle (real) density (Equation 4-5) for all the studied concrete specimens. Porosity values obtained from MIP analysis are generally lower since this technique cannot account for micropores and inaccessible pores. For ETAPP2 and TAS05_09_4 samples, the reasons of obtaining higher MIP porosity than the ones obtained by density measurements can be attributed to some artefact during analysis and/or the sample conditioning. It is important to note that MIP results can be affected by several factors such as sample preparation, forms and types of sample, sample drying and rate of pressure application, among others. For instance, it is reported that concrete fragments including coarse aggregate give higher porosity than the ones with lower-sized aggregates or with no aggregate, due to the ITZ between aggregate and mortar, which results to be more porous (Laskar et al., 1997; Kumar and Bhattacharjee, 2003; Ma, 2014).

Table 4-7. Total intruded porosity and pore size distribution obtained by MIP for all studied concrete samples (sizes correspond to diameters).

Reference	Porosity (–)	ϕ < 1 000 nm (%)	ϕ > 1 000 nm (%)
ETAPP1-4-I	0.130	84	16
ETAPP2-4-I	0.146	73	27
TAS05_09_1	0.152	57	43
TAS05_09_2	0.134	33	67
TAS05_09_3	0.116	40	60
TAS05_09_4	0.244	26	74
OPC	0.092	71	29
BMA-1	0.129	82	18
BMA-2	0.109	87	13
BMA-3	0.112	80	20
BMA-4	0.121	76	24

Table 4-8. Summary of porosities obtained by MIP and calculated from densities in the present work for all the studied concrete samples. Porosity estimated from particle (real) density obtained from hydraulic conductivity tests.

Sample*	Intruded porosity (–) From MIP	Total porosity (–) From Densities
ETAPP1	0.130	0.166
ETAPP2	0.146	0.140
OPC micro-concrete	0.092	0.168
TAS05_09	0.162	0.133
BMA concrete	0.118	0.172

*Averaged values.

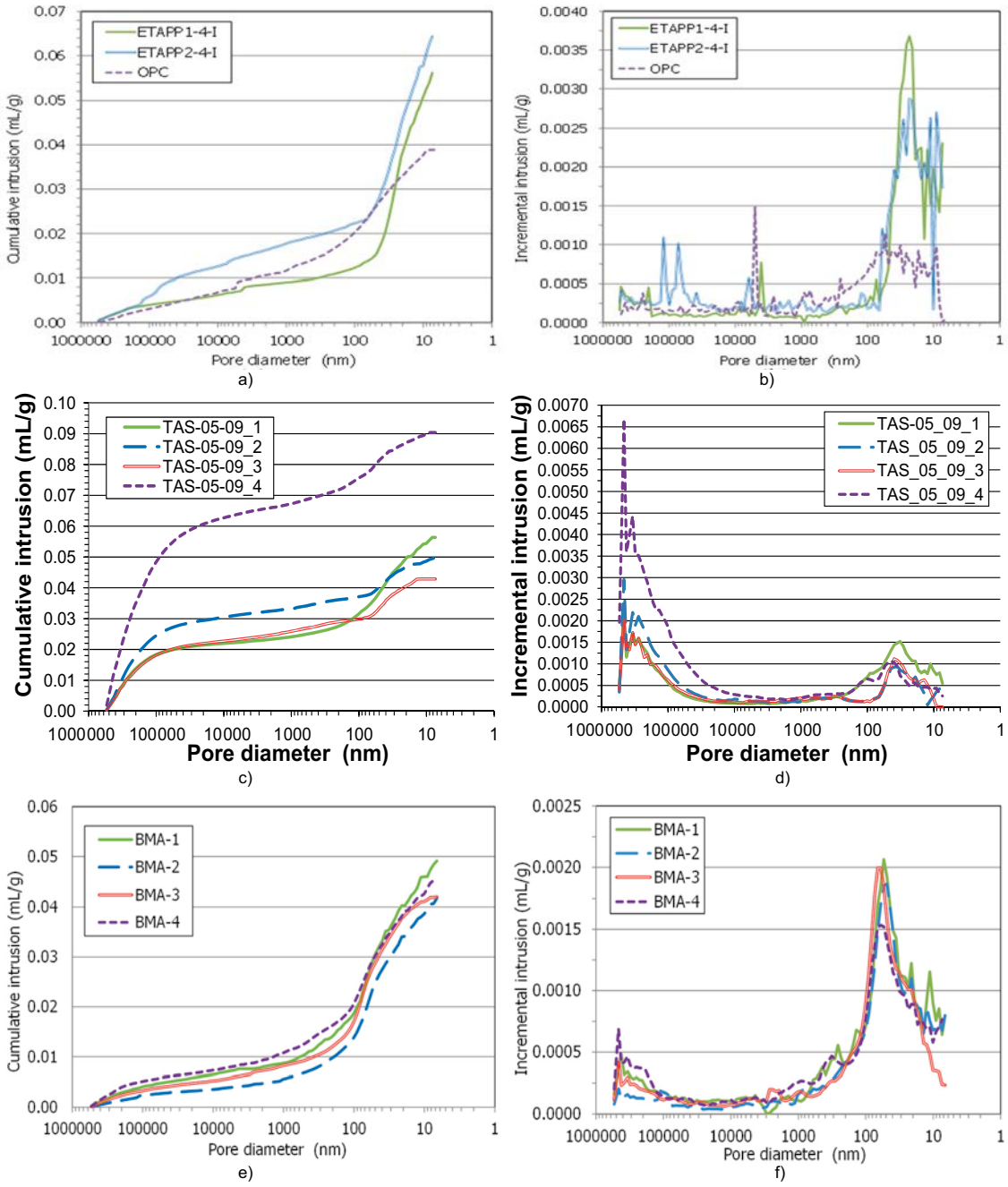

Figure 4-3. *Cumulative and incremental intrusion curves obtained by MIP for ETAPP and OPC (a–b), TAS05_09 (c–d), and BMA samples (e–f).*

5 Gas permeability

5.1 Experimental method and analytical approach

The first set of samples received, i.e. ETAPP concrete and OPC micro-concrete samples, were tested with the as-received water content. The degree of saturation was therefore not uniform between different samples. Thus, it was decided to test the second set of samples, i.e. TAS05_09 and BMA block, after drying to constant mass. To this end, specimens were oven-dried at 60 °C until their weight was stabilized (weight changes were monitored every 24 h until the difference between consecutive values was lower than 0.1 %). Drying at 60 ºC has been previously used by other researchers to condition the samples for gas permeability measurements (e.g. Meziani and Skoczylas, 1999; Benachour et al. 2008; Chen and Skoczylas, 2010). Then, samples were placed inside a desiccator with silica gel to cool down and remain dry (Figure 5-1). This temperature was selected as a compromise between not affecting too much the microstructure (which may affect its transport properties) and being able to remove as much water as possible from the samples. Still, 60 ºC was not enough to completely remove water from the samples, which still contained some water after drying and during the gas permeability measurements.

For this reason, the intrinsic permeability could not be directly obtained from the gas measurements performed (to determine this parameter with gas, the sample must be completely dry, i.e. 0 % water content). When there are two fluids present in the porous material (gas and water in this case), permeabilities of each fluid depend upon their degree of saturation: these are called effective permeabilities. Hence, the value obtained in the determinations (besides gas permeability, k_g) is the intrinsic permeability measured with gas flow, k_{ig}, multiplied by the relative permeability to gas, k_{rg}. In turn, the relative permeability to gas is the ratio between the permeability at a given saturation point (the one measured in these tests) and the *absolute* permeability at total gas saturation (i.e. total absence of water), where k_{rg} would be equal to 1. A summary of the notation used is presented in Table 5-1.

Table 5-1. Notation and units used for gas permeability.

Notation	Unit	Description
k_g	m/s	Gas conductivity
k_{g0}	m^2	Gas permeability of the dry material
k_{ig}	m^2	Intrinsic permeability deduced from gas flow
k_{rg}	-	Relative permeability to gas (k_g/ k_{g0})
$k_{ig} \cdot k_{rg}$	m^2	Effective gas permeability

a) b)

Figure 5-1. *Samples dried in the oven at 60 °C (a) and sample placed in a desiccator with silica gel (b) before the gas permeability tests.*

Two different experimental setups (permeameters) were used to determine the gas permeability, a low-pressure (LP) and a high-pressure (HP) device. The LP equipment does not allow to measure very low permeabilities (below ~10^{-18} m^2). Thus, a first trial was made for each sample with the LP equipment and then the same sample was measured in the HP permeameter. Measurement in the LP equipment is customarily done because it is a cross-check of the values obtained in the HP equipment, which gives confidence to the whole set of results. The latter also allows to analyse the effect of boundary conditions, such as gas injection pressure (P_i) and confining pressure (P_c), on measured gas permeability. The LP permeameter (Section 5.1.1) works under unsteady-state conditions (falling-head) and only pressure is measured. The HP permeameter (Section 5.1.2) works under steady-state conditions and both pressure and gas flow are measured.

In the two setups the sample was tested placed in a triaxial cell. The cylindrical concrete sample was placed between two filter papers and porous stones on top and bottom. All pieces were joined using parafilm and duct tape. Then, the sample was wrapped in two latex membranes, between which vacuum grease was applied to prevent gas losses (Figure 5-2). Nitrogen was used in both setups because it is safe and does not react with the materials tested. Additionally, its density solely depends on the pressure applied in the range of pressures used in the test.

The assemblage was mounted in a triaxial cell with walls made of methacrylate and reinforced with hose clamps with capacity to withstand pressures of up to 3 MPa (Figure 5-3 a). The cell had three inlets drilled in the base: for the sample top drainage/backpressure, for the sample bottom injection pressure (P_i), and for the confining pressure (P_c). To increase the confining pressure over 3 MPa in some cases, an extra reinforced system was designed to ensure the physical integrity of the cell (Figure 5-3 b).

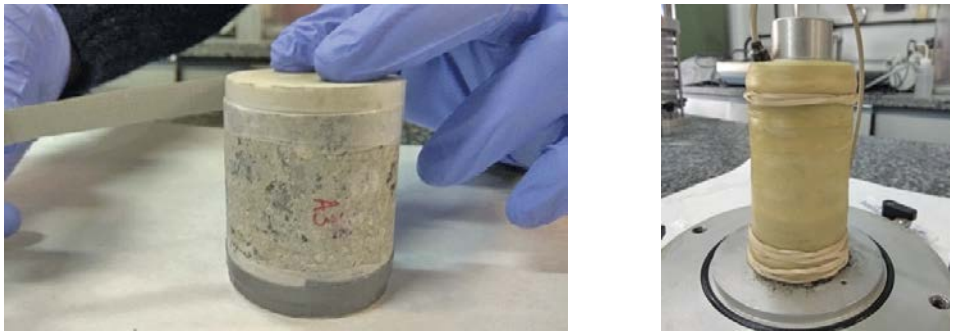

a) b)

Figure 5-2. *Example of concrete sample placed between filter paper and porous stones (a) and wrapped in double latex membranes (b).*

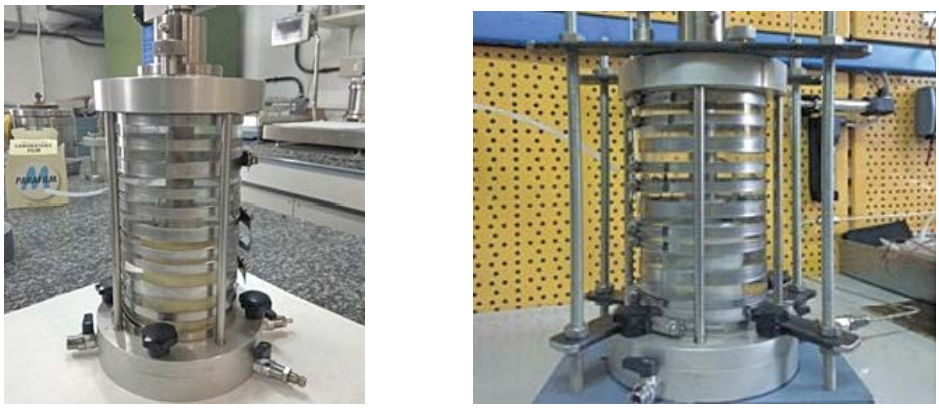

a) b)

Figure 5-3. Triaxial cell used for gas permeability tests (a) and extra reinforced system for high-pressure equipment (b).

5.1.1 Low-pressure equipment (LP)

Once the triaxial cell was filled with water, a confining pressure high enough to ensure perfect adherence of the membranes to the surface of the sample was applied to the chamber of the triaxial cell (initially 0.6 MPa). The inlet at the lower part of the sample was connected to an airtight tank of known volume, in which nitrogen gas was injected at a pressure slightly higher than atmospheric pressure. The tank was instrumented with a pressure sensor connected to a data acquisition system which recorded the pressure of the fluid contained inside (in relative values). The outlet at the upper part of the sample was left open to the atmosphere. The test consisted in allowing the air in the tank to go out to the atmosphere through the specimen, while the decrease in pressure in the tank was measured as a function of time. The tests were performed at room temperature. Prior to every new permeability test, the airtightness of the system was checked. A schematic view of the LP equipment is shown in Figure 5-4.

The effective permeability to gas was calculated with the equation proposed by Yoshimi and Osterberg (1963):

$$k_{ig} \cdot k_{rg} = 2.3 \frac{V \cdot L \cdot \mu_g}{A\left(P_{atm} + \frac{P_0}{4}\right)} \cdot \frac{-\log_{10}\left(\frac{P(t)}{P_0}\right)}{t - t_0} \quad (5\text{-}1)$$

where $k_{ig} \cdot k_{rg}$ is the effective permeability to gas (m^2), V the volume of the tank (m^3), L the length of the sample (m), A the surface area of the sample (m^2), μ_g the dynamic viscosity of nitrogen (1.78×10^{-5} Pa·s), P_{atm} the atmospheric pressure (Pa), P_0 the excess pressure over atmospheric pressure at time t_0 (s), and $P(t)$ the excess pressure over atmospheric pressure in the tank at time t. This equation is analogous to that used for the expression of permeability to water using a falling-head permeameter, the air continuity equation being applied through consideration of compressibility (Lloret Morancho 1982). In this equation, it is assumed that the initial P_0 pressure is relatively small compared to atmospheric pressure. It is also assumed that, while pressure is decreasing in the tank, the distribution of pressure in the sample is the same as would exist if this instantaneous pressure had been maintained in the tank for a long period of time. The pressure of the tank on test initiation, P_0, was fixed to values close to 0.103 MPa (relative pressure). The volume of the spherical tank used was 2.21×10^{-2} m^3 and the gas used was nitrogen. A density of nitrogen (ρ_g) of 1.12 kg/m^3 was considered, corresponding to the usual pressure and temperature conditions in the laboratory. The relation between gas conductivity (k_g, m/s) and the product of intrinsic permeability measured with nitrogen gas (k_{ig}, m^2) times the relative permeability to gas (k_{rg}) is:

$$k_g = \frac{\rho_g \cdot g}{\mu_g} \cdot k_{ig} \cdot k_{rg} = 6.2 \cdot 10^5 \cdot k_{ig} \cdot k_{rg} \quad (5\text{-}2)$$

In the LP equipment, samples were tested at 0.6 and 1.0 MPa of confining pressure. Subsequently, the cell with the sample was moved to the HP equipment.

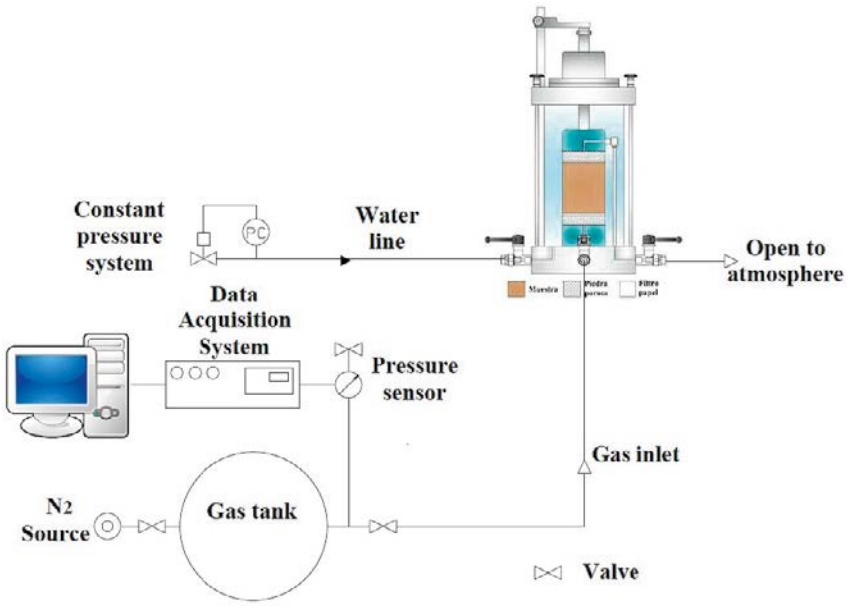

Figure 5-4. *Schematic representation of the low-pressure (LP) gas permeability system.*

The relative error (uncertainty of measurement compared to the measurement itself) of the effective permeability measured in the LP equipment ($k_{ig} \cdot k_{rg}$) represented in Equation (5-1) has three main components. These variables, from higher to lower importance are pressure, dimensions of the sample, and time (Table 5-2). The relative error of the effective gas permeability values in the LP equipment was lower than ±10 %, resulting from the combination of the relative uncertainties of the measured variables.

Table 5-2. Uncertainty of variables measured in the LP setup.

Variables	Instrument	Uncertainty (%)
Pressures: *P(t)* and P_0	Pressure sensor	± 0.1 %
Dimensions: *L* and *A*	Caliper	± 0.07 %
Time: *t* and t_0	PC	± 0.003 %

5.1.2 High-pressure equipment (HP)

The experimental setup is schematically represented in Figure 5-5. Tests were performed by keeping constant confining (P_c) and injection pressures (P_i) and atmospheric backpressure, i.e. following the working principle of a steady-state (constant-head) permeameter. With the HP equipment, P_i could reach 18 MPa and P_c could be increased up to 16 MPa. To compute the effective permeability the gas outflow was used, applying the following equation for incompressible media with compressible pore fluids (Scheidegger, 1974):

$$k_{ig} \cdot k_{rg} = \frac{Q_m \cdot \mu_g \cdot L \cdot 2P_m}{A \cdot (P_{up}^2 - P_{dw}^2)} \quad (5\text{-}3)$$

In this type of test, Q_m (m^3/s) is the mean volume flow rate measured by the appropriate flowmeter, P_m is the standard atmospheric pressure (0.101325 MPa) due to the standard temperature pressure (STP) conditions of the gas mass flowmeters, P_{up} is the gas injection pressure (P_i) and P_{dw} is the backpressure (actual atmospheric pressure in this setup). All gas pressure measurements in this equipment were done in *absolute* values. The outlet of the cell connected to the bottom of the sample was open to atmosphere, with a series of different range gas mass flowmeters measuring the gas outflow. The value used to compute permeability was the one measured by the flowmeter working in the appropriate range. Nitrogen gas was also used in these tests.

Similar to the LP equipment, the relative error of the effective permeability measured in the HP equipment ($k_{ig} \cdot k_{rg}$) represented in Equation (5-3) has three main components (Table 5-3). The relative error of effective gas permeability values ($k_{ig} \cdot k_{rg}$) in the HP equipment was lower than ±1.0 %, resulting from the combination of the relative uncertainties of the measured variables.

Table 5-3. Uncertainty of variables measured in the HP setup.

Variables	Instrument		Uncertainty (%)
Flow: Q_m	Flowmeter	Range (mL /min) = 2	± 0.6 %
		Range (mL /min) = 10	± 0.4 %
		Range (mL /min) = 100	± 0.4 %
Pressures: P_{up} and P_{dw}	Pressure sensor		± 0.04 %
Dimensions: *L* and *A*	Caliper		± 0.016 %

To analyze the effect of injection and confining pressures on permeability, different phases were followed depending on the specimen characteristics. In the high confining pressure (HCP) line (ETAPP and OPC), samples were tested starting with P_c = 0.6 or 1.0 MPa. P_i was slowly increased until a measurable flow was reached (Phase 1) and then P_c was increased up to a pressure as high as to stop gas flow (Phase 2). In other cases, P_c was increased to allow an increase in P_i up to a value high enough to trigger flow. In the low confining pressure (LCP) line (TAS05_09 and BMA), it consisted in four phases (Figure 5-6). Samples were tested at P_i = 0.2 MPa *absolute* and P_c = 3.0 MPa.

P_i was increased from 0.2 to 0.8 MPa *absolute* (Phase 1) followed by an increase in P_c up to 3.5 MPa (Phase 2). At P_c = 3.5 MPa, P_i was decreased down to 0.2 MPa, i.e. the initial value (Phase 3). Finally, samples were unloaded to P_c = 2 MPa (Phase 4).

At the end of the tests, the samples were dismantled, weighed, and oven-dried at 110 °C for 48 hours to determine their dry density and water content.

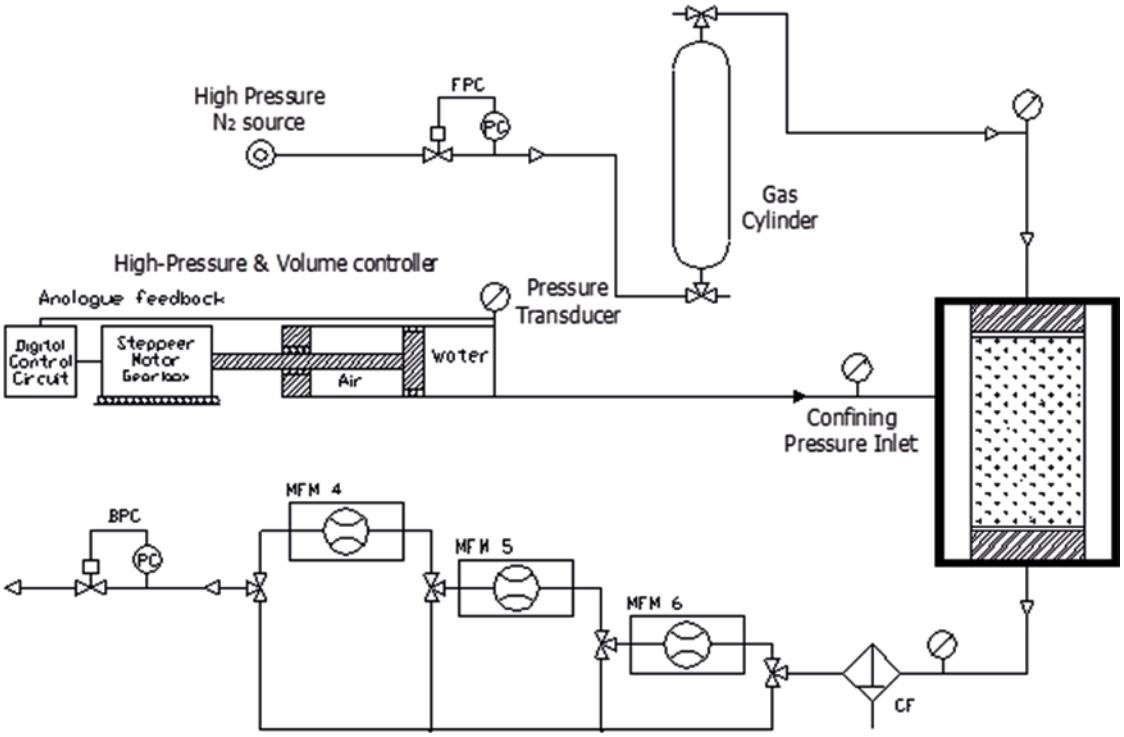

Figure 5-5. *Schematic representation of the high-pressure (HP) gas permeability system. Black lines indicate high confining pressure (HCP) line and orange lines indicate low confining pressure (LCP) line (CF: coalescing filter, FPC: forward-pressure controller, BPC: back-pressure controller, MFM: mass flow meter).*

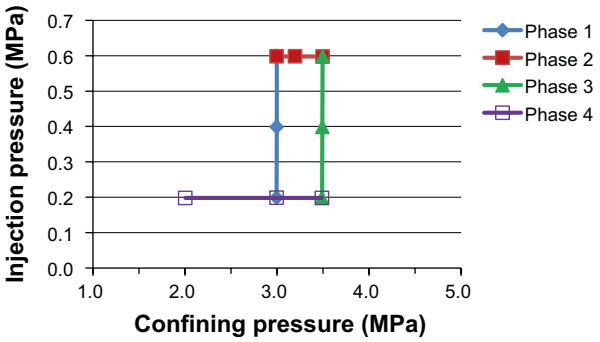

Figure 5-6. *Pressure path followed in the HP equipment at low confining pressure line (LCP) (injection gas pressure in absolute values).*

5.2 Results of gas permeability tests

5.2.1 ETAPP and TAS05_09 concrete samples

Four gas permeability tests were performed in triaxial cells with concrete samples obtained after re-drilling the sub-cores ETAPP and TAS05_09. Before testing, TAS05_09 samples were weighed and oven-dried at 60 ºC until getting constant weight. Table 5-4 summarizes the characteristics of the specimens tested. The initial bulk densities (ρ) of the samples were calculated from their weight and dimensions. The water contents (w) were computed from the dry weights obtained after drying the specimens at the end of the tests.

Table 5-4. Characteristics of the ETAPP and TAS05_09 concrete samples tested for gas permeability (note that additional analysis after drying was conducted on ETAPP samples).

Reference	Duration of drying at 60 °C	Height (cm)	Diameter (cm)	ρ (kg/m^3)	*w* (%)
ETAPP1-6-I-2	-	5.03	5.04	2380	5.8
ETAPP2-2-I-2	-	5.08	5.06	2450	4.7
ETAPP2-2-I-4	-	4.90	5.05	2400	4.8
TAS05_09-A3	Initial	5.15	5.07	2370	4.5
	16 days	5.14	5.06	2300	0.5
TAS05_09-C3	Initial	5.11	5.06	2400	4.1
	16 days	5.10	5.05	2340	0.6

5.2.1.1 ETAPP1-6-I-2

The appearance of the sub-sample ETAPP1-6-I-2 is shown in Figure 5-7. The sample was first tested in the LP equipment with a confining pressure of 0.6 MPa, but after 162 h of testing no flow was measured. Changes in P_i were affected by the laboratory temperature oscillations (differences between day and night).

The sample was then tested in the HP steady-state setup, following the pressure path showed in Figure 5-8 consisting of two phases:

- Phase 1: the concrete sample was tested at P_c = 0.6 MPa and P_i = 0.2 MPa *absolute*. Then, P_c was increased up to 1.0 MPa, and P_i was increased 0.1 MPa every 24 h up to 0.6 MPa, to ensure a measurable flow during the following phase.
- Phase 2: P_c was gradually increased from 1.0 to 2.0 MPa. At that point, the flow measured was below the turndown value (i.e. too low to be reliable).

It is referred here to turndown value to the flow value below which the accuracy of the measurement is not guaranteed. This is a value given by the manufacturer and depends on the gas flowmeter type. Flow values below the turndown value can be measured, but measurements may not correspond to laminar flow, which is necessary to properly compute permeability.

Figure 5-7. *Front (a) and lateral (b) views of ETAPP1-6-I-2 sample for gas permeability tests.*

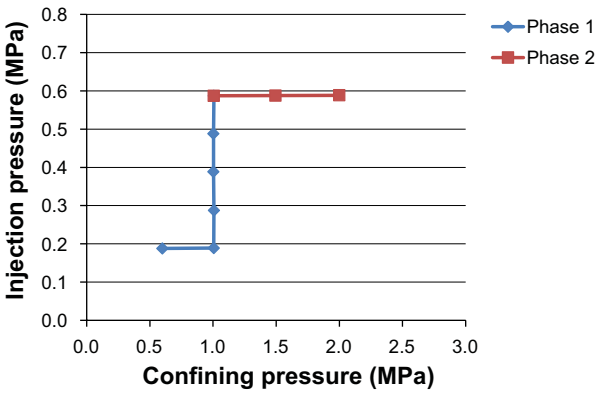

Figure 5-8. *Pressure path followed in the HP permeameter for ETAPP1-6-I-2 sample (injection gas pressure given in absolute values).*

The gas permeability obtained in the HP equipment is shown in Figure 5-9. Consistently with the lack of flow in the LP setup, the flow values recorded were below the turndown value until the application of P_i = 0.4 MPa *absolute*. During Phase 1, changes in P_i did not cause changes in gas permeability (Figure 5-9 a). However, the increase of P_c caused a decrease of gas permeability. The sample was subjected to a maximum P_c = 2.0 MPa, for which the flow measured was below the turndown value, so that gas permeability could not be calculated (Figure 5-9 b).

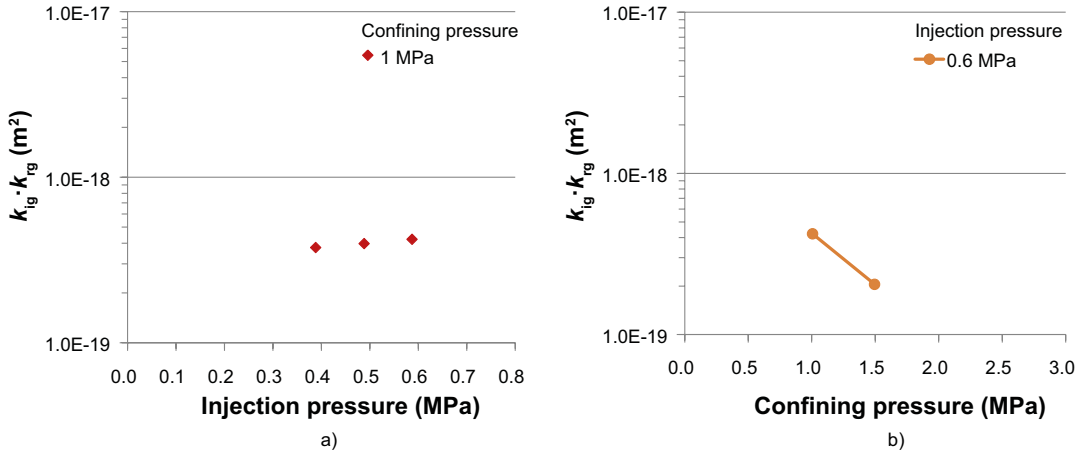

Figure 5-9. *Evolution of gas effective permeability at constant confining pressure (a) and constant injection pressure (b) for sample ETAPP1-6-I-2 (injection gas pressure given in absolute values).*

5.2.1.2 ETAPP2-2-I-2

The appearance of the sub-sample ETAPP2-2-I-2 is shown in Figure 5-10. The specimen was initially tested in the LP equipment using confining pressures of 0.6 and 1.0 MPa. The decrease in P_i in the upstream tank at the beginning of the test at P_c = 0.6 MPa was affected by the laboratory temperature. After 80 h of testing, an outflow of gas could be measured at the outlet and gas permeability was computed. Then, P_c was increased to 1.0 MPa. At this stage, P_i changes were directly related to temperature changes in the laboratory, which indicates that no flow was taking place.

Subsequently the sample was tested in the HP equipment in two phases (Figure 5-11):

- Phase 1: while P_c was kept constant (1.0 MPa), P_i was gradually increased from 0.2 to 0.6 MPa *absolute*.
- Phase 2: P_c was gradually increased from 1.0 to 2.5 MPa, with P_i = 0.6 MPa *absolute*.

The results of the gas permeability measurements are plotted in Figure 5-12. The test started at P_c = 1.0 MPa and P_i = 0.2 MPa *absolute*, similar to the LP setup. During this step, the outflow measured was below the turndown value and thus not reliable. Then, P_i was increased to trigger a flow sufficiently high to be measured accurately. During the increase of P_i from 0.2 to 0.6 MPa *absolute* in Phase 1, the gas permeability did not change (Figure 5-12 a). However, the increase of P_c caused a clear decrease in gas permeability (Figure 5-12 b). During the last step of the test, with P_c = 2.5 MPa, the flow decreased below the turndown value of the flowmeters and permeability was not computed.

Figure 5-10. *Front (a) and lateral (b) views of ETAPP2-2-I-2 sample for gas permeability tests.*

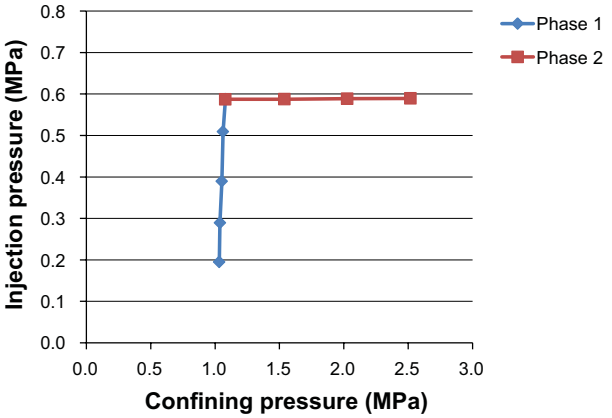

Figure 5-11. *Pressure path followed in the HP permeameter for sample ETAPP2-2-I-2 (injection gas pressure given in absolute values).*

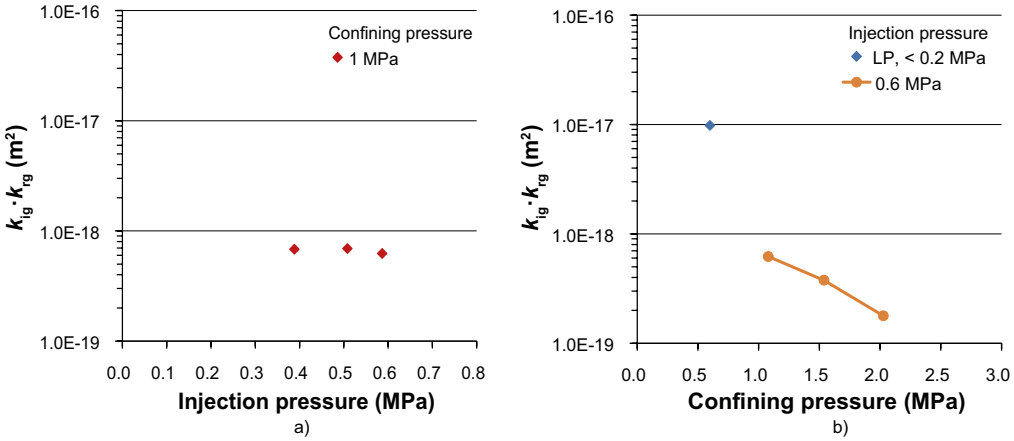

Figure 5-12. *Evolution of gas effective permeability at constant confining pressure (a) and constant injection pressure (b) for sample ETAPP2-2-I-2 (injection gas pressure given in absolute values).*

5.2.1.3 ETAPP2-2-I-4

The appearance of the sub-sample ETAPP2-2-I-4 is shown in Figure 5-13. The sample was initially tested in the LP equipment with a confining pressure of 0.6 MPa, but after 95 h of testing no outflow was detected. P_i variability caused by changes in laboratory temperature was once again observed. Consequently, no permeability values could be computed.

Afterwards, sample was tested in the HP equipment, starting with the last pressures used in the previous setup. The pressure path followed is shown in Figure 5-14:

- Phase 1: the test began with the same pressures used in the LP permeameter (P_i = 0.2 MPa *absolute* and P_c = 0.6 MPa). At that point, noticeable flow was measured, and gas permeability could be computed. Then P_c was increased to 1.0 MPa. At constant P_c, P_i was then increased up to 0.6 MPa *absolute* (0.1 MPa every 24 h) to increase the flow up to a measurable value.
- Phase 2: P_c was increased from 1.0 to 2.5 MPa (0.5 each step) with P_i = 0.6 MPa *absolute*. During the last step, the flow decreased to a value below the turndown, so the calculation of gas permeability could not be reliably done.
- Phase 3: at P_c = 2.5 MPa, P_i was increased until obtaining a flow above the turndown value.

The gas permeability value obtained in the HP equipment is shown in Figure 5-15. The test started with the pressures applied in the LP equipment (P_c = 0.6 MPa and P_i = 0.2 MPa *absolute*), in which no flow was observed. Surprisingly, flow was high enough to compute gas permeability. During Phase 1, the increase of P_i at P_c = 1 MPa did not cause any change in the gas permeability value (Figure 5-15 a). After that, the increase of P_c from 1.0 to 2.5 MPa (Phase 2) at constant P_i provoked a clear decrease of the effective gas permeability (Figure 5-15 b). In fact, at P_c = 2.5 MPa the measured flow was below the turndown value. Thus, P_i was increased up to 1 MPa *absolute* (Phase 3) to get a correctly measurable flow. The increase of P_i during this phase did not cause any change in gas permeability, similarly to Phase 1 (Figure 5-15 a).

Figure 5-13. *Front (a) and lateral (b) views of ETAPP2-2-I-4 sample for gas permeability tests.*

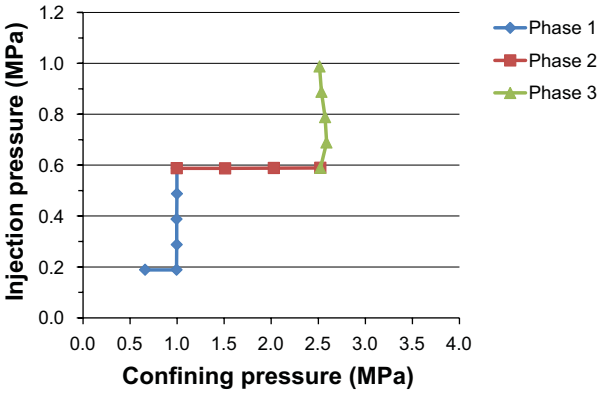

Figure 5-14. *Pressure path followed in the HP permeameter for sample ETAPP2-2-I-4.*

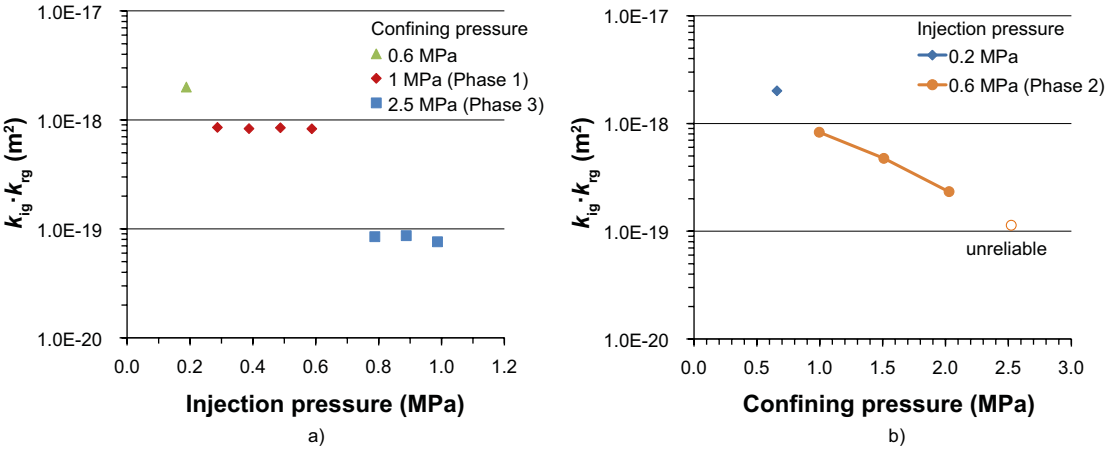

Figure 5-15. *Evolution of gas effective permeability at constant confining pressure (a) and constant injection pressure (b) for sample ETAPP2-2-I-4 (injection gas pressure given in absolute values).*

5.2.1.4 TAS05_09-A3

The appearance of the sub-sample TAS05_09-A3 is shown in Figure 5-16. Since there were a few cavities on the concrete surface, a filler was inserted in the cavities along the surface of the sample to prevent the risk of membrane piercing during the test.

The sample was first tested in the LP equipment with a confining pressure of 0.6 MPa. Figure 5-17 shows a continuous pressure drop in the upstream tank (a) and the gas permeability computed at 0.6 MPa of confining pressure (b).

Subsequently, the sample was tested in the HP equipment, following the pressure path showed in Figure 5-6 consisting of 4 phases. Results of the gas permeability measurements are plotted in Figure 5-18. Steady outflows were measured by the proper range gas flowmeter in a few minutes for all steps. The test started at P_c = 3 MPa and P_i = 0.2 MPa *absolute*. After 15 minutes of testing, the flowmeters recorded steady outflow. Nevertheless, this pressure step was kept for 4 hours to verify the steady flow. P_i was then increased from 0.2 to 0.6 MPa *absolute* in Phase 1, with a slight decrease in gas permeability (Figure 5-18 a). The increase of P_c during Phase 2 did not cause any change in gas permeability (Figure 5-18 b). During Phase 3, the outflow decreased until reaching the same value firstly measured at P_i = 0.2 MPa and P_c = 3 MPa *absolute*. During unloading (Phase 4), gas permeability did not change, similar to Phase 2. At the end of the test the sample was dismantled (Figure 5-19 a–b), weighed and oven-dried at 110 ºC for 48 hours.

Figure 5-16. *Front (a) and lateral (b) views of TAS05_09-A3 sample for gas permeability tests.*

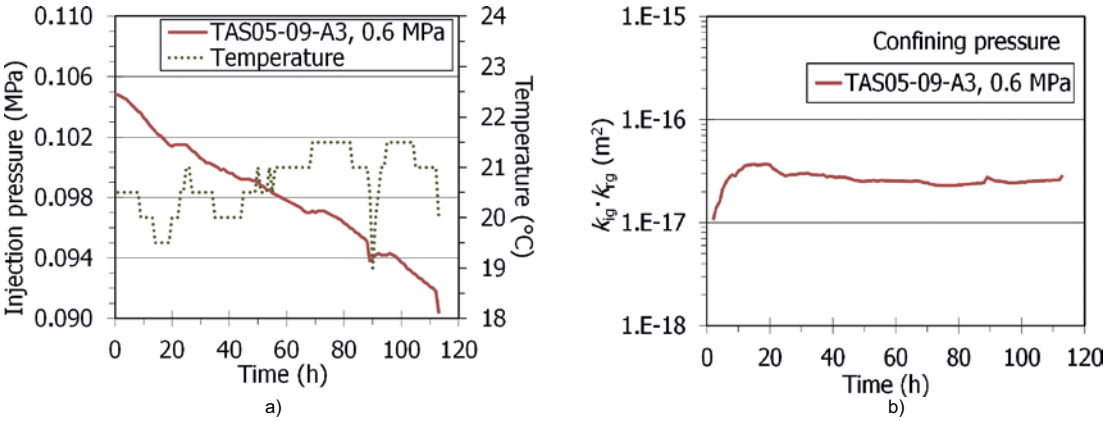

Figure 5-17. *Evolution of injection pressure (a) and gas effective permeability (k_{ig}·k_{rg}) (b) in the LP equipment at 0.6 MPa of confining pressure for sample TAS05_09-A3.*

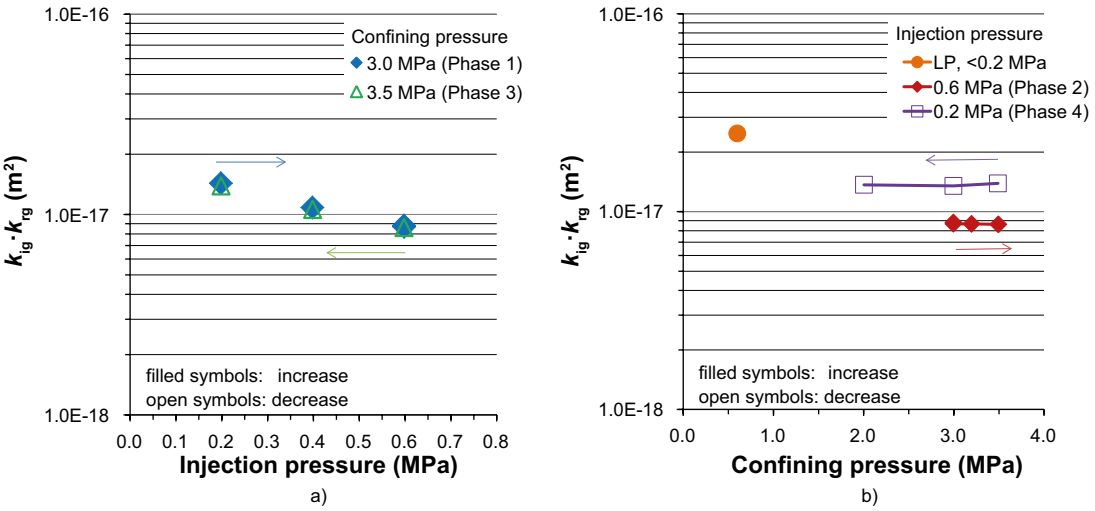

Figure 5-18. *Evolution of gas effective permeability at constant confining pressure (a) and constant injection pressure (b) for sample TAS05_09-A3 (injection pressure given in absolute values).*

a) b)

Figure 5-19. *Dismantling of sample TAS-05-09-A3 after gas permeability tests.*

5.2.1.5 TAS05_09-C3

The appearance of the sub-sample TAS05_09-C3 is shown in Figure 5-20. This sample was tested in the LP setup at 0.6 MPa of confining pressure. The pressure in the upstream tank decreased steadily from the beginning (Figure 5-21 a) and gas permeability could be computed (Figure 5-21 b).

a) b)

Figure 5-20. *Front (a) and lateral (b) views of TAS05_09-C3 sample for gas permeability tests.*

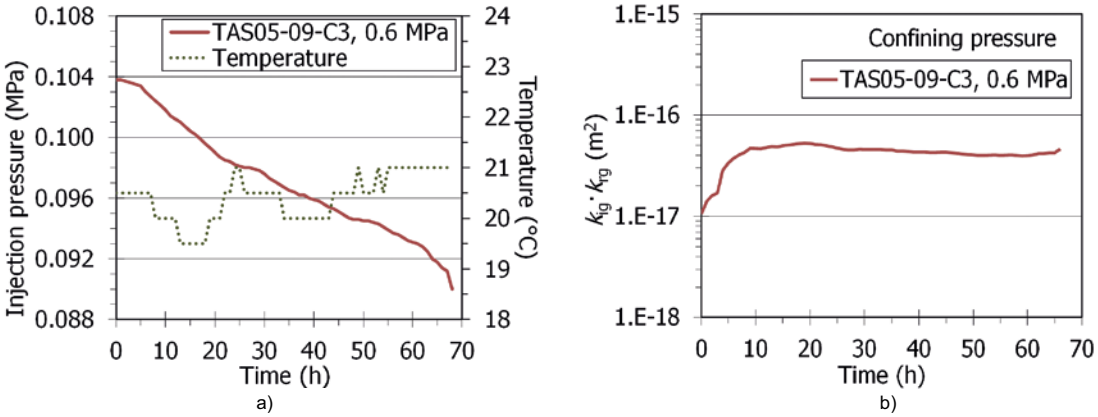

a) b)

Figure 5-21. *Evolution of injection pressure and gas effective permeability ($k_{ig} \cdot k_{rg}$) in the low-pressure equipment (LP) at 0.6 MPa of confining pressure for sample TAS05_09-C3.*

Afterwards, the sample was tested in the HP equipment with the following pressure path (Figure 5-6):

- Phase 1: the test began at P_c = 3 MPa. During this phase, P_i was increased from 0.2 to 0.8 MPa *absolute* applying four steps of one-hour duration.
- Phase 2: P_c was increased up to 3.5 MPa at P_i = 0.8 MPa *absolute*.
- Phase 3: P_i was decreased from 0.8 to 0.2 MPa *absolute*. At that point, the membrane was pierced, and the cell had to be dismantled.
- Phase 4: this phase could not be tested because of the membrane piercing.

The gas permeability obtained in the HP equipment is shown in Figure 5-22. The test started at P_c = 3 MPa and P_i = 0.2 MPa *absolute*. During Phase 1, P_i was increased 0.2 MPa each hour until reaching 0.8 MPa *absolute*. The increase of P_i caused a slight decrease in gas permeability. Then, P_c was increased up to 3.5 MPa (Phase 2), with no change in permeability (Figure 5-22 b). In Phase 3, P_i decreased, and the gas permeability values computed were almost the same as the values obtained during Phase 1 (Figure 5-22 a). At that point, the membranes were pierced, and the cell had to be dismantled (Figure 5-23 a). During dismantling, it was observed that the failure was originated at the contact between sample and porous stones. The high confining pressure applied caused the membrane piercing in an area of weakness. As a result, the sample was wetted at the upper end (Figure 5-23 b).

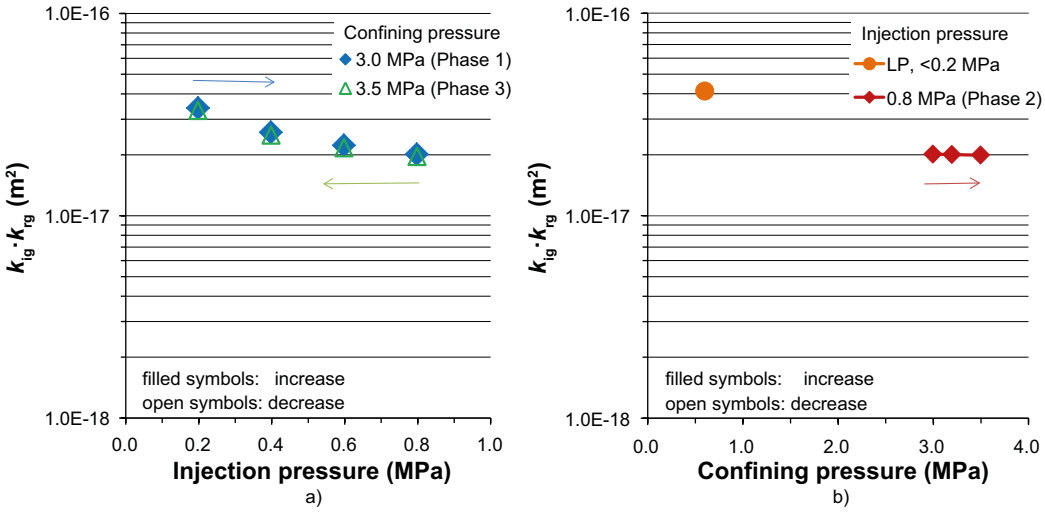

Figure 5-22. *Evolution of gas effective permeability at constant confining pressure (left) and constant injection pressure (right) for sample TAS05_09-C3 (injection pressure given in absolute values).*

Figure 5-23. *Piercing of membranes (a) and sample wetted at the upper end after failure (b).*

5.2.2 OPC and BMA micro-concretes

Four gas permeability tests were performed in triaxial cells with concrete samples obtained from OPC and BMA micro-concrete specimens. BMA samples were weighed and dried in the oven at 60 ºC until getting steady weight. Table 5-5 summarises the characteristics of the specimens before testing. The initial bulk densities (ρ) of the samples were calculated from their weight and dimensions. The water contents (w) were computed from the dry weights obtained after drying the specimens at the end of the tests.

Table 5-5. Characteristics of the OPC and BMA concrete samples tested for gas permeability (note that additional analysis after drying was conducted on BMA samples).

Sample	Duration of drying at 60 °C	Height (cm)	Diameter (cm)	ρ (kg/m^3)	w (%)
OPC-P5	-	5.00	3.73	2270	5.1
BMA-B5	Initial	5.04	5.06	2300	5.3
	23 days	5.04	5.06	2200	0.7
BMA-B7	Initial	4.96	5.06	2340	4.1
	34 days	4.94	5.06	2270	0.4

5.2.2.6 OPC-P5

The appearance of the sub-sample OPC-P5 is shown in Figure 5-24. The OPC-P5 sample was tested in the LP equipment under confining pressures of 0.6 and 1.0 MPa (Figure 5-25 a). The relative pressure decreased in the tank at 0.6 MPa of confining pressure and gas permeability was computed (Figure 5-25 b) (see the end of this section for a re-evaluation of this value). Then, the sample was tested at 1.0 MPa of confining pressure for almost 10 days. No flow went through the sample during this period, since changes in the tank pressure were just related to changes in laboratory temperature.

Figure 5-24. *Front (a) and lateral (b) views of OPC-P5 sample for gas permeability tests.*

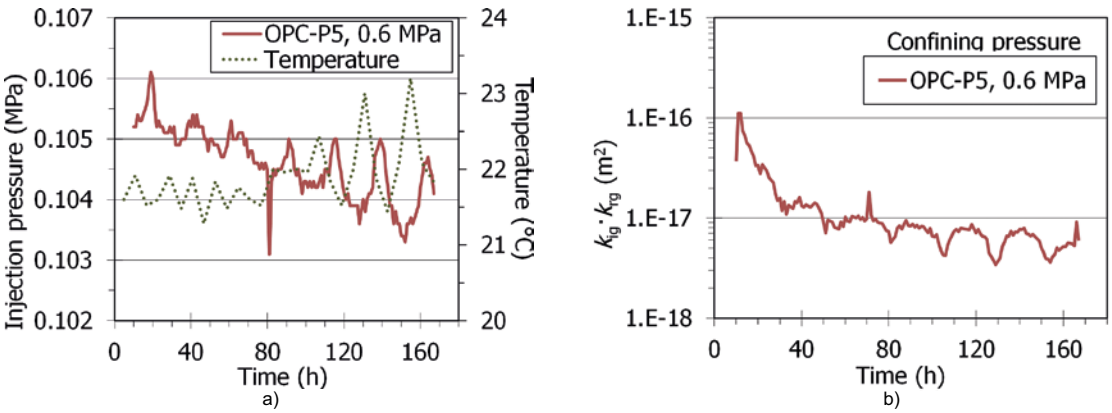

Figure 5-25. *Evolution of injection pressure (relative values) and gas effective permeability (k_{ig}·k_{rg}) in the LP equipment at 0.6 MPa of confining pressure for sample OPC-P5.*

Afterwards, the sample was tested in the HP equipment. At the beginning, the pressures were set to P_c = 1.0 MPa and P_i = 0.2 MPa *absolute*. P_i was increased up to 0.5 MPa *absolute*. No flow was detected during this period. During testing, it was observed that the latex membranes entered the cavities of concrete due to the confining pressure. The sample was thus dismantled to avoid membrane piercing and the cavities along the sample surface were filled with a filler (Figure 5-26 a). The weight of the filler was determined by weighing the sample before and after its application. The modified sample, now with a smoother surface (Figure 5-26 b), was mounted again in the cell and gas testing resumed.

The pressure path followed before and after modifying the sample is shown in Figure 5-27:

- Phase 1: the test began with the last pressure applied in the LP equipment. P_i was increased by steps up to 0.8 MPa *absolute*.
- Phase 2: P_c was increased from 1.0 to 1.5 MPa to be able to increase the injection pressure in an attempt to obtain a measurable flow.

After remounting the sample, pressures were restored at P_c = 1.0 MPa and P_i = 0.5 MPa *absolute* when a slight flow was observed, although with a value below the turndown value. P_i was then increased up to 0.8 MPa *absolute* (0.1 MPa every 24 h) to get an accurately measurable flow. At that point, the difference between P_c and P_i was 0.2 MPa, which is considered to be the minimum value necessary to ensure the adherence of the membranes to the sample surface. During most of Phase 1, measured flow was below the turndown value; only at P_i = 0.8 MPa *absolute* flow was close to it. Before further increasing of P_i, P_c had to be increased to 1.5 MPa. Then, P_i was increased again (Phase 2) with the same result: the flow measured was below the turndown value.

a) b)

Figure 5-26. *Application of the filler in the surface cavities of the concrete sample (a) and final appearance after filling the cavities (b).*

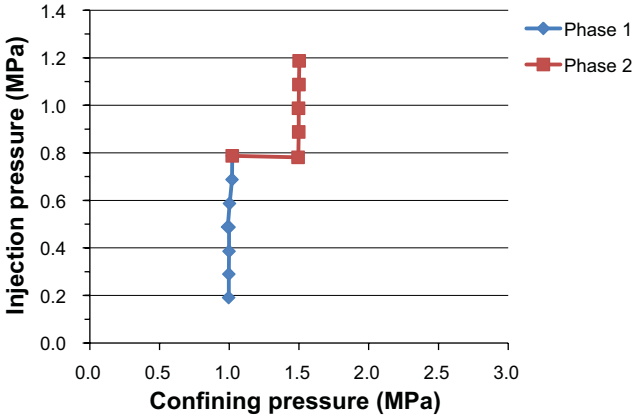

Figure 5-27. *Pressure path followed in the HP permeameter for sample OPC-P5 (injection gas pressure given in absolute values).*

Although the flow measured during the whole test was below the turndown value, tentative gas permeability values were computed for each step (Figure 5-28), even though the accuracy of these values cannot be guaranteed. In contrast to the ETAPP samples, the increase of P_i caused an increase in the gas permeability at P_c = 1.0 and 1.5 MPa (Phase 1 and Phase 2, respectively). On the other hand, the increase of P_c caused a clear decrease in gas permeability.

After 25 days, the test in the HP equipment was terminated and the cell was tested again in the LP permeameter to check the permeability computed before modifying the sample. The modified sample was tested at 0.6 MPa of confining pressure in the LP equipment for 6 days. During this time, measured changes in the pressure tank (P_i) were related to temperature changes in the laboratory and thus no flow went through the sample. Hence, it is considered that the measured flow during the first testing in the LP equipment (Figure 5-25) could have taken place along sample surface, i.e. between the membrane and the sample. Therefore, the obtained gas permeability value at these circumstances was considered not reliable and discarded. Note that, during dismantling, the sample was accidentally wetted (Figure 5-29 a–b).

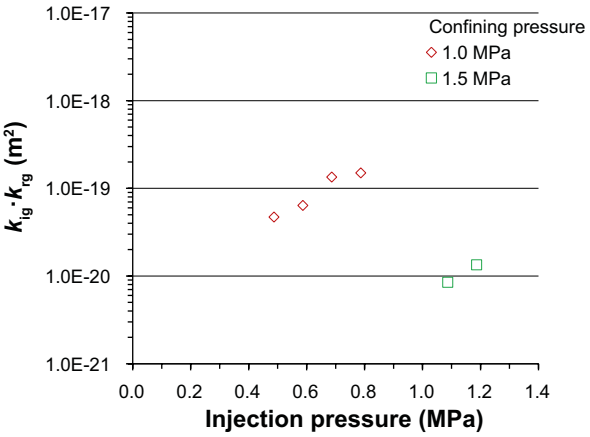

Figure 5-28. *Gas effective permeability (tentative values) at constant P_c for sample OPC-P5.*

Figure 5-29. *Final appearance of sample OPC-P5 (a–b) after gas permeability tests.*

5.2.2.7 BMA-B5

Sample BMA-B5 was obtained from the sub-core of cylinder B from the original block (Figure 2-11) and presented numerous cavities on its surface (Figure 5-30 a–b), which were filled with a filler (Figure 5-31 a). One of the cavities was at the edge of the cylinder so a small amount of filler was also placed in the tested surface (Figure 5-31 b). The sample was weighed before and after filling the cavities to determine the weight of the filler. To reinforce the weakness area (contact between sample and porous stones) extra latex rings were placed after the parafilm and duct tape and before wrapping the sample in two latex membranes (Figure 5-31 c–d).

The sample was first tested in the LP equipment for three days at P_c = 0.6 MPa. The decrease of P_i in the upstream tank and the computed gas permeability are shown in Figure 5-32 a–b.

Figure 5-30. *Elevation (a) and lateral (b) views of BMA-B5 sample for gas permeability tests.*

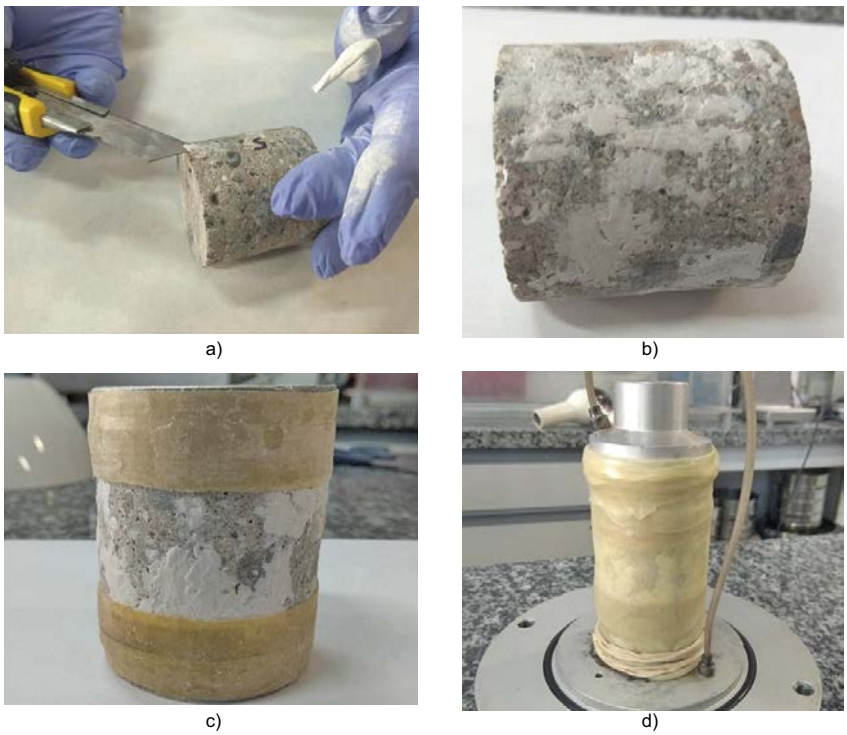

Figure 5-31. *Application of the filler (a) and appearance of sample BMA-B5 after filling the cavities (b); Latex rings placed around the concrete/porous stone contact before wrapping (c) and sample wrapped in double latex membranes (d).*

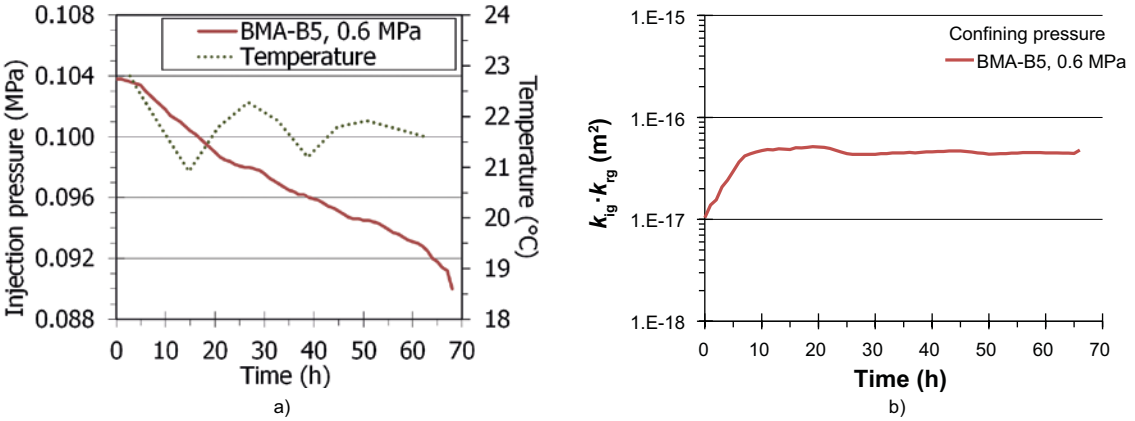

Figure 5-32. *Evolution of injection pressure and gas effective permeability ($k_{ig} \cdot k_{rg}$) in the LP equipment at 0.6 MPa of confining pressure for sample BMA-B5.*

Afterwards, the sample was moved to the HP setup and tested with the pressure path of Figure 5-6. Gas permeability obtained in the HP equipment is shown in Figure 5-33. The increase of P_i during Phase 1 caused a decrease of gas permeability. Similarly, gas permeability increased with the decrease of P_i in Phase 3 (see Figure 5-33 a). In contrast, P_c variations during Phases 2 and 4 did not cause changes in the calculated gas permeability (Figure 5-33 b).

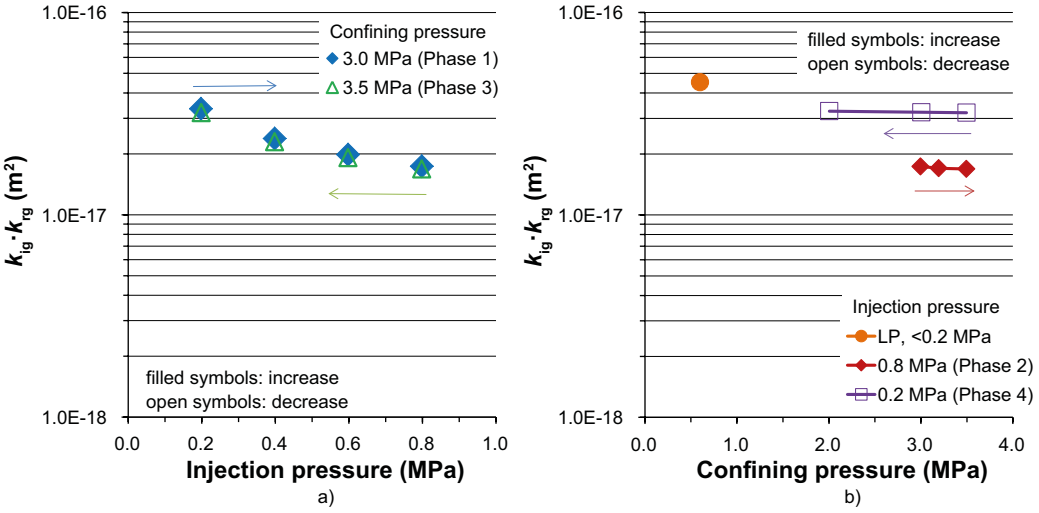

Figure 5-33. *Evolution of gas effective permeability at constant confining pressure (a) and constant injection pressure (b) for sample BMA-B5 (injection pressure given in absolute values).*

5.2.2.8 BMA-B7

Sample BMA-B7 was obtained from the sub-core of cylinder B from block BMA, with the position number 7 (Figure 2-11). The appearance of this sub-sample is shown in Figure 5-34 a–b. Again, large cavities on the surface were filled with a filler (Figure 5-34 c). The sample was tested in the LP equipment for 2 days at a confining pressure of 0.6 MPa. The pressure decreased in the upstream tank and the computed gas permeability are shown in Figure 5-35 a–b. The HP equipment was used subsequently, and the gas permeability obtained is shown in Figure 5-36 a–b.

Figure 5-34. *Lateral views of BMA-B7 sample (a–b) for gas permeability tests and preparation of the sample before wrapping (c).*

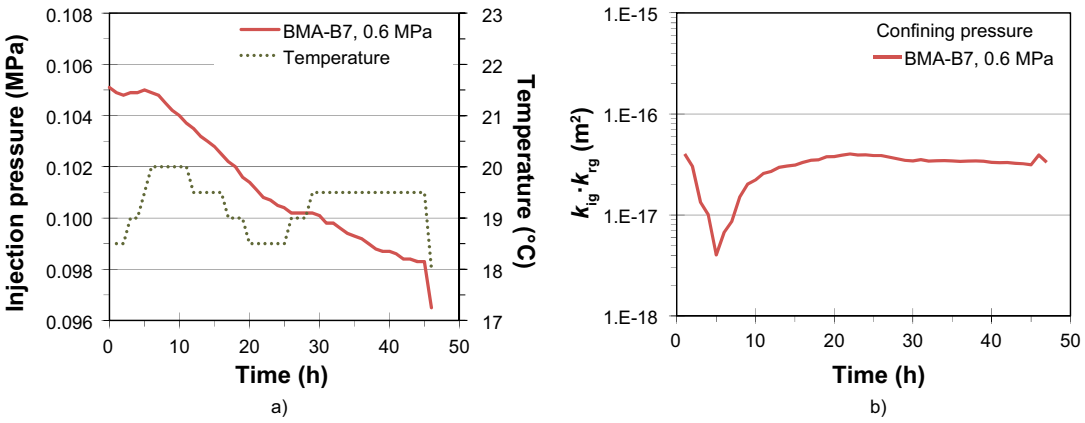

Figure 5-35. *Evolution of injection pressure and gas effective permeability ($k_{ig} \cdot k_{rg}$) in the LP equipment at 0.6 MPa of confining pressure for sample BMA-B7.*

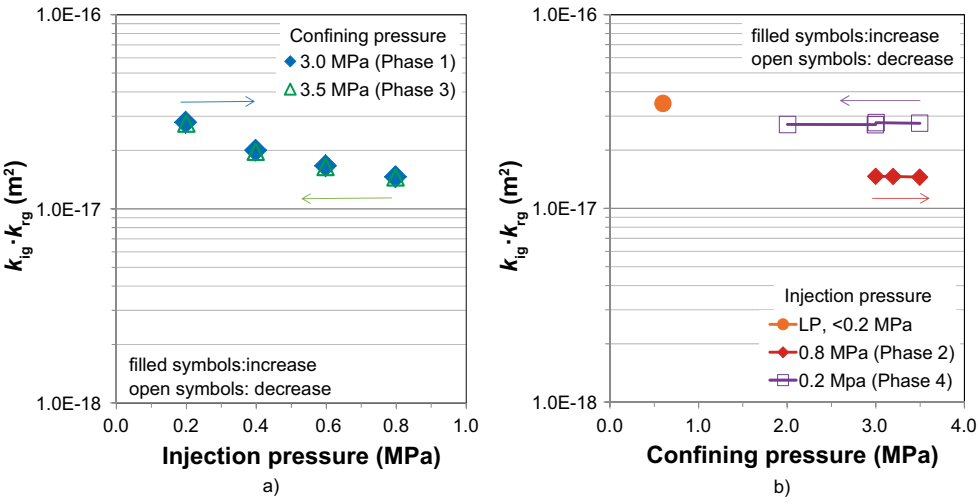

Figure 5-36. *Evolution of gas effective permeability at constant confining pressure (a) and constant injection pressure (b) for sample BMA-B7 (injection pressure given in absolute values).*

5.2.3 Summary of gas permeability results

Gas permeability was measured in four samples belonging to the different studied types of concrete: ETAPP1, ETAPP2, TAS05_09, OPC and BMA. TAS05_09 and BMA were initially dried in the oven at 60 ºC until constant weight to obtain a common baseline. After drying, the average water content of the samples was 0.6 ± 0.1 %. The drying process resulted in shrinking of the samples. All the samples were initially tested in the low-pressure setup (LP) and then in the high-pressure setup (HP). Different paths were followed depending on the specimen characteristics. A summary of the initial and final characteristics of the samples and the gas permeability values measured with both setups is shown in Table 5-6.

Figure 5-37 shows the effective gas permeability measured in the HP setup at increasing P_i. In the range of pressure tested, no effect of P_i on gas permeability was seen for the ETAPP samples. The effective gas permeability decreased with the increase of injection pressure for TAS05_09 and BMA samples, whereas it increased with the increase in P_i for the OPC sample. For this reason, the values obtained at a given injection pressure for TAS05_09 and BMA specimens are the average of all values measured under different confining pressures, mostly in the range 3.0–3.5 MPa. In all the tested samples, the effective permeability value obtained in the LP setup (confining pressure of 0.6 MPa and injection pressure lower than 0.1 MPa) was higher than that obtained with the HP setup.

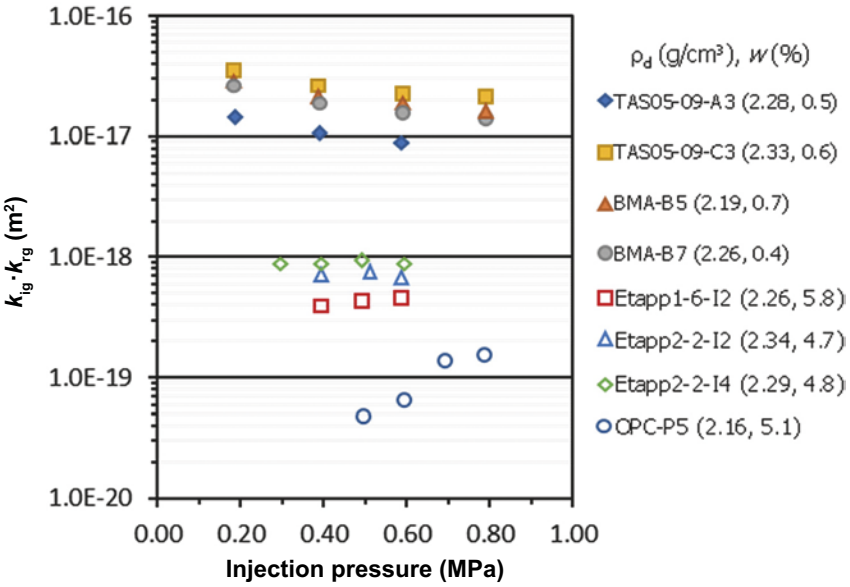

Figure 5-37. *Comparative evolution of effective gas permeability with injection pressure at constant confining pressure of 1 MPa (ETAPP and OPC) and 3–3.5 MPa (TAS05_09 and BMA) in the HP setup (injection gas pressure given in absolute values).*

Table 5-6. Summary of gas permeability results.

Parameter		ETAPP 1-6-I2	ETAPP 2-2-I2	ETAPP 2-2-I4	TAS[a] 05_09A3	TAS 05_09C3	OPC-P5[a, c]	BMA-B5	BMA-B7
Initial *w* (%)		5.8	4.7	4.8	0.5	0.6	5.1	0.7	0.4
Final *w* (%)		5.9	4.7	5.5[a]	1.3	1.4[a]	6.7[a]	0.8	0.5
Confining *P* (MPa)		LP setup							
0.6	$k_{ig}\cdot k_{rg}$ (m^2)	No flow	9.8×10^{-18}	No flow	2.5×10^{-17}	4.1×10^{-17}	No flow	4.5×10^{-17}	3.4×10^{-17}
	k_g (m/s)	No flow	6.1×10^{-12}	No flow	1.5×10^{-11}	2.5×10^{-11}	No flow	2.8×10^{-11}	2.1×10^{-11}
1.0	$k_{ig}\cdot k_{rg}$ (m^2)	-	No flow	-	-	-	No flow	-	-
	k_g (m/s)	-	No flow	-	-	-	No flow	-	-
Duration test LP (days)		7	18	4	5	3	17 + 6[b]	3	2
Injection P (Confining P) (MPa)		HP setup							
(0.6)	$k_{ig}\cdot k_{rg}$ (m^2)	No flow	-	2.0×10^{-18}	-	-	-	-	-
	k_g (m/s)	No flow	-	1.1×10^{-12}	-	-	-	-	-
(1.0)	$k_{ig}\cdot k_{rg}$ (m^2)	4.0×10^{-19}	6.6×10^{-19}	8.4×10^{-19}	-	-	9.9×10^{-20}	-	-
	k_g (m/s)	2.3×10^{-13}	3.2×10^{-13}	4.8×10^{-13}	-	-	5.8×10^{-14}	-	-
(1.5)	$k_{ig}\cdot k_{rg}$ (m^2)	2.1×10^{-19}	3.8×10^{-19}	4.8×10^{-19}	-	-	1.1×10^{-20}	-	-
	k_g (m/s)	1.2×10^{-13}	2.2×10^{-13}	2.8×10^{-13}	-	-	6.4×10^{-15}	-	-
(2.0)	$k_{ig}\cdot k_{rg}$ (m^2)	No flow	1.8×10^{-19}	2.3×10^{-19}	-	-	-	-	-
	k_g (m/s)	No flow	1.0×10^{-13}	1.3×10^{-13}	-	-	-	-	-
(2.0)	$k_{ig}\cdot k_{rg}$ (m^2)	-	No flow	8.2×10^{-20}	-	-	-	-	-
	k_g (m/s)	-	No flow	4.8×10^{-14}	-	-	-	-	-
0.2 (2.0–3.5)	$k_{ig}\cdot k_{rg}$ (m^2)	-	-	-	1.4×10^{-17}	3.4×10^{-17}	-	3.3×10^{-17}	2.8×10^{-17}
	k_g (m/s)	-	-	-	8.2×10^{-12}	2.0×10^{-11}	-	1.9×10^{-11}	1.6×10^{-11}
0.4 (3.0–3.5)	$k_{ig}\cdot k_{rg}$ (m^2)	-	-	-	1.1×10^{-17}	2.5×10^{-17}	-	2.3×10^{-17}	2.0×10^{-17}
	k_g (m/s)	-	-	-	6.3×10^{-12}	1.5×10^{-11}	-	1.4×10^{-11}	1.2×10^{-11}
0.6 (3.0–3.5)	$k_{ig}\cdot k_{rg}$ (m^2)	-	-	-	8.7×10^{-18}	2.2×10^{-17}	-	1.9×10^{-17}	1.7×10^{-17}
	k_g (m/s)	-	-	-	5.1×10^{-12}	1.3×10^{-11}	-	1.2×10^{-11}	9.8×10^{-12}
0.8 (3.0–3.5)	$k_{ig}\cdot k_{rg}$ (m^2)	-	-	-	-	2.0×10^{-17}	-	1.7×10^{-17}	1.5×10^{-17}
	k_g (m/s)	-	-	-	-	1.2×10^{-11}	-	1.0×10^{-11}	8.7×10^{-12}

a. Sample was accidentally wetted during dismantling; b. Modified sample tested in the LP permeameter at 0.6 MPa of CP for 6 days, after testing the sample in the HP equipment; c. Tentative permeability values.

To further analyse the effective gas permeability results, the difference of the squared pressures (injection, P_{up}, and backpressures, P_{dw}) is plotted against flow in Figure 5-38. A linear relationship was observed in almost all the samples tested, which indicates that stationary single-phase gas flow took place as described by Equation (5-3). However, the relationship was not clearly linear for the OPC sample, which could indicate that the flow was not stationary, and that Darcy's law cannot strictly be applied to compute permeability. Hence, the observed decrease in gas permeability with increasing injection pressure can only be attributed to an insufficient flow increase to counteract such increase of injection pressure in Equation (5-3) (Figure 5-39).

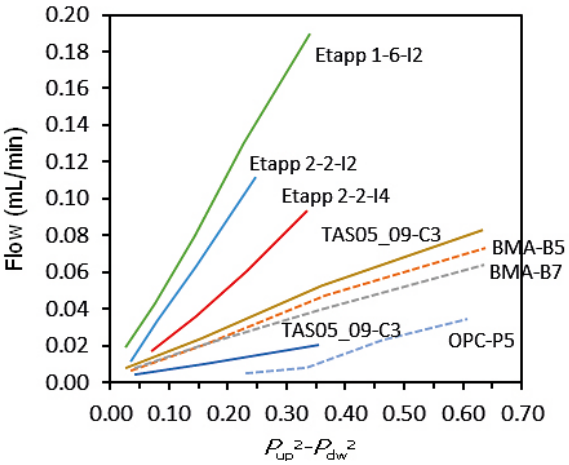

Figure 5-38. *Relationship between flow and difference of squared pressures for all the samples tested.*

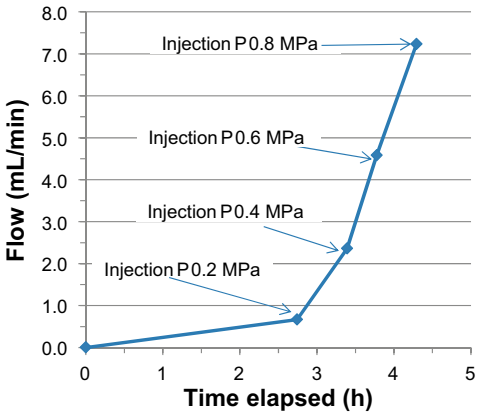

Figure 5-39. *Measured gas flow as a function of the time elapsed corresponding to Phase 1 (confining pressure 3 MPa) for sample BMA-B5 (increase of 0.2 MPa absolute in the injection pressure per step).*

Figure 5-40 shows the effective gas permeability values at different confining pressures. In the range of pressures tested, changes in confining pressure have no effect on TAS05_09 and BMA gas permeability, whereas a decrease of gas permeability with confining pressure was significant and followed the same trend for all the ETAPP samples (see Section 8). For the less saturated sample (i.e. ETAPP2-2-I4), the value of permeability measured was higher and consequently the confining pressure had to be increased to a higher value to stop flow (up to 2 and 2.5 MPa). The tentative gas permeability values for the OPC sample follow a steeper decrease with the increase of confining pressure, decreasing one order of magnitude when the confining pressure was increased from 1.0 to 1.5 MPa.

It is important to note that the different permeability results obtained from the two sub-samples of core TAS05_09 could be explained by the position of the sub-samples in the as-received core, i.e. sub-sample TAS05_09-A3 was taken from the inner part of the core, whereas TAS05_09-C3 was taken closer to the outer part. The results in Table 4-2 show that the density of the core tends to decrease towards the outer part, which is consistent with the higher permeability obtained from TAS05_09-C3 sub-sample.

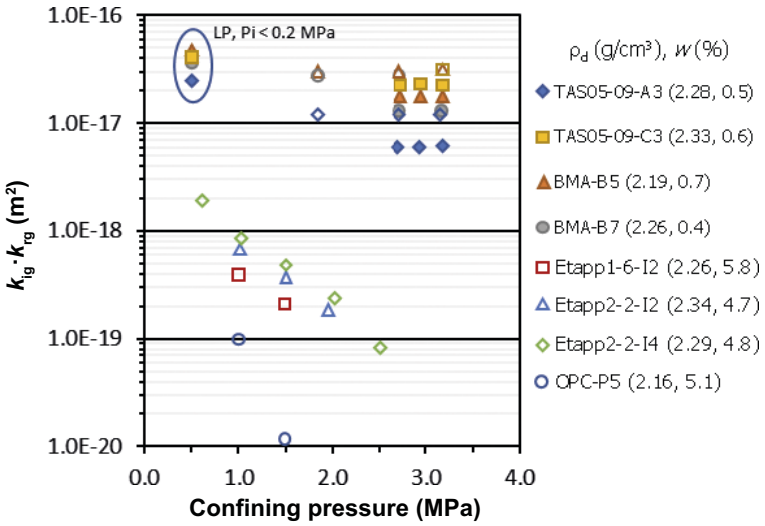

Figure 5-40. *Change of effective gas permeability with increasing confining pressure (the values are the average of all steps under the same confining pressure). For TAS05_09 and BMA samples, solid symbols denote Phase 2 (Pi = 0.8 MPa) and open symbols Phase 4 (Pi = 0.2 MPa).*

6 Hydraulic conductivity

6.1 Experimental method and analytical approach

The hydraulic conductivity was determined by measuring the volume of water passing through a cylindrical sample of saturated material laterally confined and subject to a hydraulic gradient along its axis as a function of time. The method consists in applying a hydraulic load (ΔP, in m), i.e. a potential difference, between the upper and lower part of a sample previously saturated of fixed and known dimensions (surface: A, height: L). At the same time, the flow of water passing through the sample is measured ($\Delta V/\Delta t$). With these parameters, the hydraulic conductivity (k_w, in m/s) is calculated applying Darcy's law (6-1).

$$k_w = \frac{\Delta V \cdot L}{A \cdot \Delta T \cdot \Delta P} \tag{6-1}$$

The intrinsic permeability (k_{iw}, in m^2) is calculated from hydraulic conductivity as

$$k_{iw} = \frac{k_w \cdot \mu_w}{\rho_w \cdot g} \tag{6-2}$$

where μ_w is the dynamic viscosity of water (1×10^{-3} Pa·s), ρ_w is the density of water (10^3 kg/m^3) and g is the gravity constant (9.81 m/s^2).

6.1.1 Permeameter set-up

The water used for the tests was prepared according to the description given in Section 2.3 (composition of the solutions given in Table 2-2). The assemblage of the sample in the triaxial cell followed the same procedure as for gas permeability. The valves of the triaxial cell at the top and bottom of the sample were connected to the constant load permeameter (Figure 6-1) through two water exchange tanks in which the equilibrium solution was placed. For the initial saturation of the sample, a water injection pressure of 0.6 MPa was applied to the top and bottom of the test specimen, with a confining pressure of 0.8 MPa in the triaxial cell. Once the sample was saturated under constant confining pressure, a hydraulic load of around 0.1 MPa was applied, increasing the injection pressure at the bottom to perform the measurement. The hydraulic load was generated by the mercury column of the permeameter.

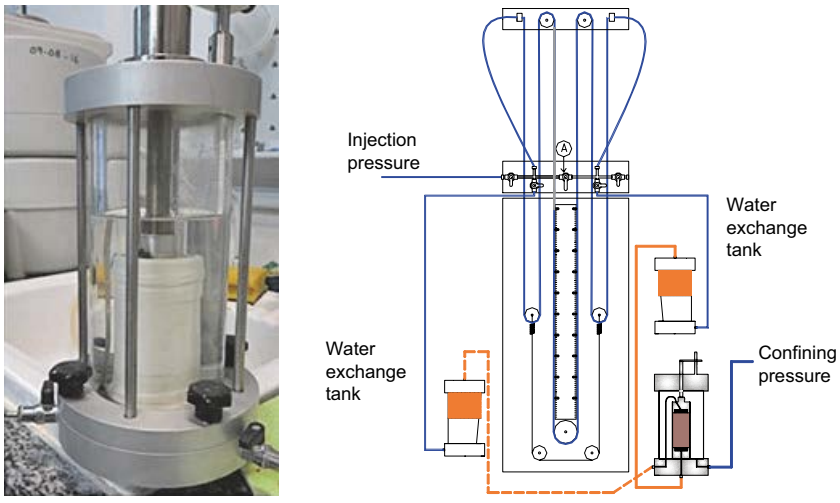

Figure 6-1. *Picture (a) and schematic plot (b) of the triaxial cell and constant load water permeability setup.*

6.1.2 Pressure/volume controller set-up

Likewise, keeping the sample in the same triaxial cell and the same confining pressure, the described measurements performed in the permeameter were alternated with those made in a different setup used to apply injection and backpressure and measure flow at the same time (Figure 6-2).

Once the sample was saturated as explained above, the inlet of the cell connecting to the sample bottom was connected to a constant pressure oil/water pump whose pressure was set to 0.7 MPa. The valve of the cell connecting to the top of the sample was connected to a pressure/volume controller set at a constant pressure of 0.6 MPa while the water outflow was measured. In both setups, exchangers with the equilibrium solution (Table 2-2) were used between the pressure systems on top and bottom of the sample and the triaxial cell inlets. The passage of water was recorded as a function of time until constant flow was reached. Data acquired was used to obtain the hydraulic conductivity by applying Equation (6-1). Although the way of applying the injection and backpressures and the method for outflow measurement differ in both setups, the measurement principle is the same and hence also the equations used to compute permeability.

The use of two different setups allowed testing two samples at the same time as well as cross-checking the values obtained from two different systems to measure outflow (i.e. the permeameter and the pressure/volume controller). Permeability measurements were repeated alternating these two setups until a constant value was obtained. This was considered as the permeability of the sample in equilibrium with the concrete pore solution. At the end of the test, the specimen was disassembled, weighed, measured and dried at 110 ºC for 48 h to determine the final water content (w), the dry density (ρ_d), and the initial and final degrees of saturation (S_r).

The relative error (uncertainty of measurement compared to the measurement itself) of the hydraulic conductivity measured in the permeameter (k_w) represented by Equation (6-1) has four main components: water volume, hydraulic head, dimensions of the sample, and time. The relative error resulting from the combination of the relative uncertainties of these variables was lower than ±1.5 %. In the case of the measurements with the pressure/volume controller setup, the measured variables are pressure, flow, and dimensions of the samples, also yielding a relative error lower than ±1.5 %.

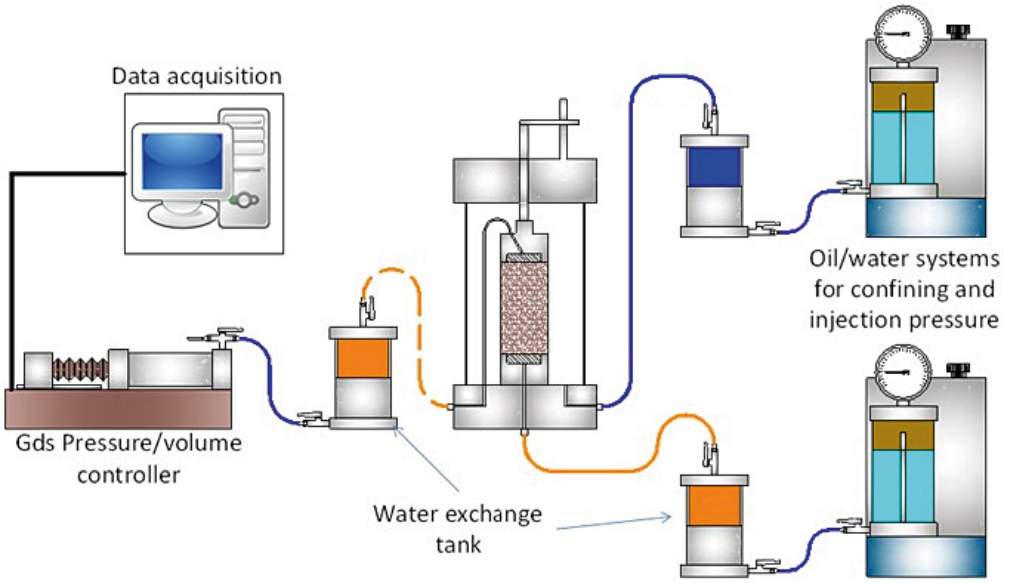

Figure 6-2. *Setup for the measurement of hydraulic conductivity using a pressure/volume controller.*

6.2 Results of hydraulic conductivity tests

6.2.1 ETAPP and TAS05_09 concrete samples

Hydraulic conductivity tests were carried out in triaxial cells with concrete samples obtained after re-drilling the sub-cores ETAPP1, ETAPP2 and TAS05_09. The obtained cylindrical samples were cut in sections and the sub-samples shown in Figure 6-3 were tested. ETAPP2-2-I3 (Figure 6-3 d) sample showed a cavity on the surface which was filled with a filler to avoid piercing of the latex membrane upon confinement (no effect was observed in this sample hydraulic conductivity results).

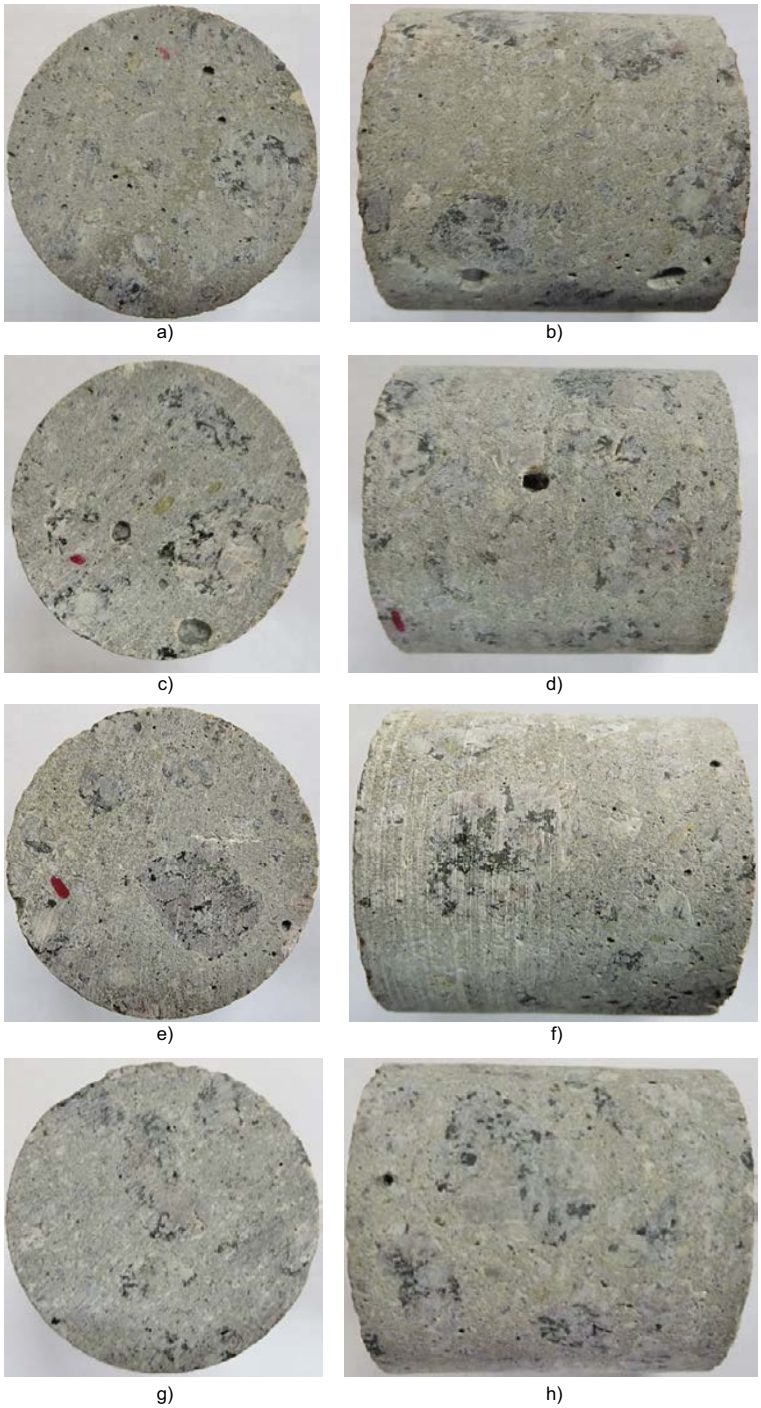

Figure 6-3. *Front and lateral views of sample ETAPP1-6-I3 (a–b); ETAPP2-2-I3 (c–d); ETAPP2-2-S5 (e–f); TAS05_09-A2 (g–h).*

Table 6-1 summarises the characteristics of the specimens tested. Due to the uncertainties in the solid particle density value (Section 4.2.1), the final degree of saturation after the hydraulic conductivity tests was fixed to a value of 100 % and the particle (real) density was computed from Equations (4-5) and (4-6). The values thus obtained were also used to compute the initial degrees of saturation of each sample. This choice is supported by the fact that after several weeks of water injection, it is expected that the degree of saturation of the samples should be close to 100 %.

Table 6-1. Characteristics of the concrete samples used for hydraulic conductivity tests.

Reference	Height (cm)	Diameter (cm)	ρ (kg/m^3)	Initial ρ_d (kg/m^3)	Initial *w* (%)	Initial S_r (%)
ETAPP1-6-I3	5.005	5.048	2360	2230	5.8	79
ETAPP2-2-I3	4.998	5.055	2420	2310	5.0	94
ETAPP2-2-S5	4.829	5.050	2390	2260	5.7	86
TAS05_09-A2	5.099	5.052	2450	2340	4.4	78

All the samples were initially saturated for several days under a confining pressure of 0.8 MPa, injecting the solution through both ends at a pressure of 0.6 MPa. Afterwards, a hydraulic head of 0.1 MPa was applied and the flow was measured. This head resulted in hydraulic gradients of between 191 and 208 m/m. This process was repeated days later to check that the hydraulic conductivity measured was steady.

Figure 6-4 shows hydraulic conductivity values obtained as a function of the time from start of saturation. There is a decreasing trend of permeability with time. This behaviour was already observed in concrete samples using the same experimental setup by Villar et al. (2012, 2014) and previously by other researchers (e.g. Hearn, 1998; Loosveldt et al. 2002). It could be attributed to the slow kinetics of the saturation process and/or to chemical reactions (e.g. continued hydration) taking place during saturation. Hearn (1998) linked this decrease in flow with a decrease in the permeability of concrete caused by self-healing. From these results it seems that, for the size of sample tested and injection pressures applied, more than 40 days are needed to get a steady value. Hence, the value for sample ETAPP2-2-I3, which was only reliably measured after a saturation period of 20 days, was probably not steady.

The obtained results are summarised in Table 6-2. Note that, for ETAPP samples, permeability was measured with the two above described setups, both of which are constant-head permeameters. However, during the first measurements, the permeameter was not working properly and the first values obtained with this equipment have been thus discarded.

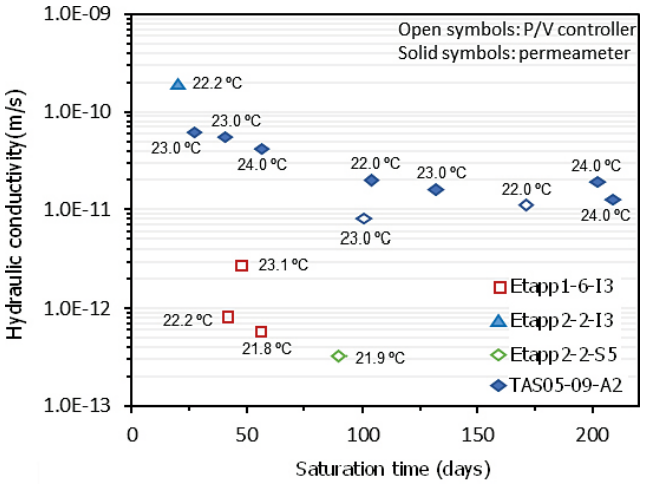

Figure 6-4. *Hydraulic conductivity measured in ETAPP and TAS05_09 samples over time (two different setups were used). Temperature at the time of measurement is also reported.*

Table 6-2. Summary of results from hydraulic conductivity tests for ETAPP and TAS05_09 samples.

Reference	ETAPP 1-6-I3	ETAPP 2-2-I3[b]	ETAPP 2-2-S5	TAS05_09-A2
ρ_d (g/cm^3)	2.23	2.31	2.26	2.34
Porosity [a] (–)	0.167	0.134	0.156	0.133
Initial *w* (%)	5.8	5.0	5.7	4.4
Initial S_r (%)	79	94	86	78
Time [c] (days)	57	20	88	200
Permeameter				
k_w (m/s)		1.9×10^{-10}		
k_{ig} (m^2)		2.0×10^{-17}		
T (°C)		22.2		
P/V controller				
k_w (m/s)	1.4×10^{-12}		3.4×10^{-13}	1.3×10^{-11}
k_{iw} (m^2)	1.4×10^{-19}		3.4×10^{-20}	1.3×10^{-18}
T (°C)	22.4		21.9	22.8
Final *w* (%)	7.5	5.8	6.9	5.7
Final S_r [d] (%)	100	100	100	100

a. Calculated with Equation (4-7); b. Not steady value; c. Since beginning of saturation; d. Assuming final *w* (%) as complete saturation.

6.2.2 OPC and BMA micro-concretes

Four hydraulic conductivity tests were performed in triaxial cells with concrete samples obtained after re-drilling the OPC and the BMA block. The sub-samples shown in Figure 6-5 were used to conduct the tests.

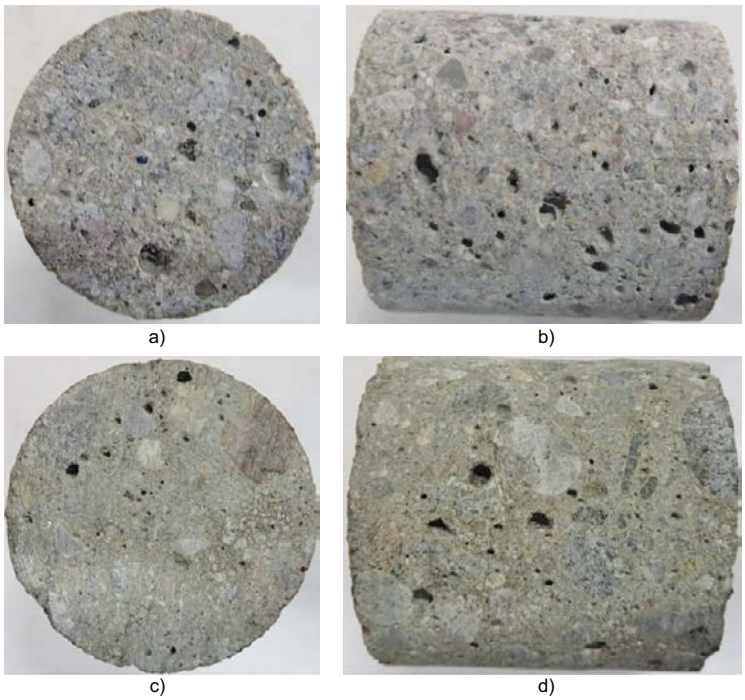

Figure 6-5. *Front and lateral views of sample OPC-P3 (a–b); and BMA-B4 (c–d).*

Table 6-3 summarises the characteristics of the specimens tested. As previously mentioned for ETAPP and TAS05_09 samples, due to the uncertainties in the particle density value (Section 4.2.1), the final degree of saturation was fixed to a value of 100 % and the particle density computed from Equations (4-5) and (4-6). The values thus obtained (Table 6-3) were also used to compute the initial degrees of saturation of each sample.

Table 6-3. Characteristics of the concrete samples used for hydraulic conductivity tests.

Reference	Height (cm)	Diameter (cm)	ρ (kg/m^3)	Initial ρ_d (kg/m^3)	Initial w (%)	Initial S_r (%)
OPC-P3	5.090	3.733	2250	2170	3.7	48
BMA-B4	5.026	5.059	2300	2190	5.6	62

The procedure of testing OPC and BMA samples was the same as previously detailed for ETAPP and TAS05_09. Figure 6-6 shows the permeability values obtained as a function of the time from start of saturation. As previously seen in the limestone concrete samples, there is a decreasing trend of permeability in the samples with saturation time which can be associated to the slowness of the saturation process and/or to chemical reactions taking place during saturation. The results suggest that for the size of sample tested and the applied injection pressures, more than 80 days are needed to get a steady value. The results obtained are summarised in Table 6-4, where the equilibrium hydraulic conductivity values are shown. Note that, for OPC-P3 sample, permeability was measured with the two above described setups, with consistent values.

Table 6-4. Summary of the hydraulic conductivity results for OPC and BMA samples.

Reference	OPC-P3	BMA-B4
ρ_d (kg/m^3)	2170	2190
Porosity [a] (–)	0.171	0.177
Initial w (%)	3.7	5.0
Initial S_r (%)	48	62
Time [b] (days)	48	83
Permeameter		
k_w (m/s)	2.0×10^{-11}	
k_{iw} (m^2)	2.0×10^{-18}	
T (°C)	22.6	
P/V controller		
k_w (m/s)	1.3×10^{-11}	1.9×10^{-11}
k_{iw} (m^2)	1.3×10^{-18}	2.0×10^{-18}
T (°C)	22.3	21.8
Final w (%)	7.9	8.1
Final S_r [c] (%)	100	100

a. Calculated with Equation (4-7); b. Since beginning of saturation; c. Assuming final w (%) as complete saturation.

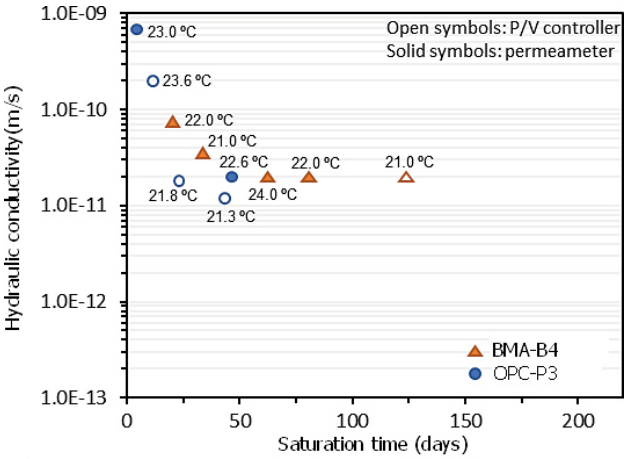

Figure 6-6. *Hydraulic conductivity measured in OPC and BMA samples over time (two different setups were used). Temperature at the time of measurement is also reported.*

7 HTO Diffusion Experiments

7.1 Experimental method and analytical approach

Among the different experimental methods to determine diffusivity in cement-based materials, the most common are through-diffusion and in-diffusion. The former is based on flux determination, while the latter entails the measuring of concentration profiles in the solid sample.

Diffusion coefficients can be determined under two regimens: steady-state and transient. In-diffusion is a transient method, whereas through-diffusion can be performed under both regimes. Steady-state method is more time-consuming and requires maintaining the concentration gradient constant but is considered more accurate. For this reason, in the present work, steady-state through-diffusion (TD) experiments were conducted as described by Van Loon et al. (2003) and Descostes et al. (2008). According to this method, the concrete sample is placed inside a diffusion cell between two reservoirs, named "inlet" and "outlet", where the equilibrium porewater is continuously stirred (Figure 7-1). Once the concrete sample is saturated (approximately 3 weeks are required to complete saturation), the inlet reservoir is spiked in this case with tritiated water (HTO), a neutral tracer. HTO has been preferred over other tracers due to its conservative properties.

Concentrations in both reservoirs are kept constant so that steady-state diffusion across the sample can be reached. At this point, the diffusive flux across the concrete specimen is constant. Different experimental approaches can be employed to maintain the concentration gradient constant, i.e. (i) by spiking additional tracer in the inlet reservoir or (ii) by using large volumes of equilibrium porewater to minimize the concentration decrease; and (i) by carrying out frequent sampling in the outlet reservoir to maintain the concentration near to zero or (ii) by changing the outlet container periodically. In the present study, the experimental procedure consisted on the use of a large volume (1 000 ml) inlet reservoir and very small (20 ml) outlet reservoir, which is periodically changed. In these experiments the first samplings were performed one and three days after the starting of the experiment, and the rest of sampling every week.

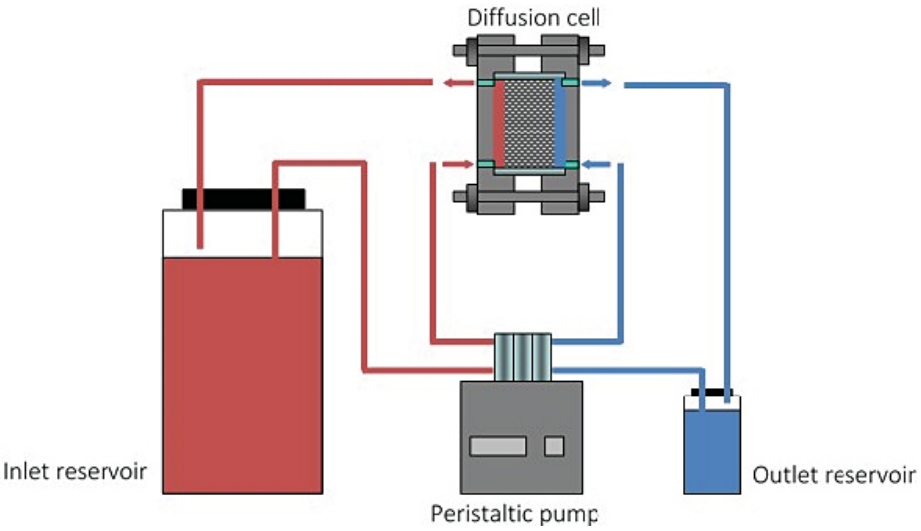

Figure 7-1. *Schematic diagram of the experimental setup for through-diffusion experiments.*

The initial and boundary conditions of the HTO through-diffusion experiment across the axis of the cylindrical concrete sample (x coordinate), which is initially tracer-free, are (small variations at both boundaries are allowed):

- Initial condition:
  C(x, t) = 0 $\forall$x and t ≤ 0
- Boundary conditions:
  At the high concentration side: C(0, t) = C_0 (= constant) t > 0
  At the low concentration side: C(L, t) = 0 t > 0

The concentration profile in the sample at time *t* can be calculated using the following analytical expression (Crank, 1975):

$$c(x,t) = c_0 \cdot \left[1 - \frac{x}{L} - \frac{2}{\pi}\sum_{n=1}^{\infty}\frac{1}{n}\cdot sin\frac{n\pi x}{L}\,exp\left(-\frac{D_a \cdot n^2 \cdot \pi^2}{L^2}\cdot t\right)\right] \quad (7\text{-}1)$$

where D_a (m²/s) is the apparent diffusion coefficient, c_0 (count per minute per millilitre, cpm/ml) is the initial concentration, and L (m) is the thickness of the sample.

The flux across the low-concentration side, at x = L, is in turn calculated as follows (Thoma et al. 1993; Grathwohl, 1998; Jakob et al. 1999):

$$j(L,t) = -\phi_{acc}\cdot D_e \left.\frac{\partial c}{\partial x}\right|_{x=L} = c_0\frac{D_e}{L}\left(1 + 2\sum_{n=1}^{\infty}(-1)^n exp\left|\frac{-n^2\pi^2 D_e t}{\alpha L^2}\right|\right) \quad (7\text{-}2)$$

where D_e (m²/s) is the effective diffusion coefficient and ϕ_{acc} (–) is the accessible porosity of the sample. There is a transient behaviour of the system at short times which lasts until the porosity is filled up with the tracer and the concentration of the solution and solid (if adsorption takes place) reaches equilibrium. At this point, a linear concentration gradient is established along the sample thickness, and diffusion reaches the steady-state with a constant flux (mol·m^{-2}·s^{-1}), given by Equation (7-3), regardless any retarding mechanisms such as adsorption. For this reason, TD experiments are very time-consuming when non-conservative tracers are used.

$$j_L = \frac{c_0 \cdot D_e}{L} \quad (7\text{-}3)$$

Integrating the flux with respect to time and multiplying it by the cross-sectional area A (m²) of the sample yields the total diffused mass of tracer (or cumulative mass in the low concentration reservoir), Q (cpm), in the linear sorption case (Crank, 1975; Bourke et al. 1993):

$$Q = A \cdot L \cdot c_0 \cdot \left[\frac{D_e}{L^2}t - \frac{\alpha}{6} - \frac{2\alpha}{\pi^2}\sum_{n=1}^{\infty}\frac{(-1)^n}{n^2}\cdot exp\left(-\frac{D_e \cdot n^2 \cdot \pi^2}{L^2 \cdot \alpha}\cdot t\right)\right] \quad (7\text{-}4)$$

where α is the capacity factor given by

$$\alpha = \phi_{acc} + \rho_d \cdot K_d \quad (7\text{-}5)$$

In Equation 7-5, ρ_d is the dry density of the sample (kg·dm^{-3}) and K_d is the distribution coefficient (dm^3·kg^{-1}). For non-sorbing tracers such as HTO, $K_d \approx 0$ and the capacity factor is equivalent to the accessible porosity. The relation between D_a and D_e is given by Equation (7-6).

$$D_a = \frac{D_e}{\phi_{acc} + \rho_d \cdot K_d} = \frac{D_e}{\alpha} \quad (7\text{-}6)$$

For sufficiently long periods of time, a steady-state condition is reached and the series expansion in Equation (7-4) vanishes (the exponential term tends to zero), obtaining a linear relationship between Q and t (7-7).

$$Q = A \cdot L \cdot c_0 \cdot \left[\frac{D_e}{L^2}t - \frac{\alpha}{6}\right] \quad (7\text{-}7)$$

Thus, the effective diffusion coefficient can be calculated from the slope of the straight line fitting the long-term behaviour of Q as a function of time in cpm/s as given by Equation (7-8). This simplified expression is normally used for calculating the D_e coefficient in TD experiments.

$$D_e = \frac{slope \cdot L}{A \cdot c_0} \quad (7\text{-}8)$$

The intercept of Equation (7-8) with the time axis (i.e. for $Q = 0$) is denoted as time-lag (t_e) and is approximately 2/3 of the time necessary to reach steady-state conditions (Crank, 1975):

$$t_e = \frac{L^2 \cdot \alpha}{6 \cdot D_e} \quad (7\text{-}9)$$

From Equation (7-9), the capacity factor (and the accessible porosity if a conservative tracer is used) can be calculated using Equation (7-10).

$$\alpha = 6 \frac{D_e \cdot t_e}{L^2} \quad (7\text{-}10)$$

It is noted that the accessible porosity values derived from this method (TD) may not represent accurate estimations when the time-lag value calculation is subject to changes (see e.g. Jakob et al. 1999).

From a practical point of view, it is not always easy to maintain the inlet and outlet reservoirs at constant concentration as a function of time. Thus, slight variations of concentration are generally accepted within the reservoirs while preserving the validity of the analytical solution. For the experiments, the approximate threshold of concentration variation was assumed to be ±10 % in both reservoirs.

7.2 Experimental set-up

Diffusion experiments were carried out using HTO as tracer. The concrete porewater used for the tests was prepared according to the description given in Section 2.3 (composition of these solutions is given in Table 2-2). The HTO activity was measured by liquid scintillation counting (LSC) using a Tri Carb 4910TR Perkin Elmer liquid scintillation counter and Ultima Gold (Perkin Elmer) as scintillation cocktail. Calibrations were previously carried out with standards of known activity and the same geometry of the samples. The HTO activity used in the inlet-reservoir was in the range 1 350–1 560 cpm/mL (count per minute per millilitre), which is equivalent to $(1.0–1.1) \times 10^{-10}$ M (taking into account the specific activity of tritium and the detector counting efficiency). This activity has proven to be sufficient to perform reliable experiments.

Through-diffusion (TD) experiments were performed on ETAPP1, ETAPP2, TAS05_09, OPC and BMA concrete samples. Selection criteria was based on visual inspection, being the selected sub-samples those showing more homogeneity with smaller and more regular pores. Besides, when possible, the presence of larger aggregates than the height of the sample was avoided. Table 7-1 summarizes the experiments carried out for each type of material as well as the dimensions and original location of tested sub-samples. Selected sub-samples for diffusion experiments were sealed with an epoxy resin (Epofix, Struers GmbH) in PVC diffusion rings. The rings were mounted in PVC diffusion cells inside a glove box under N_2 atmosphere at O_2 and $CO_2 < 1$ ppm (Figure 7-2).

Table 7-1. Materials and sub-samples selected for diffusion tests. The reference name of each sub-sample, its location in the original sub-core specimen, dimensions and weight are included.

Material	Sub-sample	Location (mm from surface)	Diameter (mm)	Height (mm)	Weight (g)
ETAPP1	ET1-8	173.0	50.0	18.1	85.8
	ET1-13	279.0	50.0	17.4	81.2
ETAPP2	ET2-2	53.0	50.0	16.9	80.6
	ET2-12	262.0	50.0	17.3	84.0
TAS05_09	TAS05_09 B2	198.7	50.0	17.9	86.3
	TAS05_09 B4	241.1	50.0	17.6	86.3
	TAS05_09 B5	261.7	50.0	17.7	86.3
OPC	OPC-1	10.0	50.0	17.6	87.1
	OPC-2	31.0	50.0	19.1	90.0
BMA	BMA 1	8.0	50.0	18.6	87.2
	BMA 2	22.4	50.0	18.0	82.8
	BMA 7	129.8	50.0	18.7	85.9

a) b)

Figure 7-2. *Experimental setup of diffusion cells into the glove box (a); detail of the setup with the inlet and outlet reservoirs at both sides of the diffusion cell (b).*

7.3 Results of diffusion tests

7.3.1 ETAPP and TAS05_09 concrete samples

7.3.1.1 ETAPP1

Two TD experiments were performed with limestone concrete from the first casting, ETAPP1. The tests lasted 142 and 122 days for ET1-8 and ET1-13 sub-samples, respectively (Figure 7-3).

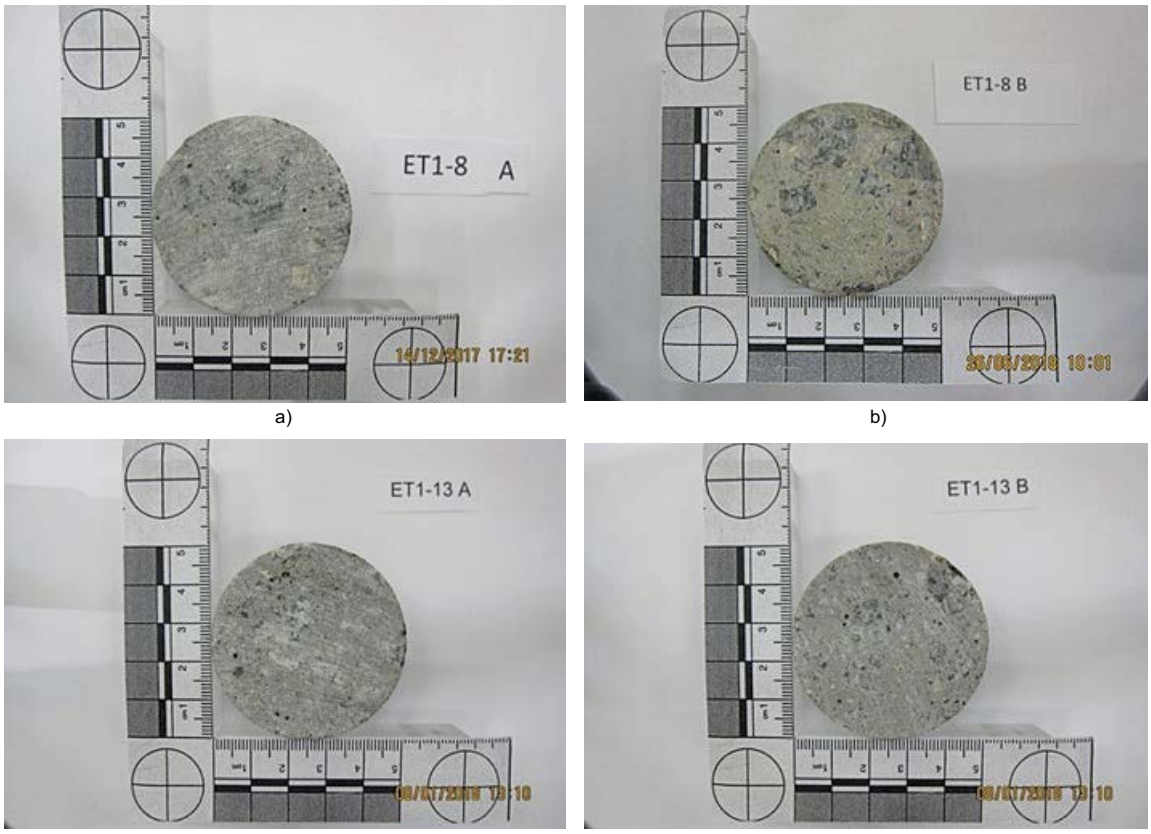

a) b)

c) d)

Figure 7-3. *Appearance of both sides of samples ET1-8 (a–b) and ET1-13 (c–d).*

Figure 7-4 a–b shows the experimentally measured cumulative mass and the fits obtained for ET1-8 and ET1-13 samples under transient- and steady-state conditions, using Equations (7-4) and (7-8), respectively. Obtained effective diffusion coefficients and accessible porosity under these two regimes are given in Table 7-2.

Figure 7-5 a–b shows the obtained HTO flux (cpm·cm^{-2}·h^{-1}) against time (in hours). Linear fitting has been calculated by using Equation (7-2), considering the values of D_e and porosity obtained from the fit of the cumulative mass using Equation (7-4). All experimental data obtained from ET1-8 and ET1-13 samples are listed in Appendix E.

Table 7-2. Calculated effective diffusion coefficients and accessible porosity at steady-state (7-8) and transient-state (7-4) conditions for ET1-8 and ET1-13 samples.

	ET1-8			ET1-13		
Regime	**R^2**	**D_e (m^2/s)**	**ϕ_{acc}**	**R^2**	**D_e (m^2/s)**	**ϕ_{acc}**
Steady	0.9998	5.30×10^{-12}	0.21	0.9999	6.42×10^{-12}	0.27
Transient	-	5.40×10^{-12}	0.22	-	6.31×10^{-12}	0.25

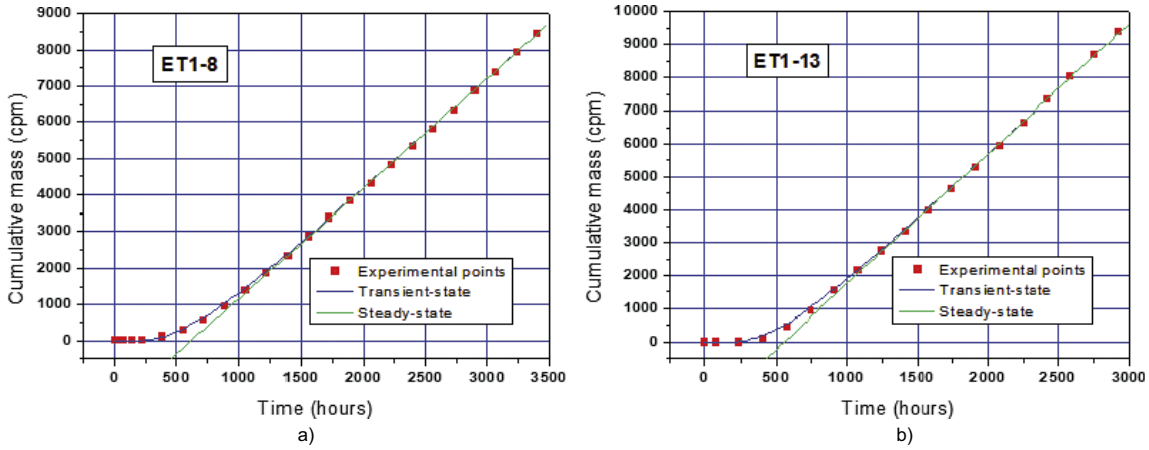

Figure 7-4. Cumulative mass (cpm) vs. time (hours) and fit of the steady-state region and transient-state in samples ET1-8 (a) and ET1-13 (b).

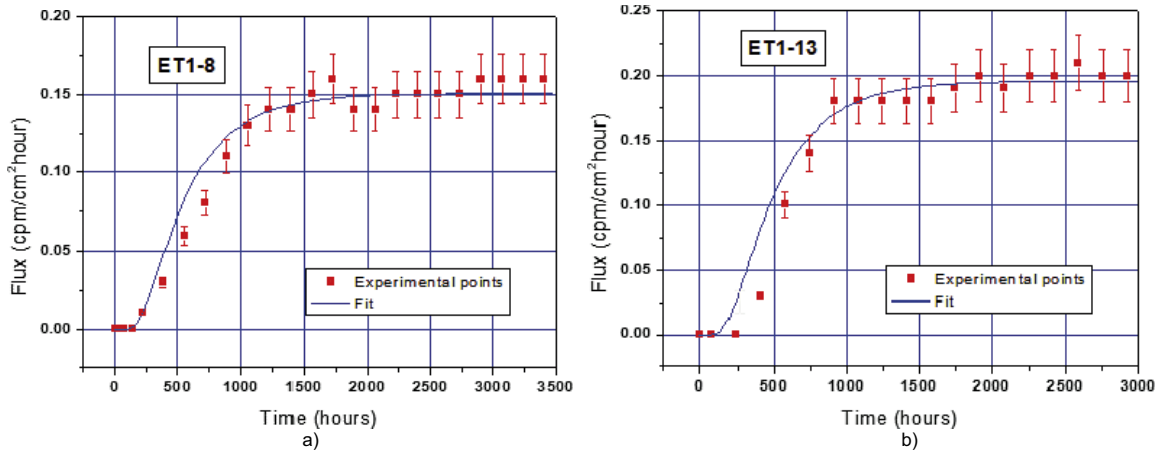

Figure 7-5. HTO flux in cpm·cm^{-2}·h^{-1} (cpm stands for counts per minute) vs. time (hours) for the through diffusion experiment with samples ET1-8 (R^2 = 0.978) (a) and ET1-13 (R^2 = 0.928) (b).

7.3.1.2 ETAPP2

Two TD experiments were performed with limestone concrete from the second casting, ETAPP2. The tests lasted 135 and 121 days for ET2-2 and ET2-12 sub-samples, respectively (Figure 7-6 a–d). Figure 7-7 shows the experimental results concerning cumulative mass and the fits obtained for ET2-2 and ET2-12 samples under transient- and steady-state conditions. Calculated effective diffusion coefficients and accessible porosity under these two regimes (Equations 7-4 and 7-8) are given in Table 7-3. Figure 7-8 a–b shows the experimental and fitted HTO flux (cpm·cm^{-2}·h^{-1}) against time (in hours). All experimental data obtained from ET2-2 and ET2-12 samples are listed in Appendix E.

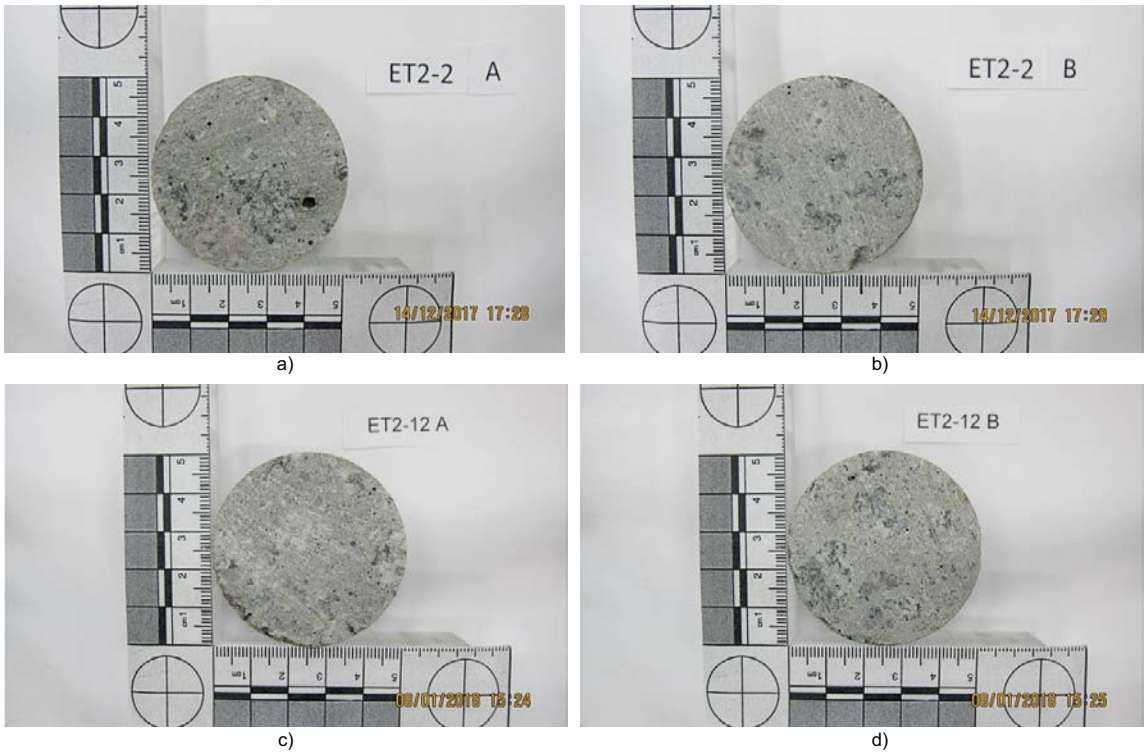

Figure 7-6. *Appearance of both sides of samples ET2-2 (a–b) and ET2-12 (c–d).*

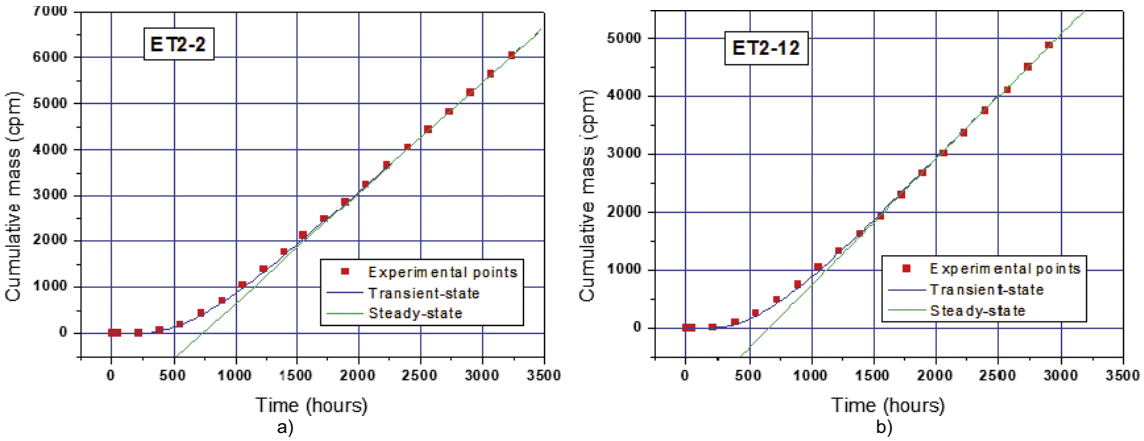

Figure 7-7. *Cumulative mass (cpm) vs. time (hours) and fit of the steady-state region and transient-state in samples ET2-2 (a) and ET2-12 (b).*

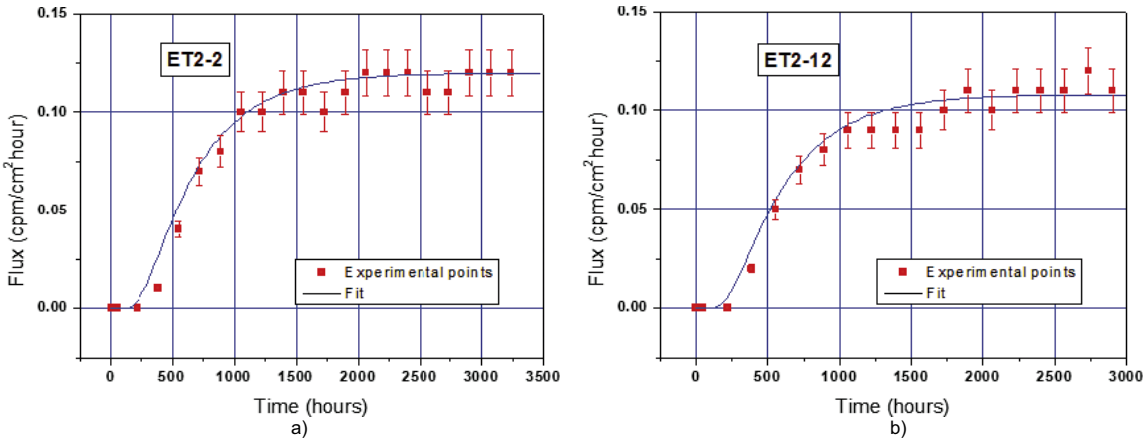

Figure 7-8. *HTO flux in cpm·cm^{-2}·h^{-1} (cpm stands for counts per minute) vs. time (hours) for the through diffusion experiment with samples ET2-2 (R^2 = 0.977) (a) and ET2-12 (R^2 = 0.999) (b).*

Table 7-3. Calculated effective diffusion coefficients and accessible porosity at steady-state (7-8) and transient-state (7-4) conditions for ET2-2 and ET2-12 samples.

	ET2-2			ET2-12		
Regime	**R^2**	**D_e (m^2/s)**	**ϕ_{acc}**	**R^2**	**D_e (m^2/s)**	**ϕ_{acc}**
Steady	0.9999	4.06×10^{-12}	0.21	0.9997	3.61×10^{-12}	0.18
Transient	-	4.17×10^{-12}	0.23	-	3.58×10^{-12}	0.17

7.3.1.3 TAS05_09

Three TD experiments were performed with TAS05_09 concrete sample. The tests lasted 142 days for the three sub-samples tested, i.e. TAS05_09 B2, TAS05_09 B4 and TAS05_09 B5 (Figure 7-9 a–f). Figure 7-10 a–c shows the experimental results regarding cumulative mass of HTO as well as the fits for TAS05_09 B2, B4 and B5 samples under transient- and steady-state conditions. Calculated effective diffusion coefficients and accessible porosity under these two regimes are listed in Table 7-4. Figure 7-11 a–c shows the experimentally obtained and modelled HTO flux (cpm·cm^{-2}·h^{-1}) against time (in hours). All experimental data obtained from tested TAS05_09 samples are listed in Appendix E.

Table 7-4. Calculated effective diffusion coefficients and accessible porosity at steady-state (7-8) and transient-state (7-4) conditions for TAS05_09 B2, TAS05_09 B4 and TAS05_09 B5 samples.

	TAS05_09 B2			TAS05_09 B4			TAS05_09 B5		
Regime	**R^2**	**D_e (m^2/s)**	**ϕ_{acc}**	**R^2**	**D_e (m^2/s)**	**ϕ_{acc}**	**R^2**	**D_e (m^2/s)**	**ϕ_{acc}**
Steady	0.9999	4.80×10^{-12}	0.10	0.9999	4.72×10^{-12}	0.09	0.9998	4.56×10^{-12}	0.06
Transient	-	5.01×10^{-12}	0.14	-	4.81×10^{-12}	0.11	-	4.82×10^{-12}	0.12

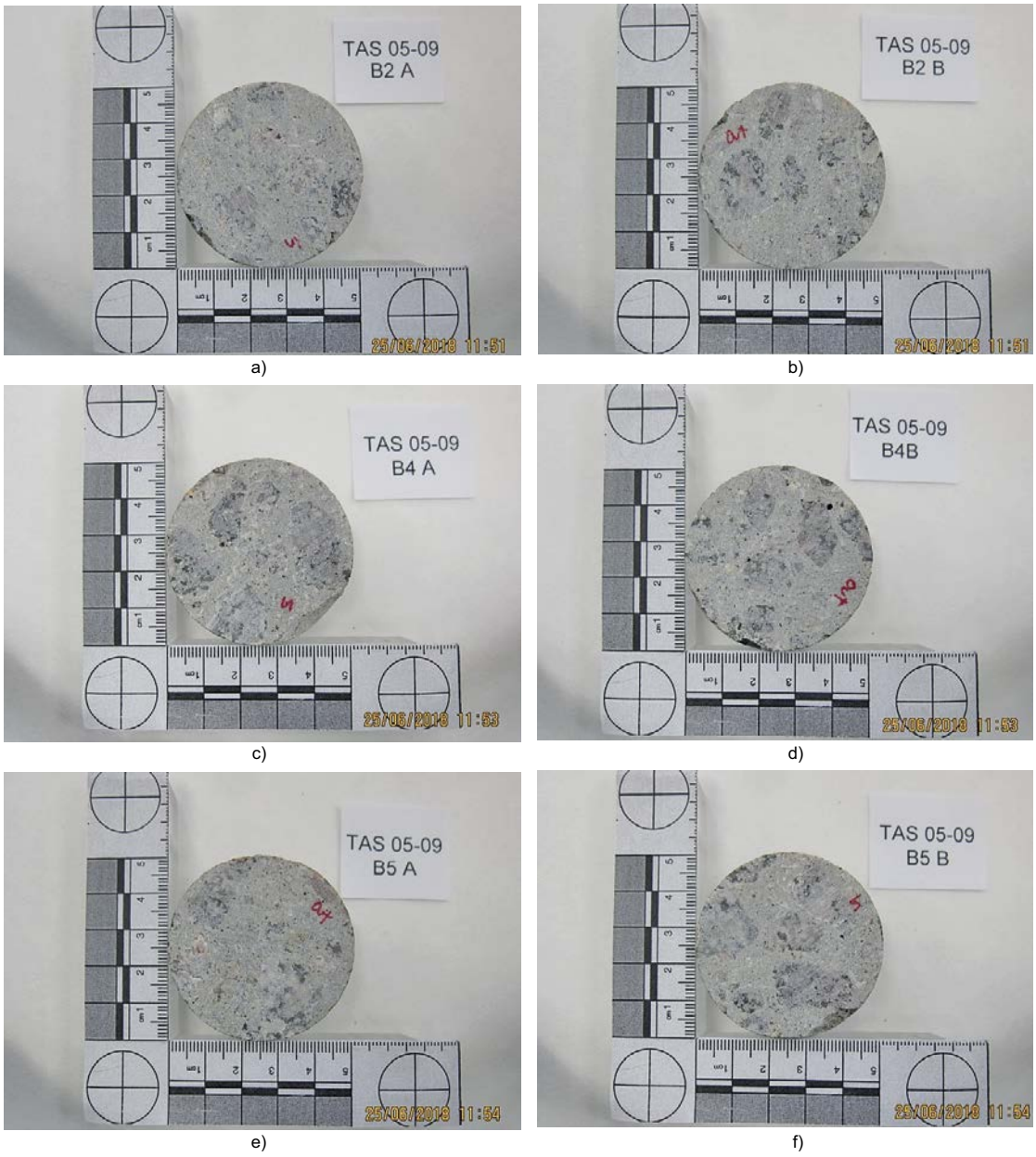

Figure 7-9. *Appearance of both sides of samples TAS05_09 B2 (a–b); TAS05_09 B4 (c–d) and TAS05_09 B5 (e–f).*

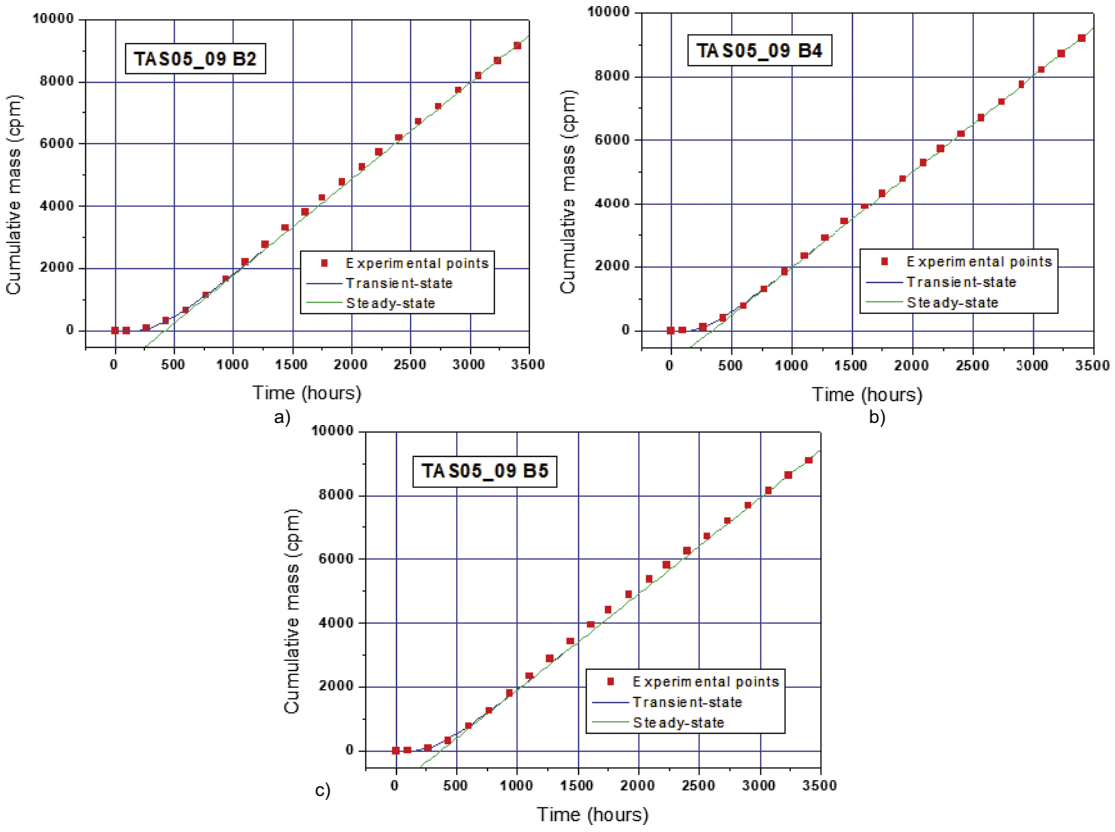

Figure 7-10. *Cumulative mass (cpm) vs. time (hours) and fit of the steady-state region and transient-state in samples TAS05_09 B2 (a); TAS05_09 B4 (b) and TAS05_09 B5 (c).*

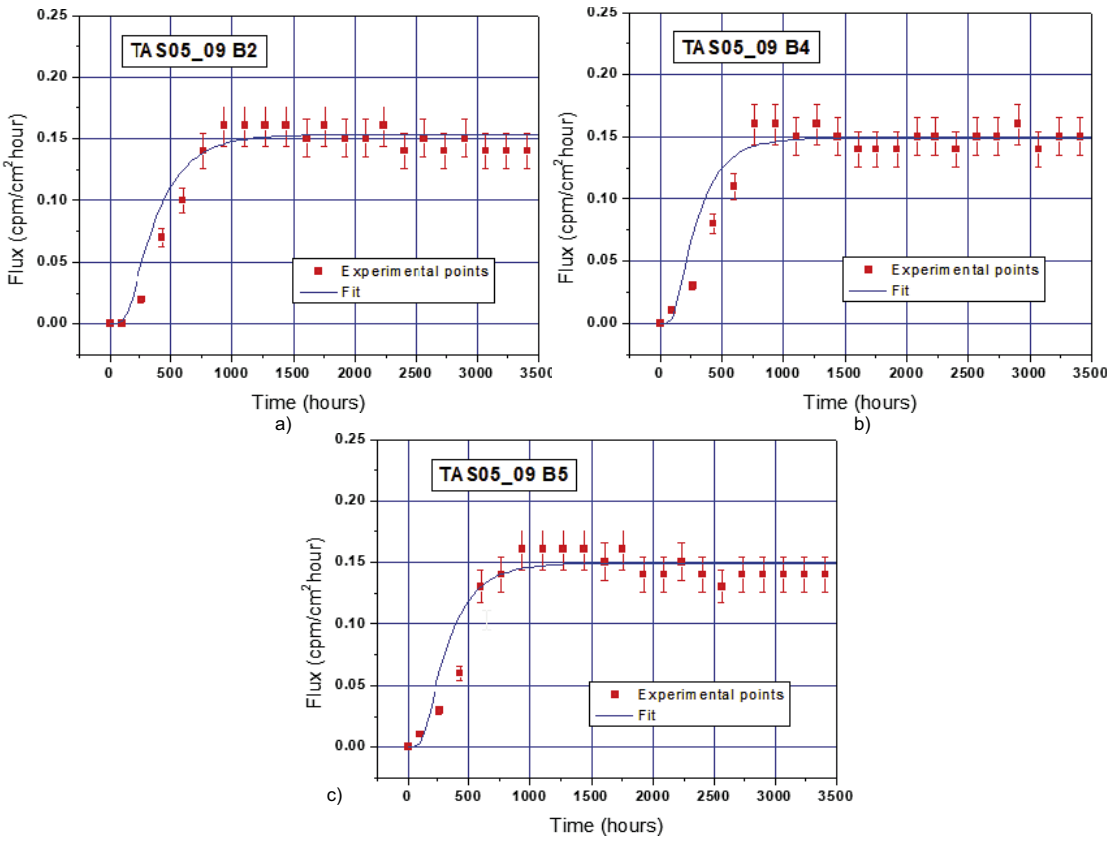

Figure 7-11. *HTO flux in cpm·cm^{-2}·h^{-1} vs. time (hours) for the through diffusion experiment with samples TAS05_09 B2 (R^2 = 0.982) (a); TAS05_09 B4 (R^2 = 0.969) (b) and TAS05_09 B5 (R^2 = 0.972) (c).*

7.3.2 OPC and BMA micro-concretes

7.3.2.1 OPC-1 and OPC-2

Two TD experiments were performed with OPC micro-concrete sample. The tests lasted 165 days for both OPC-1 and OPC-2 tested sub-samples (Figure 7-12 a–d). Figure 7-13 a–b shows the cumulative mass of HTO experimentally obtained and the fits for OPC-1 and OPC-2 samples under transient- and steady-state conditions. Calculated effective diffusion coefficients and accessible porosity under these two regimes are listed in Table 7-5. Figure 7-14 a–b shows the experimentally obtained and modelled HTO flux (cpm·cm^{-2}·h^{-1}) against time (in hours). All experimental data obtained from OPC samples are listed in Appendix E.

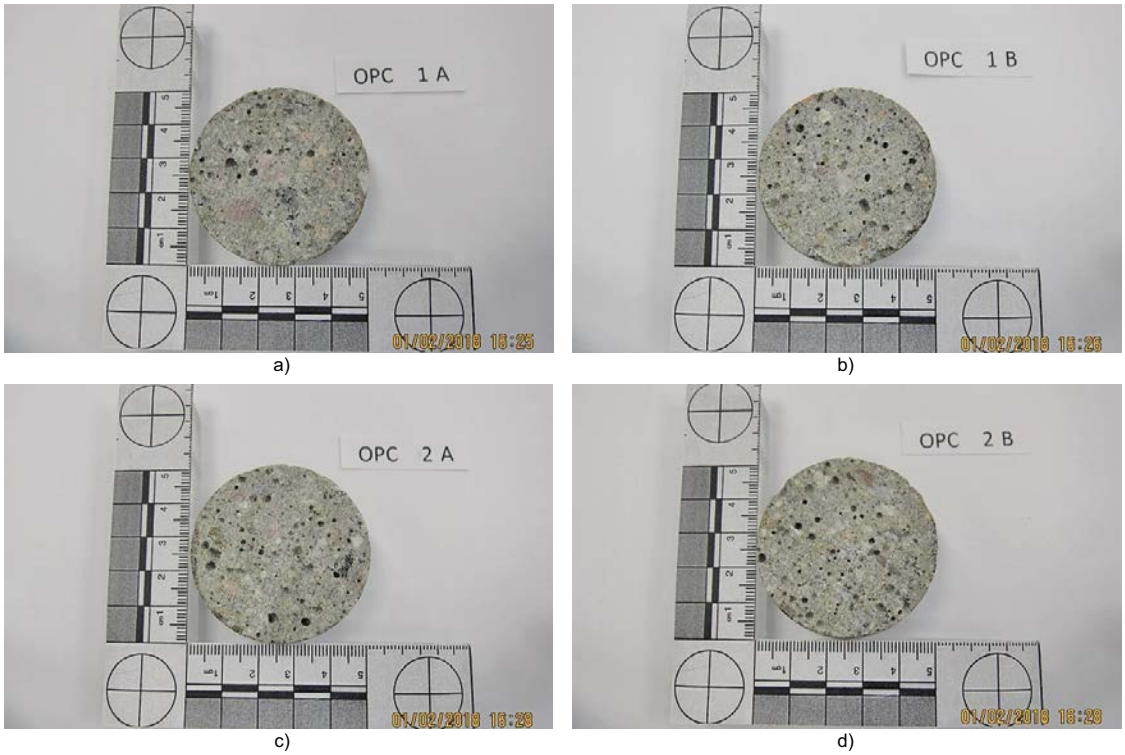

Figure 7-12. *Appearance of both sides of samples OPC-1 (a–b) and OPC-2 (c–d).*

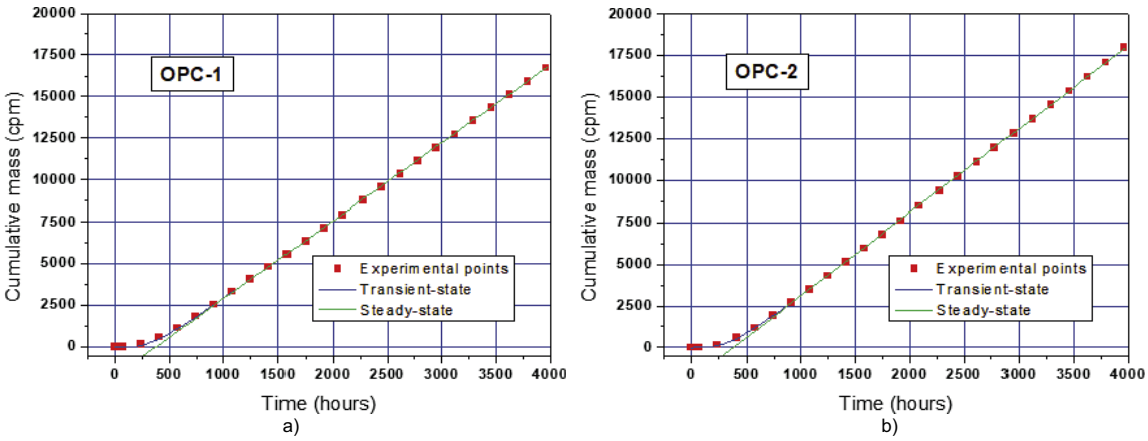

Figure 7-13. *Cumulative mass (cpm) vs. time (hours) and fit of the steady-state region and transient-state in samples OPC-1 (a) and OPC-2 (b).*

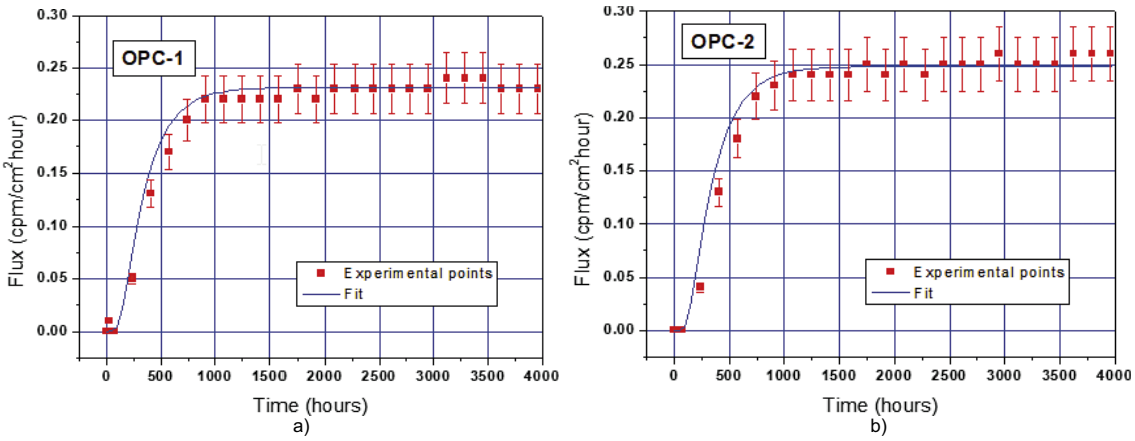

Figure 7-14. HTO flux in cpm·cm^{-2}·h^{-1} (cpm stands for counts per minute) vs. time (hours) for the through diffusion experiment with samples OPC-1 ($R^2 \approx 1.0$) (a) and OPC-2 ($R^2 = 0.995$) (b).

Table 7-5. Calculated effective diffusion coefficients and accessible porosity at steady-state (7-8) and transient-state (7-4) conditions for OPC-1 and OPC-2 samples.

	OPC-1			OPC-2		
Regime	**R^2**	**D_e (m²/s)**	**ϕ_{acc}**	**R^2**	**D_e (m²/s)**	**ϕ_{acc}**
Steady	1.000	7.39×10^{-12}	0.21	1.000	8.66×10^{-12}	0.22
Transient	-	7.29×10^{-12}	0.19	-	8.49×10^{-12}	0.19

7.3.2.2 BMA1, BMA2 and BMA7

Three TD experiments were performed with the BMA concrete sample. The tests lasted 114 days for the three sub-samples tested, i.e. BMA 1, BMA 2 and BMA 7 (Figure 7-15 a–d). Figure 7-16 a–c shows the experimentally obtained cumulative mass of HTO and the fits for the BMA samples under transient- and steady-state conditions. Calculated effective diffusion coefficients and accessible porosity under these two regimes are listed in Table 7-6. Figure 7-17 a–c shows the experimentally obtained and modelled HTO flux (cpm·cm^{-2}·h^{-1}) against time (in hours). All experimental data obtained from BMA samples are comprised in Appendix E.

Table 7-6. Calculated effective diffusion coefficients and accessible porosity at steady-state (7-8) and transient-state (7-4) conditions for BMA 1, BMA 2 and BMA 7 samples.

	BMA 1			BMA 2			BMA 7		
Regime	**R^2**	**D_e (m²/s)**	**ϕ_{acc}**	**R^2**	**D_e (m²/s)**	**ϕ_{acc}**	**R^2**	**D_e (m²/s)**	**ϕ_{acc}**
Steady	0.9998	9.09×10^{-12}	0.11	0.9999	9.66×10^{-12}	0.14	1.000	9.11×10^{-12}	0.11
Transient	-	9.33×10^{-12}	0.15	-	9.68×10^{-12}	0.15	-	9.14×10^{-12}	0.15

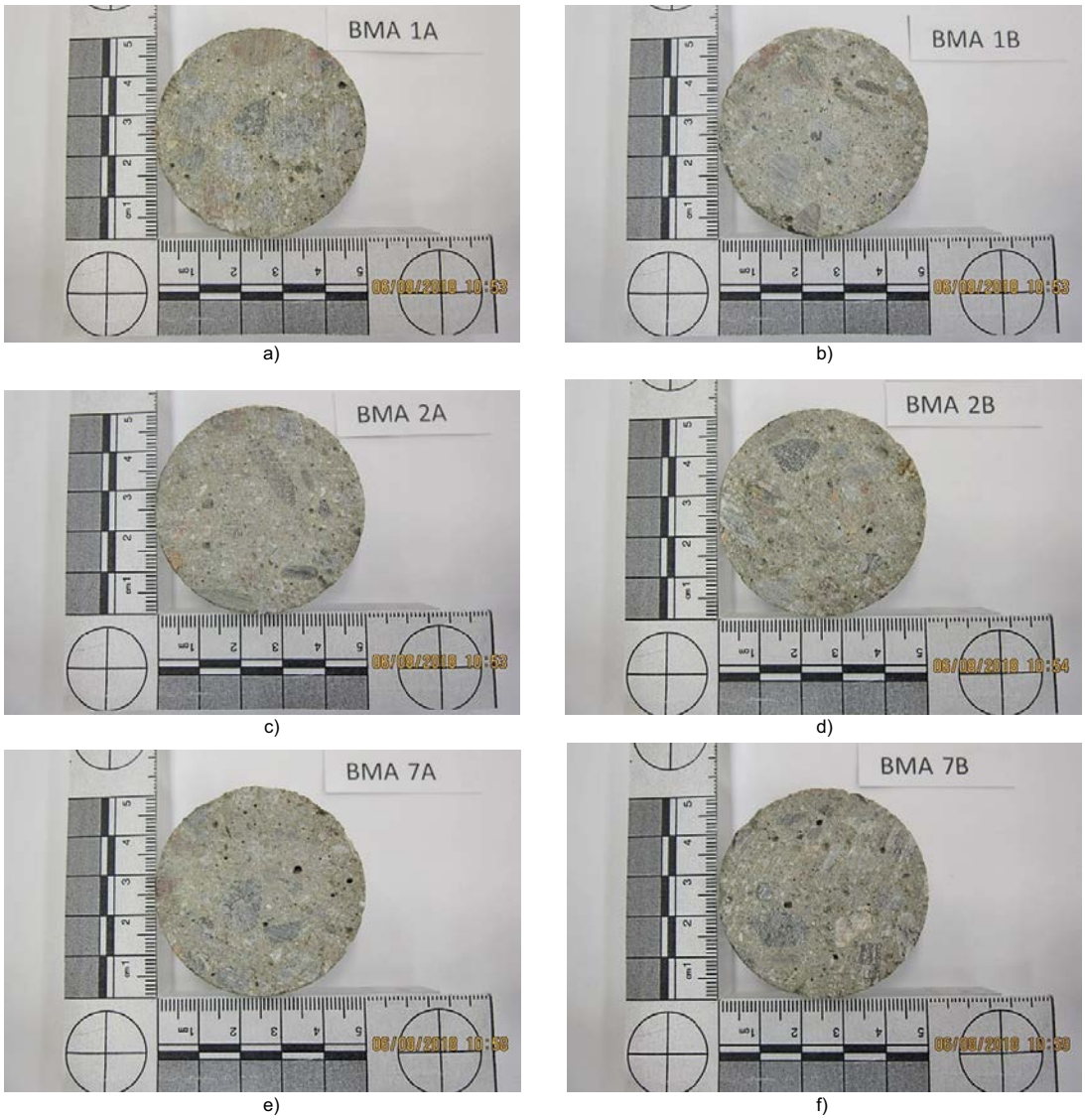

Figure 7-15. *Appearance of both sides of samples BMA 1 (a–b); BMA 2 (c–d) and BMA 7 (e–f).*

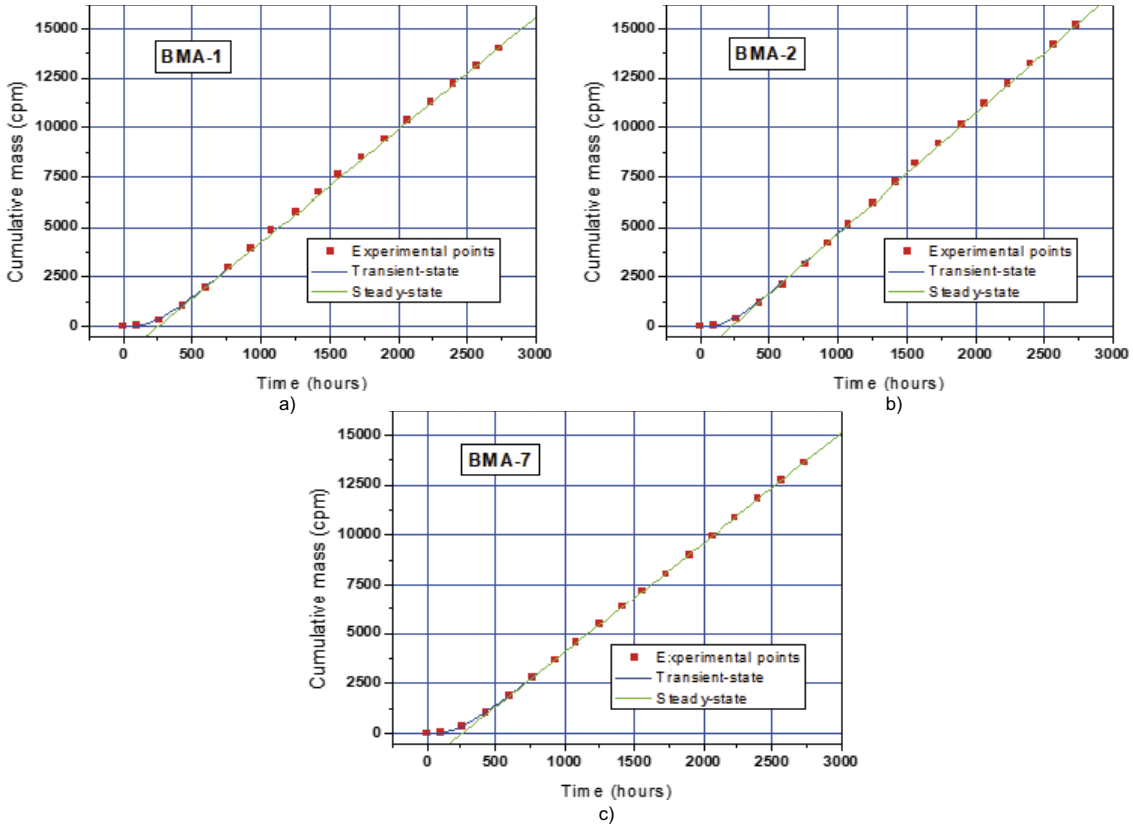

Figure 7-16. *Cumulative mass (cpm) vs. time (hours) and fit of the steady-state region and transient-state in samples BMA 1 (a); BMA 2 (b) and BMA 7 (c).*

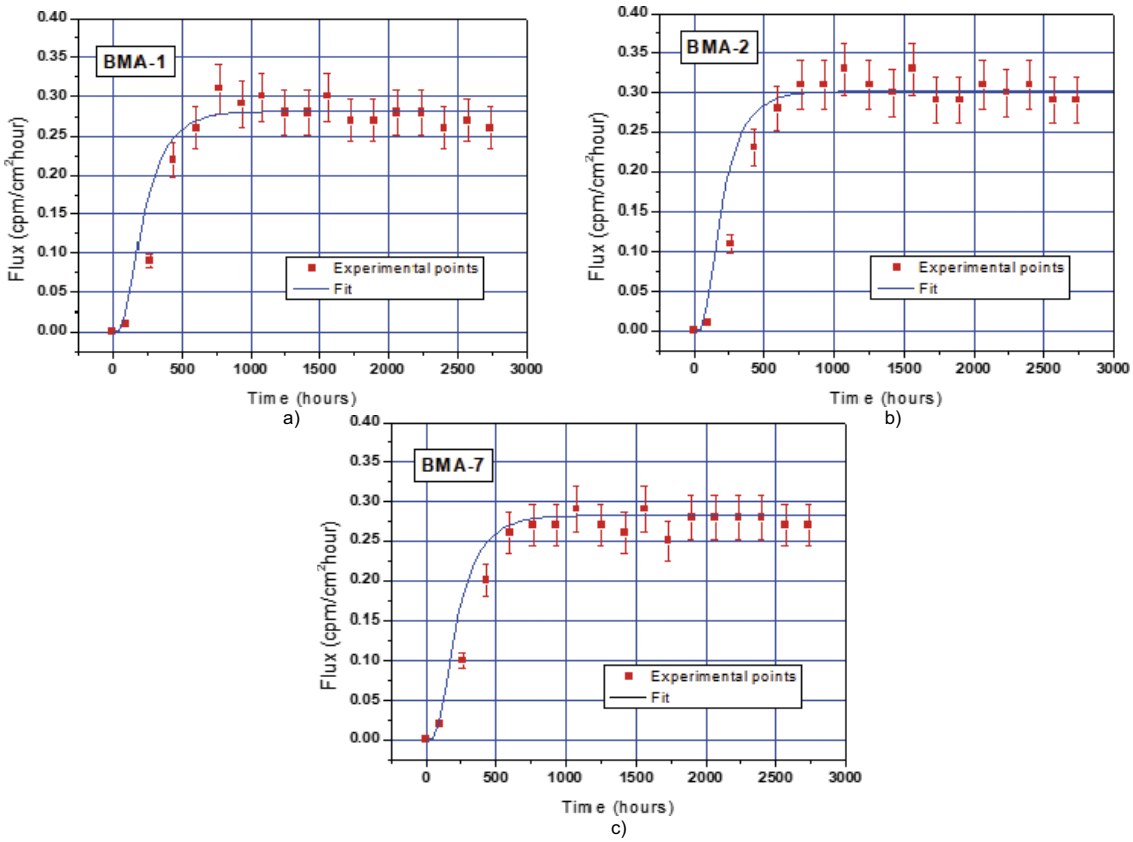

Figure 7-17. *HTO flux in cpm·cm^{-2}·h^{-1} (cpm stands for counts per minute) vs. time (hours) for the through diffusion experiment with samples BMA 1 (R^2 = 0.936) (a); BMA 2 (R^2 = 0.967) (b) and BMA 7 (R^2 ≈ 1.0) (c).*

7.4 Summary of the results and uncertainty estimations

Figure 7-18 comparatively shows the effective diffusion coefficients of all the sub-samples tested. Results show a general lower diffusivity for the limestone concrete samples (ETAPP and TAS05_09) compared to the samples without limestone filler (OPC micro-concrete and BMA). Similar D_e values have been obtained between TAS05_09 and ETAPP samples, although with remarkable differences in terms of porosity.

It is noteworthy to mention that TD experiments are typically analysed using the approximate solution presented in Equation (7-7). This analytical solution is obtained from two boundary conditions: constant concentration gradient and zero concentration in the outlet reservoir. Although these two conditions cannot be perfectly satisfied from an experimental point of view, the associated uncertainty can be estimated.

The overall uncertainty for the values in the TD measurements results from the uncertainty on the parameters involved to calculate these values (Ellison et al. 2000). When using the approximate solution given by Equation (7-7), D_e is calculated from the slope of the straight-line fitting (y = a·t+b) the long-term behaviour of Q as a function of time, Equation (7-8). Therefore, the capacity factor can be defined as follows (Equation 7-11):

$$\alpha = -\frac{6 \cdot b}{A \cdot L \cdot c_0} \tag{7-11}$$

The uncertainty associated to D_e and a can be calculated by combining the relative errors on the individual parameters, a, b, L, S and c_0 (Van Loon and Soler, 2004), considering Equations (7-12) and (7-13):

$$\boldsymbol{u(D_e) = D_e \sqrt{(r.u.(a))^2 + (r.u.(L))^2 + (r.u.(A))^2 + (r.u.(c_0))^2}} \tag{7-12}$$

$$\boldsymbol{u(\alpha) = \alpha \sqrt{(r.u.(b))^2 + (r.u.(L))^2 + (r.u.(A))^2 + (r.u.(c_0))^2}} \tag{7-13}$$

In these equations, u stands for absolute error and *r.u.* is the relative uncertainty defined by the absolute error divided by the measured value. The uncertainty in the D_e value for all the samples (ETAPP1, ETAPP2, OPC micro-concrete, TAS05_09 and BMA) ranges between 0.07×10^{-12} and 0.18×10^{-12} m^2/s and for the capacity factor (accessible porosity) between 0.3 and 0.6.

When using Equation (7-4) for fitting the transient-state it should be considered that the error in each accumulated activity corresponds to the sum of each individual error, by calculating the square root of the sum of each square error. This way the first values present higher relative uncertainty, due to the fact that the activity is lower. This analysis was performed using the Root Data Analysis Framework (https://root.cern.ch/) with the experimental results from OPC-2 micro-concrete sample. The value obtained was $D_e = (8.46 \pm 0.03) \times 10^{-12}$ m^2/s and a porosity of 0.1876 ± 0.0003. In turn, the values obtained without uncertainty estimation in an Excel spreadsheet were $D_e = 8.49 \times 10^{-12}$ m^2/s and porosity 0.19.

The estimated accessible porosity for ETAPP1 and 2 resulted to be the highest among all tested specimens. Calculation of porosity values depends on the estimation of the time-lag value according to Equation (7-10), which is in turn the intercept of the straight line (steady-state) as expressed in Equation (7-9). It should be noted that different criteria with regards to the straight-line correlation factor will give rise to different time-lag values and, hence, to different porosity values.

In the authors' opinion, and considering the heterogeneity of the material, the best way of estimating the effective diffusion coefficient and the accessible porosity from these concrete samples is using the arithmetic mean of the results obtained from the same sample and with the same accurate methodology.

The mean values and associated uncertainties obtained from the HTO through-diffusion (TD) experiments carried out on the different types of concrete studied are shown in Table 7-7. It is noted that the accessible porosity values derived from this method (TD) may not represent accurate estimations when the time-lag value calculation is subject to changes (see e.g. Jakob et al. 1999).

Table 7-7. Summary of mean values from diffusion tests and the associated range of uncertainties.

Concrete/Sample	From steady-state		From transient-state	
	D_e (m²/s)	ϕ_{acc} (–)	D_e (m²/s)	ϕ_{acc} (–)
ETAPP1	$(5.86 \pm 0.56) \times 10^{-12}$	0.240 ± 0.03	$(5.85 \pm 0.45) \times 10^{-12}$	0.235 ± 0.015
ETAPP2	$(3.83 \pm 0.22) \times 10^{-12}$	0.195 ± 0.015	$(3.87 \pm 0.29) \times 10^{-12}$	0.200 ± 0.03
TAS05_09	$(4.69 \pm 0.12) \times 10^{-12}$	0.083 ± 0.02	$(4.88 \pm 0.12) \times 10^{-12}$	0.123 ± 0.015
OPC	$(8.02 \pm 0.63) \times 10^{-12}$	0.215 ± 0.01	$(7.89 \pm 0.60) \times 10^{-12}$	0.190 ± 0.01
BMA	$(9.30 \pm 0.32) \times 10^{-12}$	0.133 ± 0.02	$(9.38 \pm 0.28) \times 10^{-12}$	0.240 ± 0.03

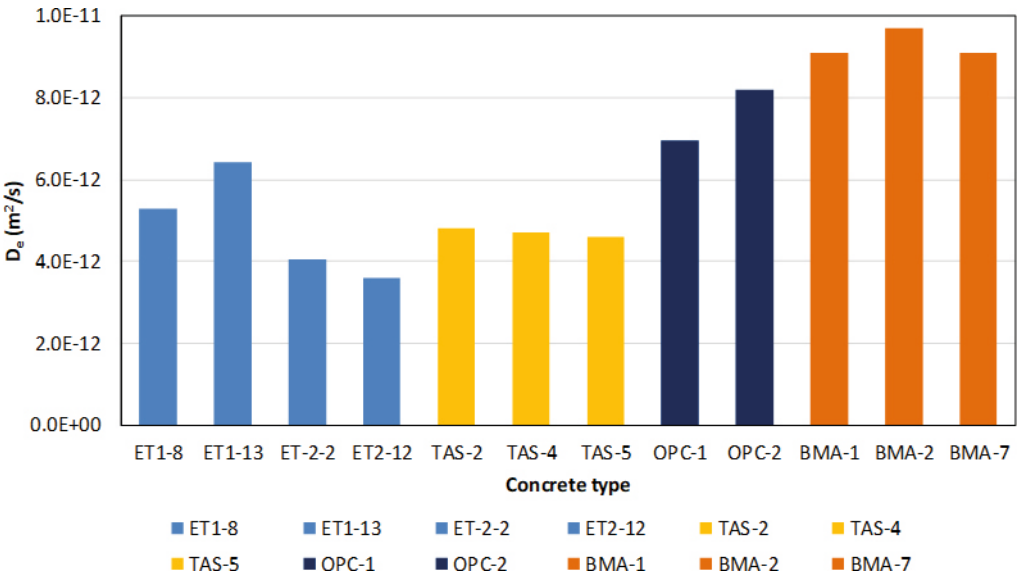

Figure 7-18. *Comparative chart of HTO effective diffusion coefficients obtained in the present study for ETAPP, TAS05_09, OPC micro-concrete and BMA samples.*

8 Concluding remarks

Different types of concrete of interest to SKB have been characterized in terms of physical and transport properties. Samples of limestone concrete (ETAPP1, ETAPP2, and TAS05_09) and OPC concrete (OPC micro-concrete and BMA) sent by SKB to CIEMAT laboratories in Madrid (Spain) were used in the experiments. Figure 8-1 shows a comparative plot of the averaged results from gas permeability, hydraulic conductivity, effective diffusion, and total porosity (calculated from dry and particle densities) of the samples.

There is some uncertainty associated with the particle (real) density with different values obtained for all the samples using two techniques, namely pycnometry using water and helium. The particle density, together with the dry density, are used to compute the porosity of the samples. The particle density obtained with water pycnometry was systematically higher than that obtained with helium pycnometry. However, chemical reactions probably take place during the determination of the particle density using water pycnometry, which may affect the accuracy of the measurement. The particle density was also computed at the end of the hydraulic conductivity tests assuming that the samples had a final degree of saturation of 100 % (due to the injection of water during long time periods). The values of particle density derived from these tests were considered as the most representative.

The hydraulic conductivity decreased with saturation time in all tested samples, until reaching a steady-state value upon equilibration of the system. This decrease is typically observed in water permeability tests and can plausibly be explained by the slow kinetics of saturation and by chemical reactions taking place during saturation, such as continued hydration (Hearn, 1998; Loosveldt et al. 2002; Villar et al. 2014). Hydraulic conductivity is also sensitive to temperature changes, increasing with it, which can be explained by the increase in water dynamic viscosity with temperature. Chen and Skoczylas (2010) also reported hydraulic conductivity values depending on temperature changes, with water permeability changes of about 25 % for temperature variations between 21 – 24 ºC.

A total of 12 through-diffusion tests were carried out in concrete samples using HTO as a conservative (i.e. non-reactive) tracer. The tests lasted between 114 and 165 days depending on the sample. The effective diffusion coefficient of the tracer was obtained under both transient- and steady-state conditions.

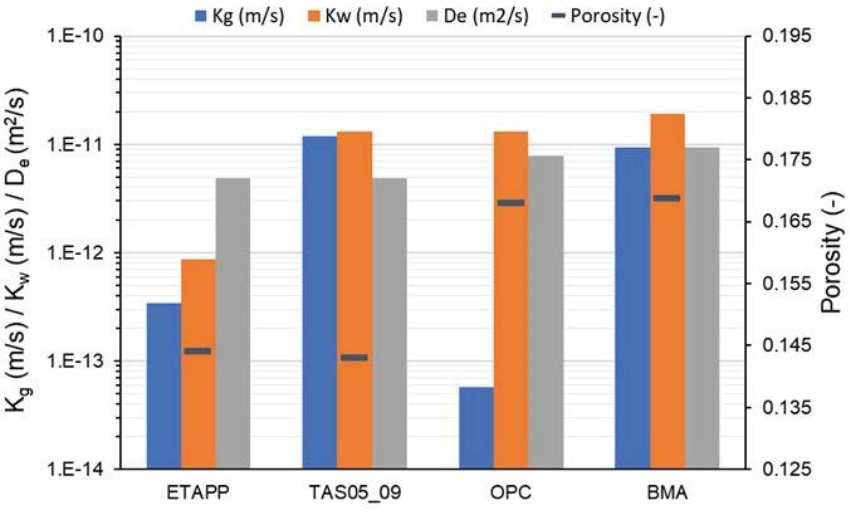

Figure 8-1. *Summary of averaged results from gas permeability (measured under confining pressures of 1.0 MPa for ETAPP and OPC and 0.8 MPa for TAS05_09 and BMA), hydraulic conductivity, effective diffusion (under transient regime) and porosity (right axis) of the concrete samples studied.*

8.1 Limestone concrete

The two ETAPP samples from the concrete cubes were similar in terms of dry density, although the water content of the ETAPP1 sample was higher. The pore size distribution of the ETAPP samples showed most of the pores with a pore size below 100 nm. Concerning the concrete core TAS05_09, the average bulk density was 2 420 kg/m^3, showing a homogeneous distribution along the sample core. This density was in the upper range of the bulk densities measured in the ETAPP concrete samples. The dry density tended to be higher towards the end of the core, corresponding to the inner part, whereas the water content was lower towards both ends. The lower water content at the ends correlates well with the lower ultrasound velocity measured there. The pore size distribution of the TAS05_09 core did not show significant differences between the four samples analysed, although a significant pore volume with pore sizes larger than 0.1 mm was measured. This is not common in concrete with limestone additions and could at least partly be attributed to the conditioning of the sub-samples.

Gas permeability tests of the ETAPP samples were carried out on the as-received water content states. Differences in measured gas permeability of these samples were not significant and could not be related to their density or degree of saturation variations between samples. Gas permeability of all ETAPP samples clearly decreased with the increase of confining pressure, more than one order of magnitude when the confining pressure increased from 0.6 to 2.5 MPa for an ETAPP2 specimen. The reason for this behaviour is still not fully clear. Other researchers also measured a decrease of gas permeability in dried concrete samples with increasing confining pressure and attributed it to closure of micro-cracks that were caused by the drying process (Meziani, 2006; Wu et al. 2013). However, the observed decrease was only of 20 % when increasing the pressure from 0.5 to 2 MPa. The existence of micro-cracks that could partially or totally close upon the effect of confining pressure does not seem likely in the present study, since the samples were tested immediately after being drilled, without allowing water content changes for the ETAPP samples (and also the OPC micro-concrete sample). On the other hand, gas flow along the sample/membrane interfaces cannot be ruled out, since the specimens presented uneven surfaces caused by the existence of air voids. Surface irregularities could partially impair the sealing function of the membrane allowing gas transport along the interface. The gas flow would decrease as the tightness of the interface was enhanced by the increase in confining pressure, which would result in the computation of lower permeability values.

For TAS05_09 concrete samples, a variation of the resulting effective gas permeability was observed with injection pressure. This fact can only be attributed to an insufficient flow increase to counteract such increase of injection pressure (Equation 5-3). The effective gas permeability of the quasi-dry samples (presumably close to the intrinsic permeability measured with air flow, k_{ig}) was at least an order of magnitude higher than the intrinsic permeability deduced from water flow, k_{iw}. This is in agreement with results in the literature (e.g. Loosveldt et al. 2002). This difference, along with the decrease of water permeability over time, suggests that the samples undertake some microstructural changes during water saturation. In general, results show higher gas permeability for the TAS05_09 compared to the ETAPP samples, as expected due to the preconditioning of the TAS05_09 samples by oven-drying at 60 ºC.

Results from through-diffusion (TD) tests using HTO as a tracer show that ETAPP and TAS05_09 samples have similar D_e values, although with different calculated accessible porosities. It is noted that the accessible porosities derived from through-diffusion tests may not represent accurate estimations when the time-lag value calculation is subject to changes (see e.g. Jakob et al. 1999). A more coherent relationship is found between the D_e and total porosity values calculated from dry and particle density values (Figure 8-1), showing an increase in D_e with increasing total porosity.

8.2 OPC concrete

The dry density of the OPC sample was clearly lower and its water content higher than the ETAPP samples. This OPC sample contained numerous voids in the surface, discernible to the naked eye. Its pore size distribution was also different to that of the ETAPP samples, being more homogeneous, whereas in the ETAPP samples most of the pores had a pore size below 100 nm. The ultrasound velocity measurements of block BMA showed a good internal homogeneity. However, the densities measured along the cylinder drilled showed some variability, with an overall bulk density of 2 370 kg/m^3 and a water content close to 6 %.

The comparison of the ultrasound velocity measurements between the two types of concrete (limestone concrete of TAS05_09 sample and OPC concrete of BMA sample) must be done taking into account the distance along which the measurements were performed, because smaller path lengths tend to give more variable and slightly lower pulse velocities. For similar measurement distances, the velocities obtained in the TAS05_09 core were higher than those obtained in the BMA block, which would indicate a higher strength of the first. This would be consistent with the concrete mix design of each sample. Also, the pore size distribution showed a lower average size of pores for the BMA than for the TAS05_09 concrete.

Gas permeability was measured in one OPC sample. Despite the fact of having lower dry density (and thus higher porosity) and lower degree of saturation, compared with the ETAPP samples, the OPC sample showed a gas permeability (for the same confining conditions) almost one order of magnitude lower than the other samples. As stated for the ETAPP samples, minimizing or eliminating gas flow across the membrane/sample interface could have a non-negligible impact on the gas permeability measurements. This would be consistent with the fact that the lowest gas flow was recorded for the OPC micro-concrete sample, with sealed surface irregularities.

For BMA concrete samples, a variation of the resulting effective gas permeability was observed with injection pressure, as with the TAS05_09 samples. The effective gas permeability of the quasi-dry samples was at least an order of magnitude higher than the intrinsic permeability deduced from water flow, k_{iw}. The results show higher gas permeability for the BMA samples compared to OPC micro-concrete samples, as expected due to the preconditioning of the BMA samples by oven-drying at 60 ºC.

Results from through-diffusion (TD) tests using HTO as a tracer show higher effective diffusion coefficients for the OPC-micro concrete and BMA samples compared to the limestone concrete samples. This trend is to be expected given the higher water-to-cement ratio of the OPC and BMA samples compared to the limestone concrete samples (i.e. 0.63 vs. 0.49, respectively). For OPC and BMA samples, the effective diffusion coefficient increase with increasing total porosity, similar to the case of the limestone concrete samples.

References

SKB's (Svensk Kärnbränslehantering AB) publications can be found at www.skb.com/publications.

Alcañiz-Martínez J, Louis-Cereceda M, Sánchez-Medrano F J, Lasheras-Estrella A, 2015. Estudio en estructuras de hormigón armado. Velocidad de ultrasonidos y resistencia a compresión. Revista Científica 21, 19–28. (In Spanish.)

Benachour Y, Davy C A, Skoczylas F, Houari H, 2008. Effect of a high calcite filler addition upon microstructural, mechanical, shrinkage and transport properties of a mortar. Cement and Concrete Research 38, 727–736.

Bourke P J, Jefferies N L, Lever D A, Lineham T R, 1993. Mass transfer mechanisms in compacted clays. In Manning D A C, Hall P L, Hughes C R (eds). Geochemistry of clay-pore fluid interactions. London: Chapman & Hall.

Chen W, Skoczylas F, 2010. Gas permeability of macro-cracked concrete: effect of temperature and water saturation. In 7th International Conference on Fracture Mechanics of Concrete and Concrete Structures, FraMCoS-7, Jeju, Korea, 23–28 May 2010.

Crank J, 1975. Mathematics of diffusion. 2nd ed. Oxford: Clarendon Press.

Descostes M, Blin V, Bazer-Bachi F, Meier P, Grenut B, Radwan J, Schlegel M L, Buschaert S, Coelho D, Tevissen E, 2008. Diffusion of anionic species in Callovo-Oxfordian argillites and Oxfordian limestones Meuse/Haute-Marne, France. Applied Geochemistry 23, 655–677.

Ellison S R L, Rösslein M, Willians A (eds), 2000. Quantifying uncertainty in analytical measurements. 2nd ed. EURACHEM/CITAC Guide CG 4.

Grathwohl P, 1998. Diffusion in natural porous media: contaminant transport, sorption/desorption and dissolution kinetics. Boston: Kluwer Academic Publishers.

Hearn N, 1998. Self-sealing, autogenous healings and continued hydration: What is the difference? Materials and Structures 31, 563–567.

Höglund L O, 2001. Project SAFE. Modelling of long-term concrete degradation processes in the Swedish SFR repository. SKB R-01-08, Svensk Kärnbränslehantering AB.

Jakob A, Sarott F-A, Spieler P, 1999. Diffusion and sorption on hardened cement pastes - experiments and modelling results. Waste Management Laboratory PSI-Bericht 99-05, Paul Scherrer Institut, Switzerland, Nagra NTB 99-06, Nagra, Switzerland.

Kumar R, Bhattacharjee B, 2003. Study on some factors affecting the results in the use of MIP method in concrete research. Cement and Concrete Research 33, 417–424.

Lagerblad B, Rogers P, Vogt C, Mårtensson P, 2017. Utveckling av konstruktionsbetong till kassunerna i 2BMA (Development of construction concrete for the caissons in 2BMA). SKB R-17-1, Svensk Kärnbränslehantering AB. (In Swedish.)

Laskar M A, Kumar R, Bhattacharjee B, 1997. Some aspects of evaluation of concrete through mercury intrusion porosimetry. Cement and Concrete Research 27, 93–105.

Lloret Morancho A, 1982. Comportamiento deformacional del suelo no saturado bajo condiciones drenadas y no drenadas. PhD thesis. Technical University of Catalonia. (In Spanish.)

Loosveldt H, Lafhaj Z, Skoczylas F, 2002. Experimental study of gas and liquid permeability of a mortar. Cement and Concrete Research 32, 1357–1363.

Ma H, 2014. Mercury intrusion porosimetry in concrete technology: tips in measurement, pore structure parameter acquisition and application. Journal of Porous Materials 21, 207–215.

Meziani H, 2006. Gas permeability measurements of cement-based materials under hydrostatic test conditions using a low-transient method. Magazine of Concrete Research 58, 489–503.

Meziani H, Skoczylas F, 1999. An experimental study of the mechanical behaviour of a mortar and of its permeability under deviatoric loading. Materials and Structures 32, 403–409.

Mårtensson P, Vogt C, 2019. Concrete caissons for 2BMA. Large scale testing of design and material. SKB TR-18-12, Svensk Kärnbränslehantering AB.

Scheidegger A E, 1974. The physics of flow through porous media. 3rd ed. Toronto: University of Toronto Press.

Sing K S W, Everett D H, Haul R AW, Moscou L, Pierotti R A, Rouquérol J, Siemieniewska T, 1985. Reporting physisorption data for gas/solid systems with special reference to the determination of surface area and porosity. Pure and Applied Chemistry 57, 603–619.

SKB, 2001. Project SAFE. Compilation of data for radionuclide transport analysis. SKB R-01-14, Svensk Kärnbränslehantering AB.

Taylor H F W, 1997. Cement chemistry. 2nd ed. London: Thomas Telford.

Thoma G J, Reible D D, Valsaraj K T, Thibodeaux L J, 1993. Efficiency of capping contaminated sediments in situ. 2. Mathematics of diffusion-adsorption in the capping layer. Environmental Science & Technology 27, 2412–2419.

Van Loon L R, Soler J M, 2004. Diffusion of HTO, 36Cl-, 125I- and 22Na+ in Opalinus Clay: effect of confining pressure, sample orientation, sample depth and temperature. PSI Bericht 04-03, Paul Scherrer Institut, Switzerland.

Van Loon L R, Soler J M, Bradbury M H, 2003. Diffusion of HTO, 36Cl- and 125I- in Opalinus Clay samples from Mont Terri: Effect of confining pressure. Journal of Contaminant Hydrology 61, 73–83.

Villar M V, Martín P L, Romero F J, Gutiérrez-Rodrigo V, Barcala J M, 2012. Gas and water permeability of concrete. Informes Técnicos CIEMAT 1261, Octubre 2012, CIEMAT, Spain.

Villar M V, Martín P L, Romero F J, Gutiérrez-Rodrigo V, Barcala J M, 2014. Gas and water permeability of concrete. Geological Society, London, Special Publications 415, 59–73.

Wesche K H, 1955. Möglichkeiten für die Anwendung von Ultraschall bei der Betonprüfung. Bautechnik 32, 151–155. (In German.)

Wu Z, Wong H S, Buenfeld N R, 2013. Effect of confining pressure on gaseous transport properties of concrete. In 33rd Cement & Concrete Science Conference, Portsmouth, UK, 2–3 September 2013.

Yoshimi Y, Osterberg J O, 1963. Compression of partially saturated cohesive soils. Journal of the Soil Mechanics and Foundations Division 89, 1–24.

Appendix A

ETAPP concrete

A1 ETAPP1 – Limestone concrete mix PSU-17 4 17/03/13

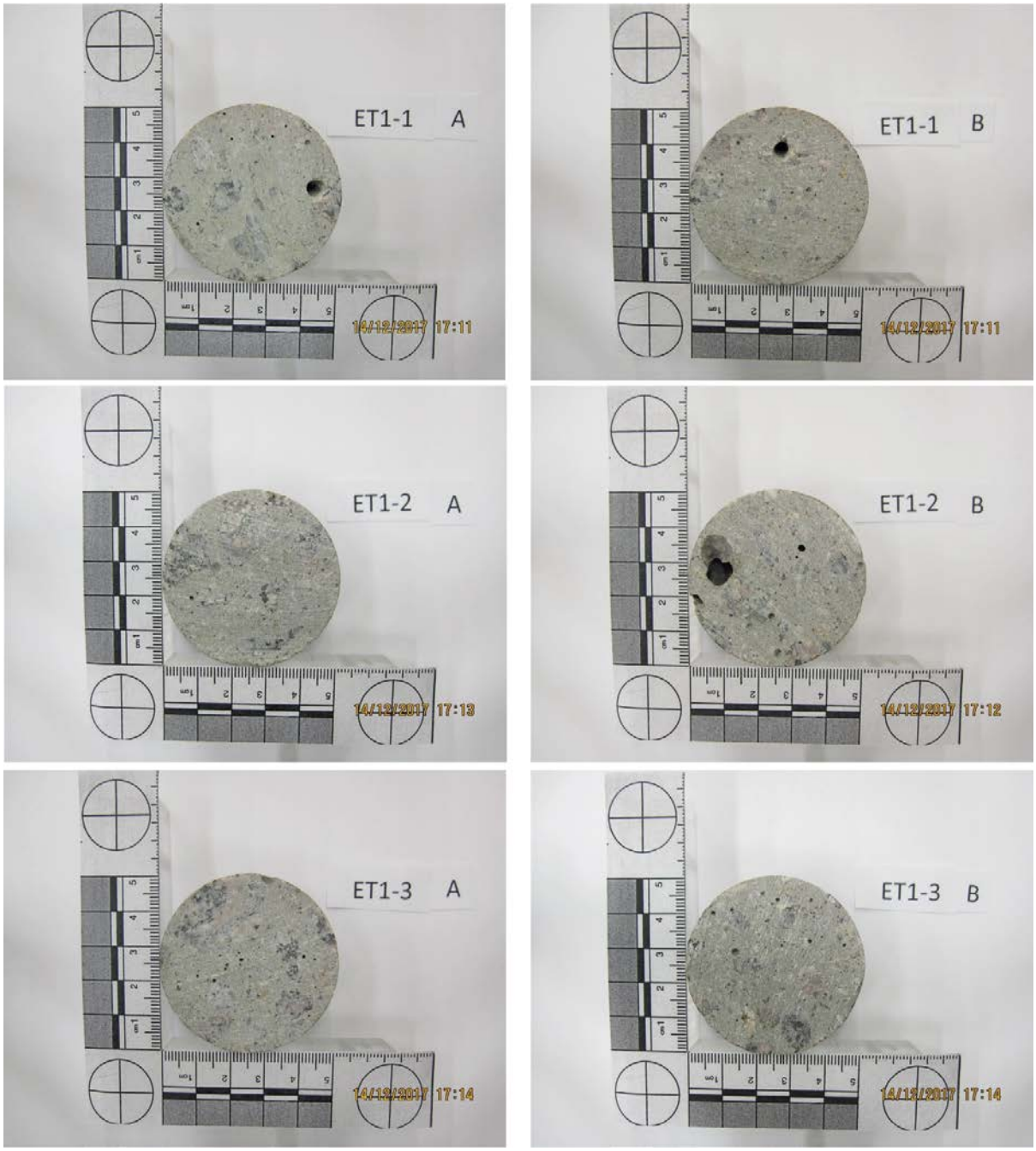

Figure A-1. *Aspect of ETAPP1 sub-samples (a and b labels stand for opposite sides of the same sample).*

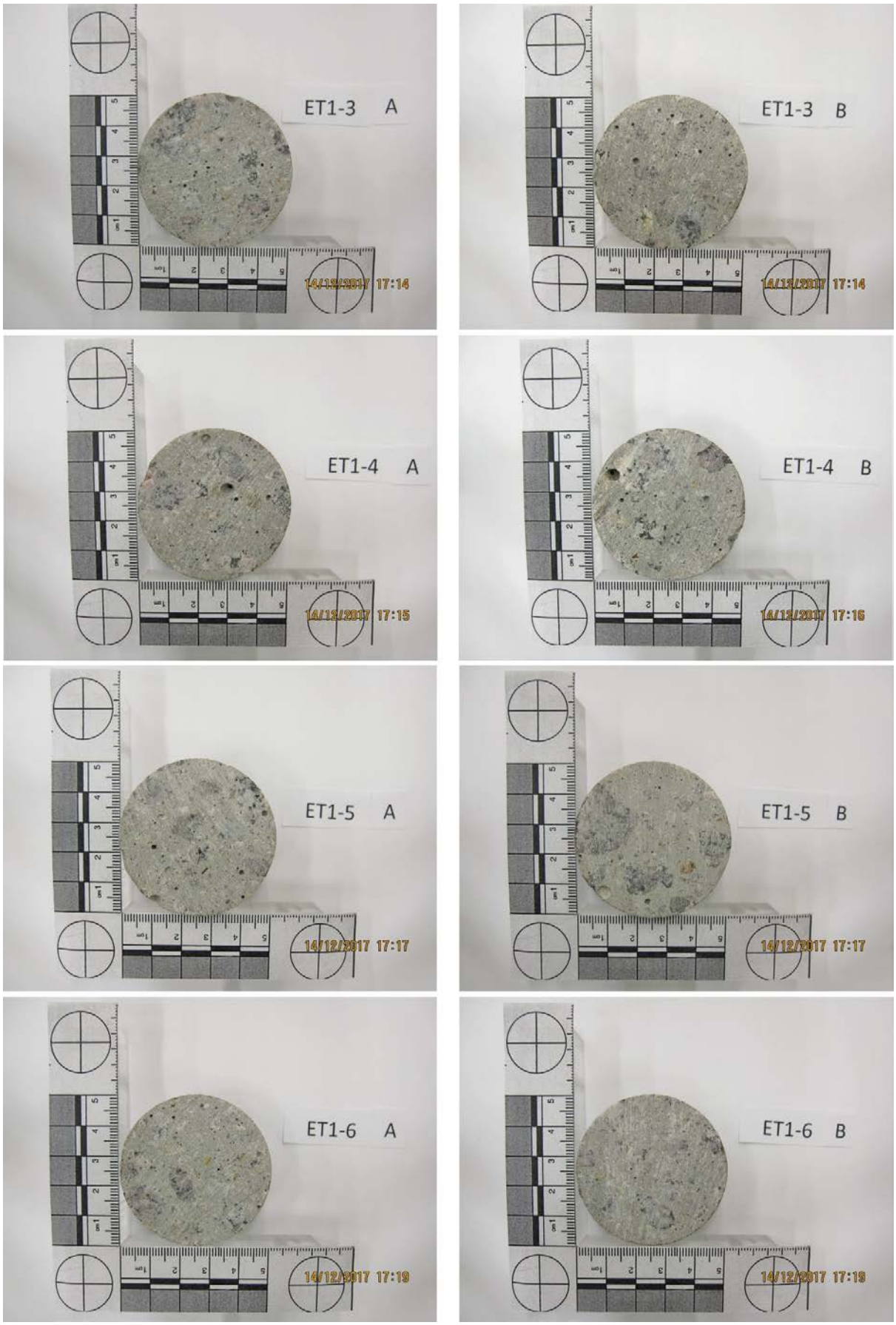

Figure A-1 forts. *Aspect of ETAPP1 sub-samples (a and b labels stand for opposite sides of the same sample).*

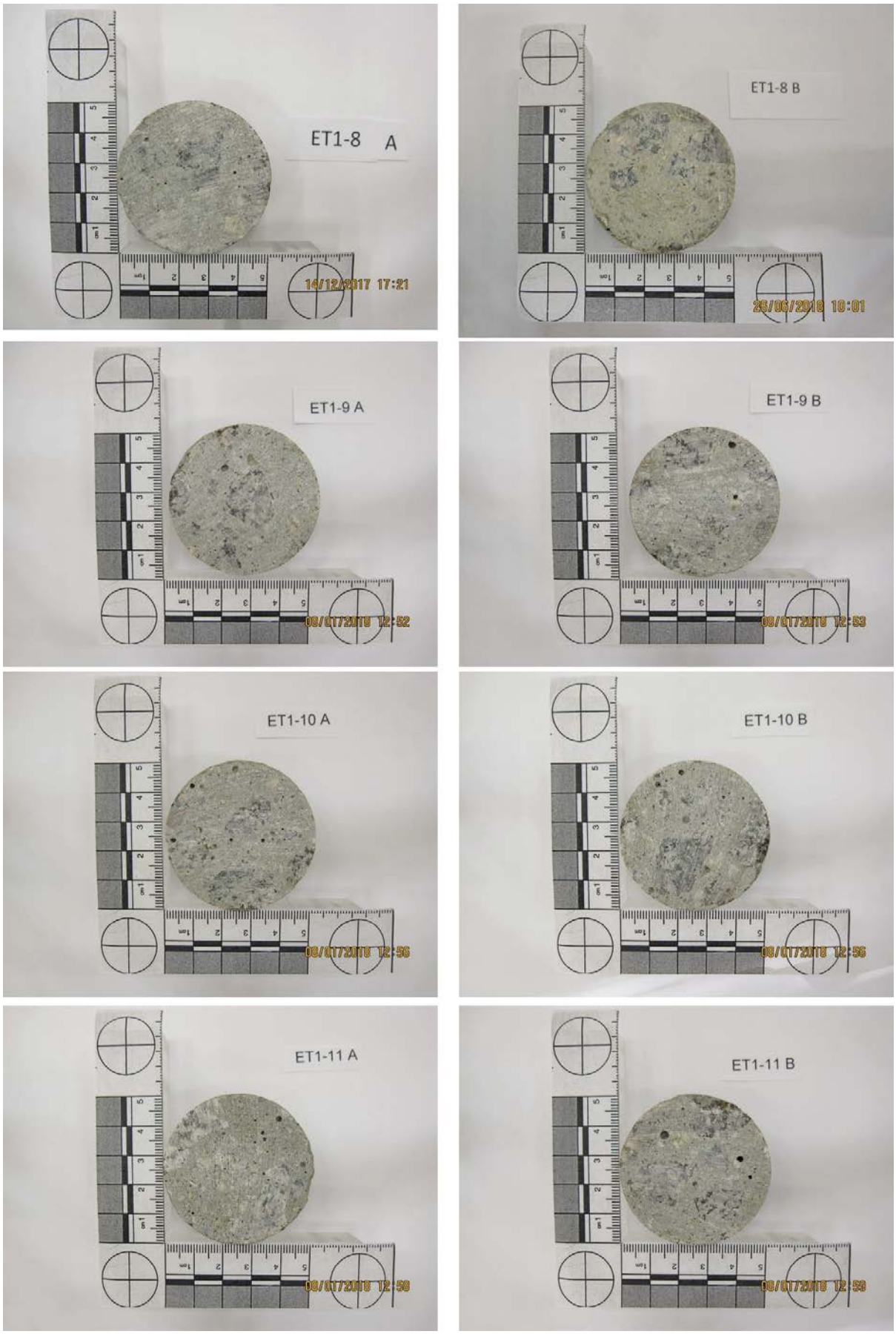

Figure A-1 forts. *Aspect of ETAPP1 sub-samples (a and b labels stand for opposite sides of the same sample).*

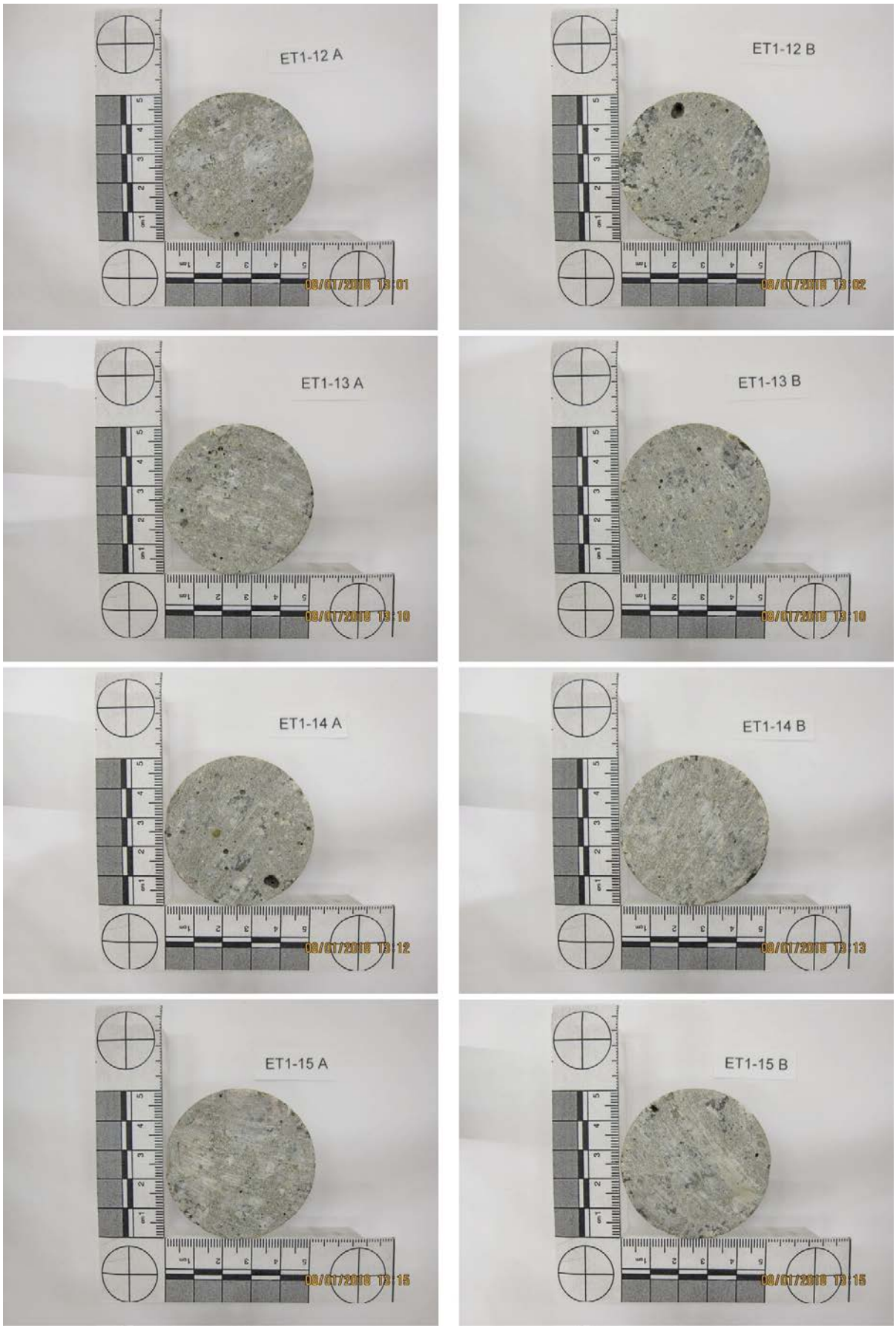

Figure A-1 forts. *Aspect of ETAPP1 sub-samples (a and b labels stand for opposite sides of the same sample).*

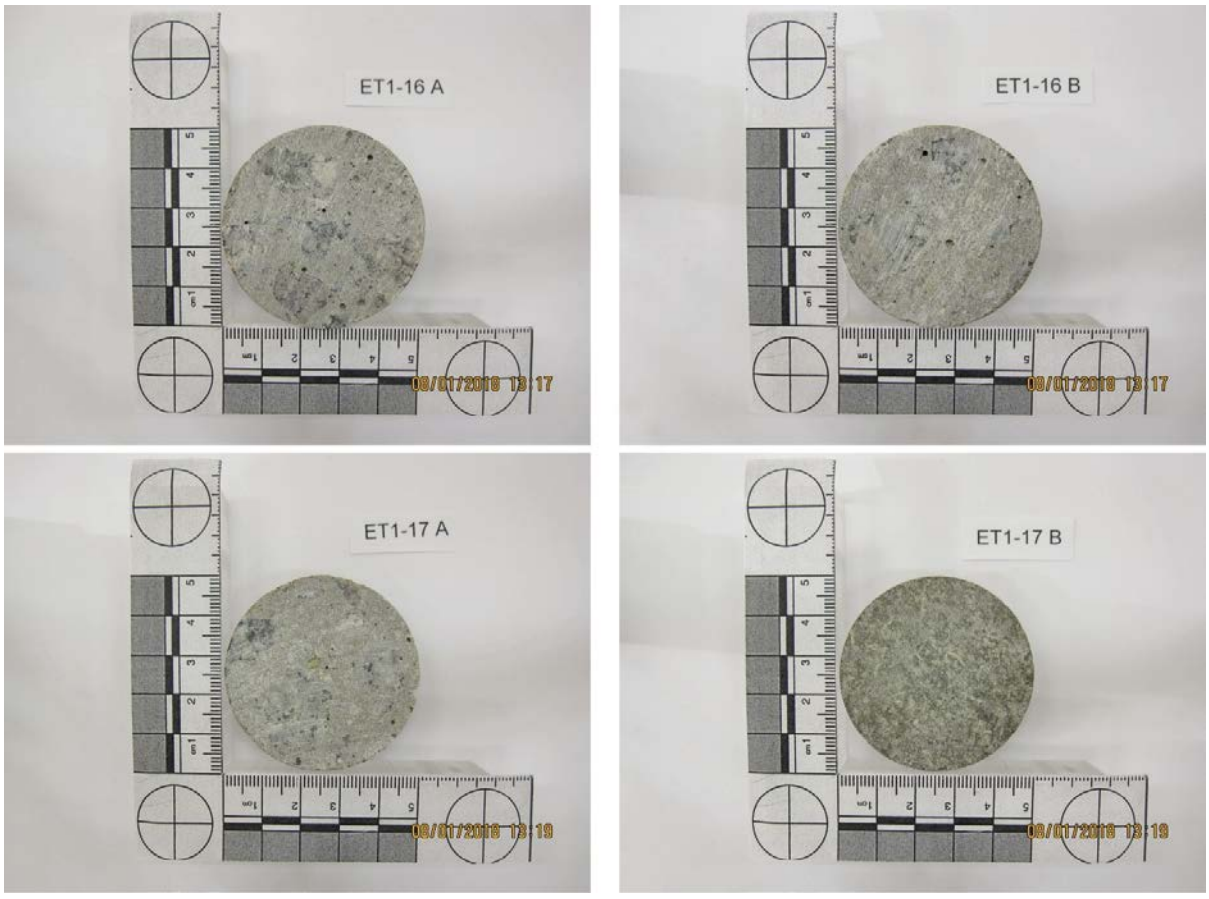

Figure A-1 forts. *Aspect of ETAPP1 sub-samples (a and b labels stand for opposite sides of the same sample).*

A2 ETAPP2 – Limestone concrete mix PSU-17. 4 17/05/03

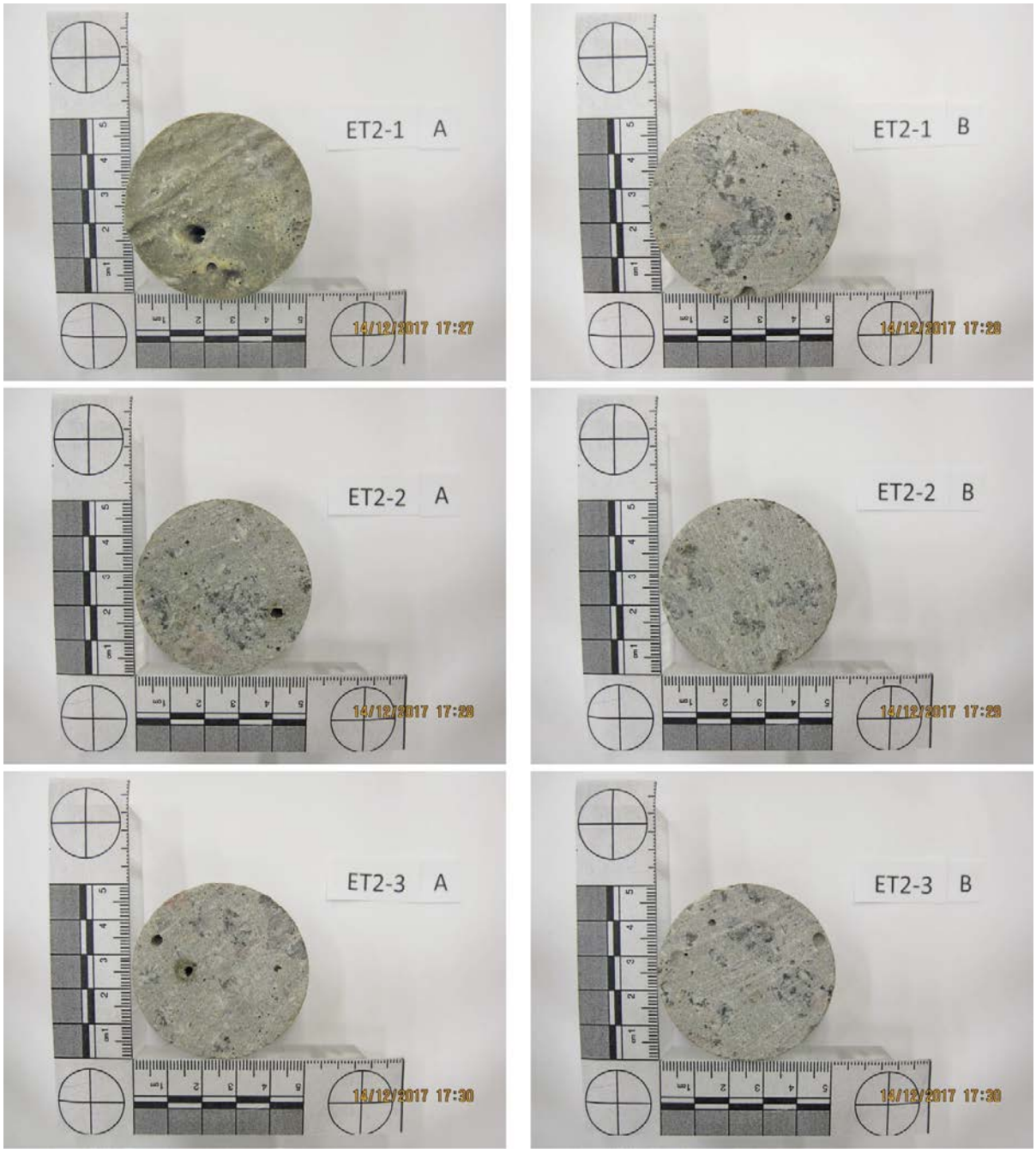

Figure A-2. *Aspect of ETAPP2 sub-samples (a and b labels stand for opposite sides of the same sample).*

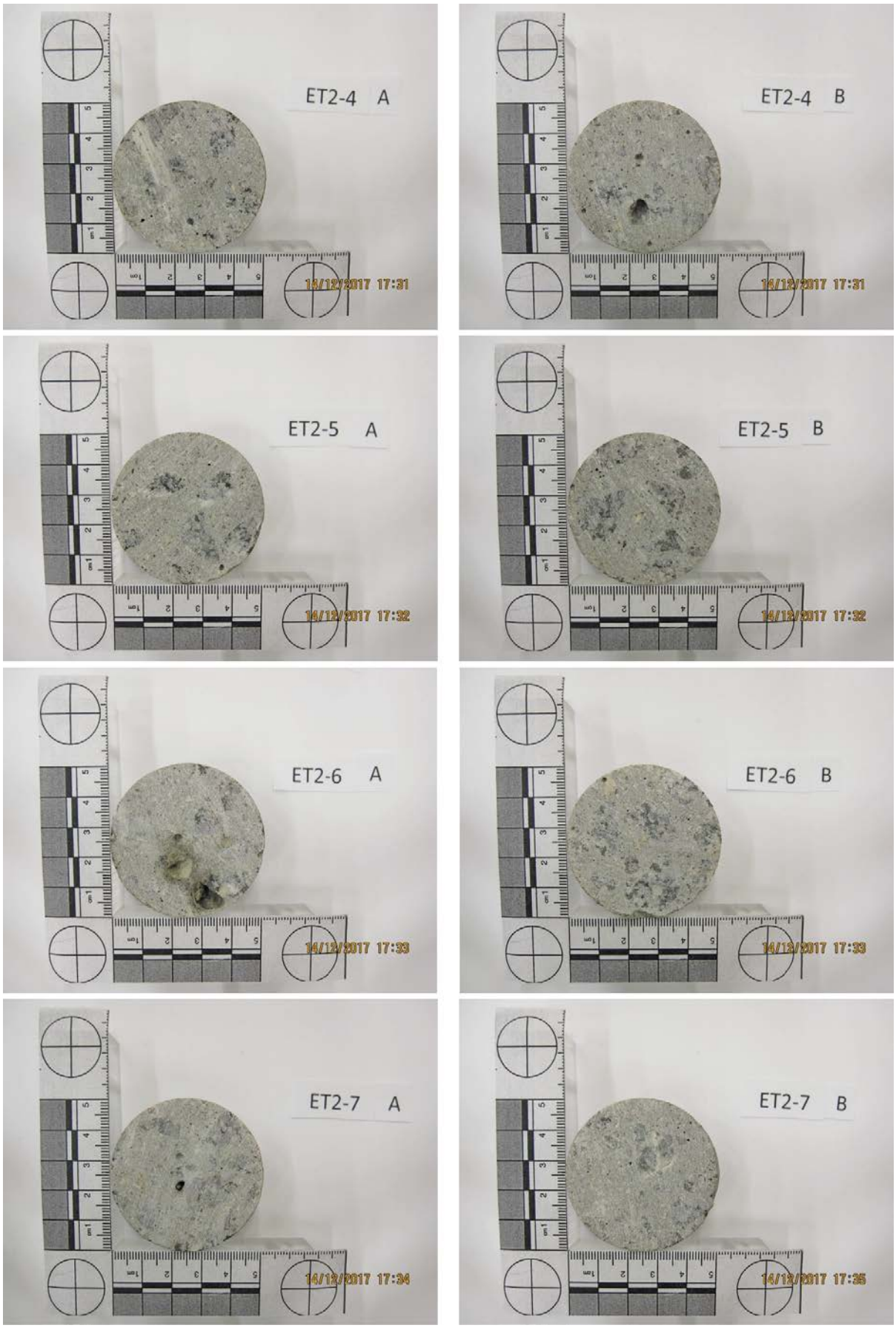

Figure A-2 forts. *Aspect of ETAPP2 sub-samples (a and b labels stand for opposite sides of the same sample).*

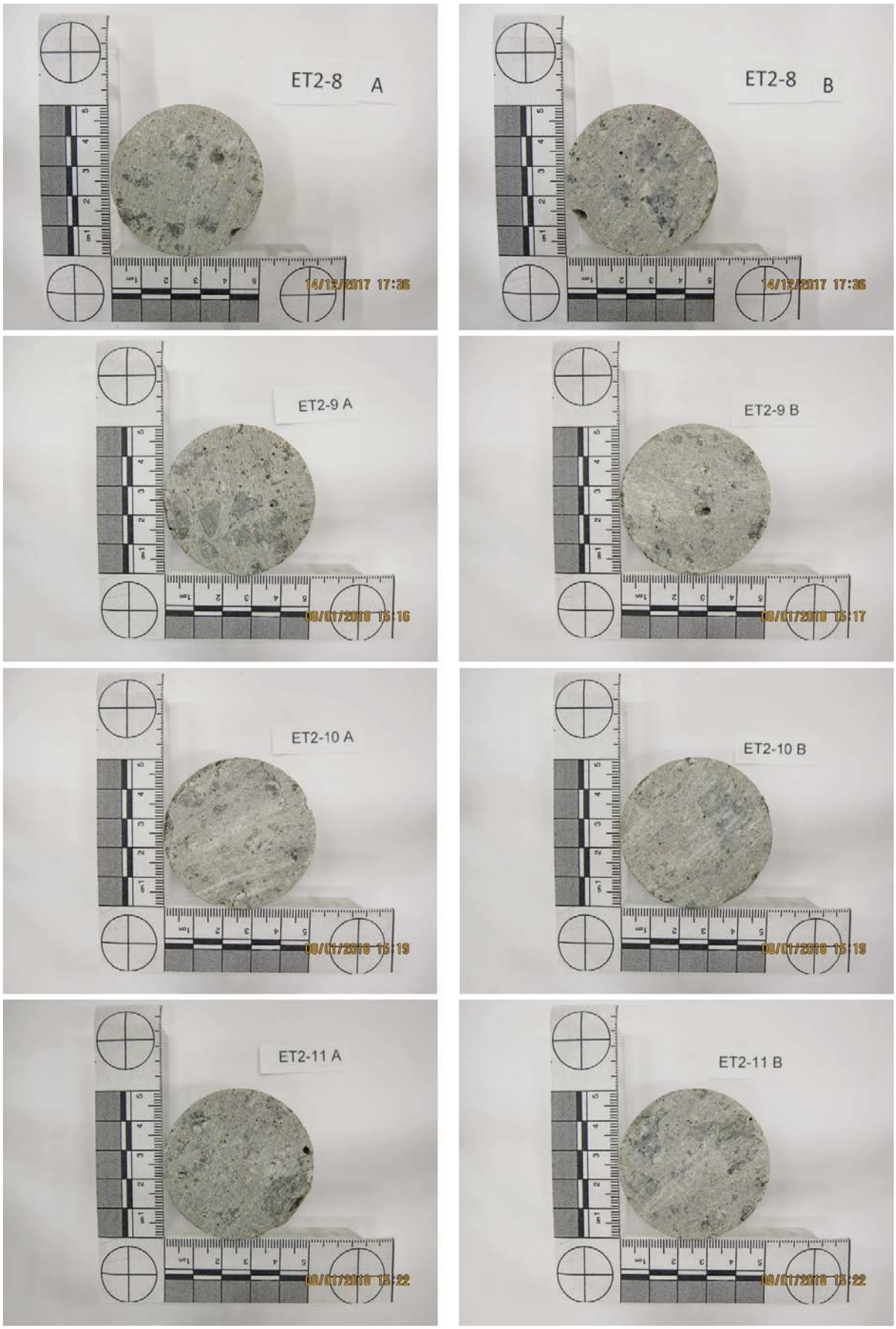

Figure A-2 forts. *Aspect of ETAPP2 sub-samples (a and b labels stand for opposite sides of the same sample).*

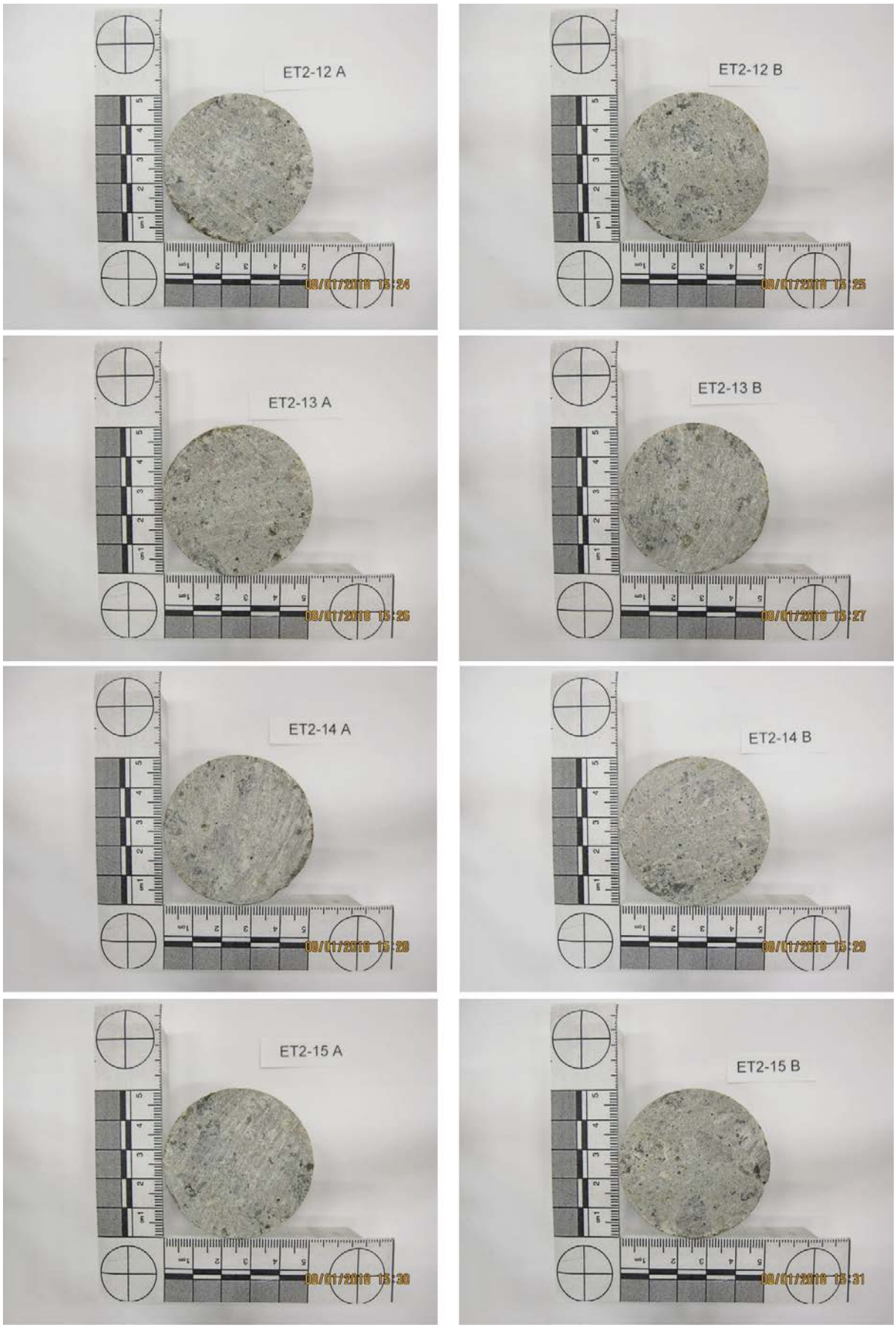

Figure A-2 forts. *Aspect of ETAPP2 sub-samples (a and b labels stand for opposite sides of the same sample).*

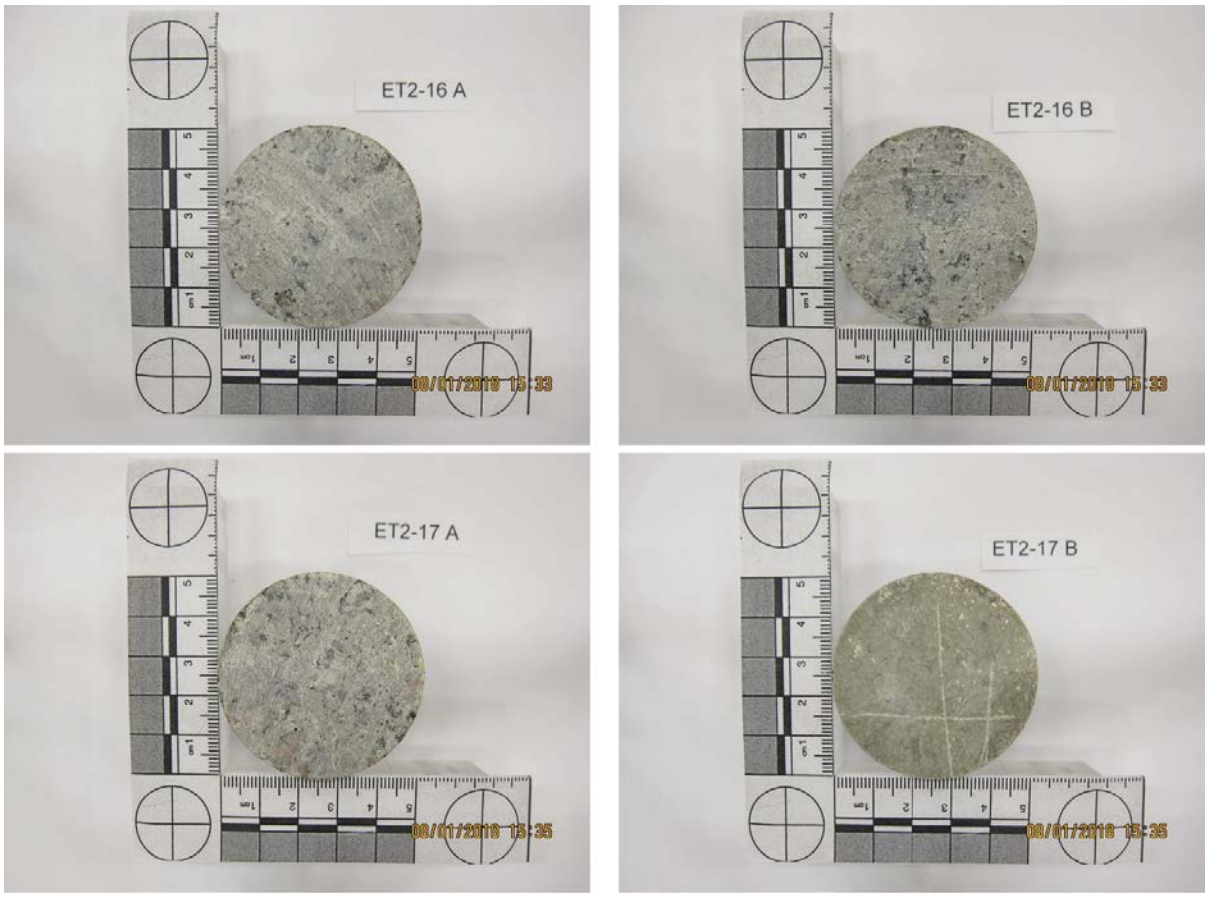

Figure A-2 forts. *Aspect of ETAPP2 sub-samples (a and b labels stand for opposite sides of the same sample).*

Appendix B

Micro-concrete OPC

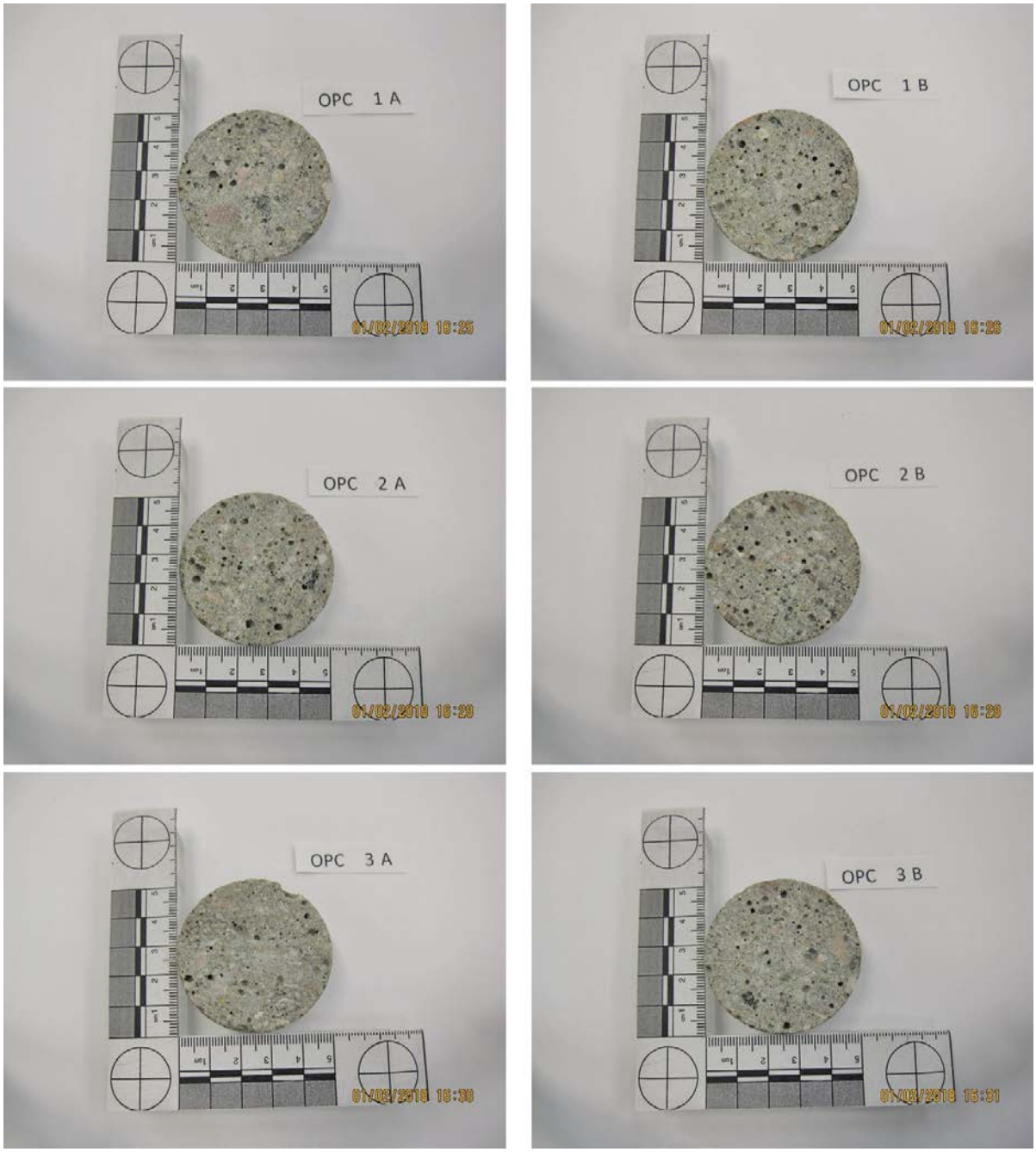

Figure B-1. *Aspect of OPC sub-samples (a and b labels stand for opposite sides of the same sample).*

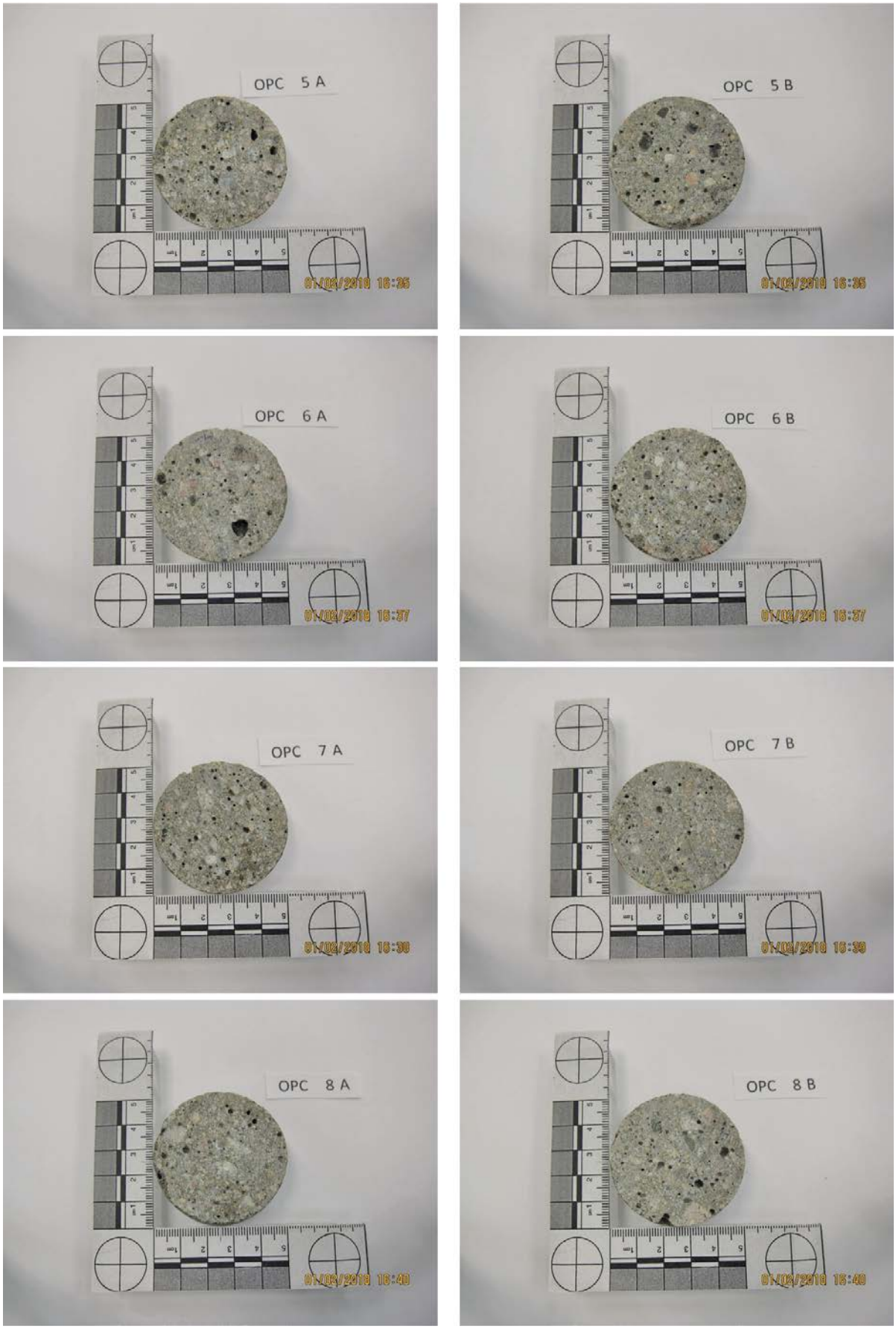

Figure B-1 forts. *Aspect of OPC sub-samples (a and b labels stand for opposite sides of the same sample).*

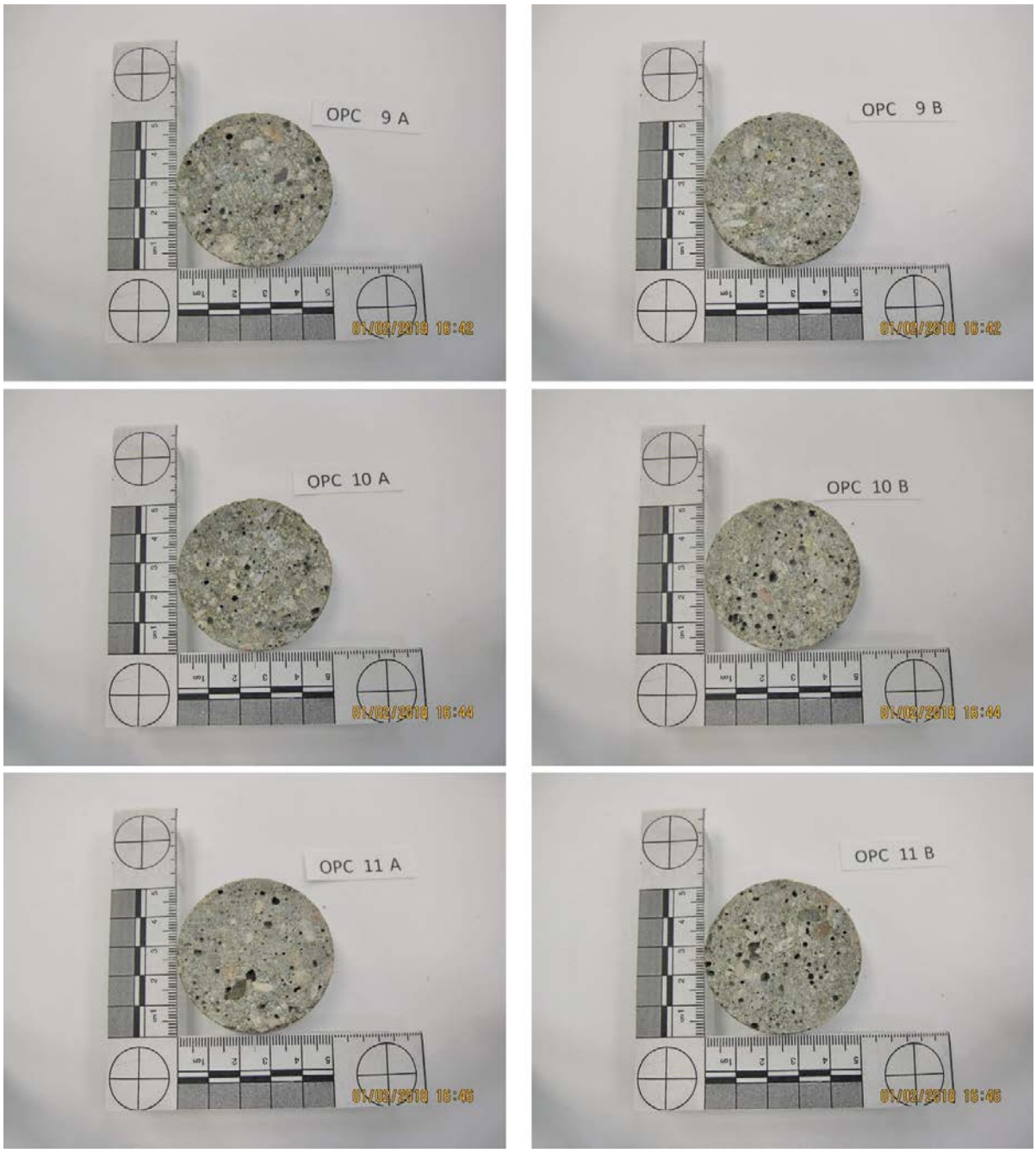

Figure B-1 forts. *Aspect of OPC sub-samples (a and b labels stand for opposite sides of the same sample).*

Appendix C

TAS05_09 concrete

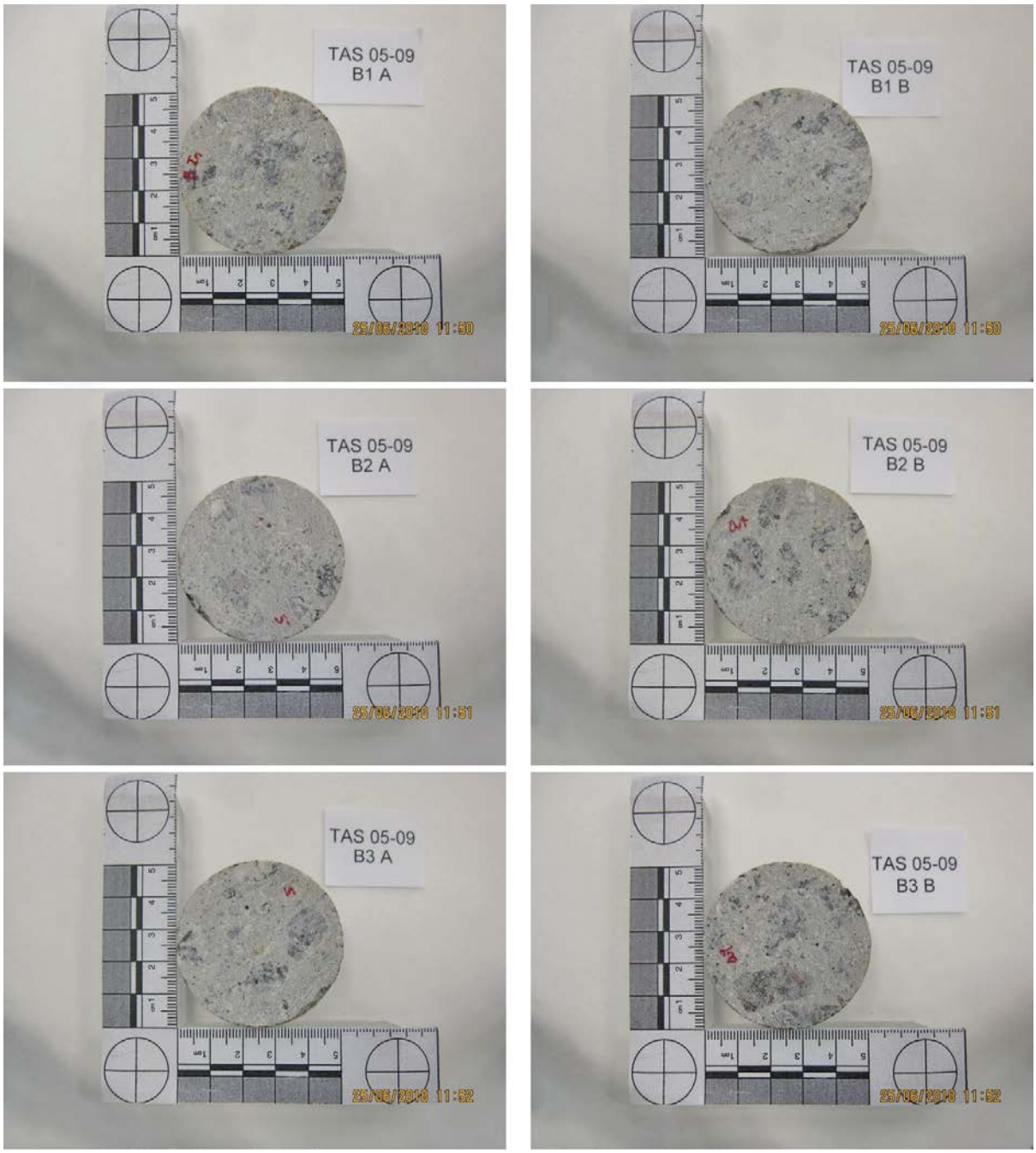

Figure C-1. *Aspect of TAS05_09 sub-samples (a and b labels stand for opposite sides of the same sample).*

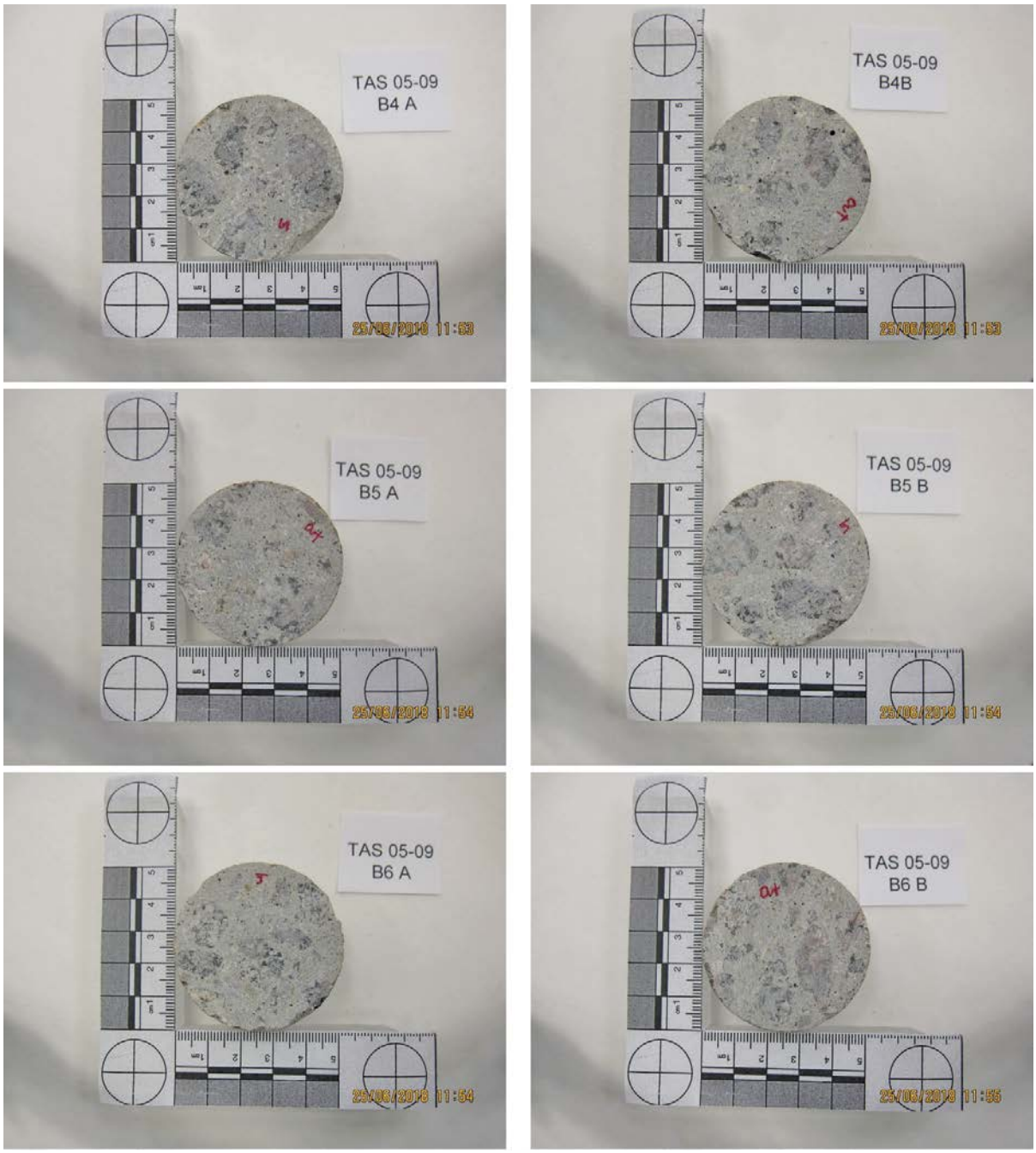

Figure C-1 forts. *Aspect of TAS05_09 sub-samples (a and b labels stand for opposite sides of the same sample).*

Appendix D

BMA concrete

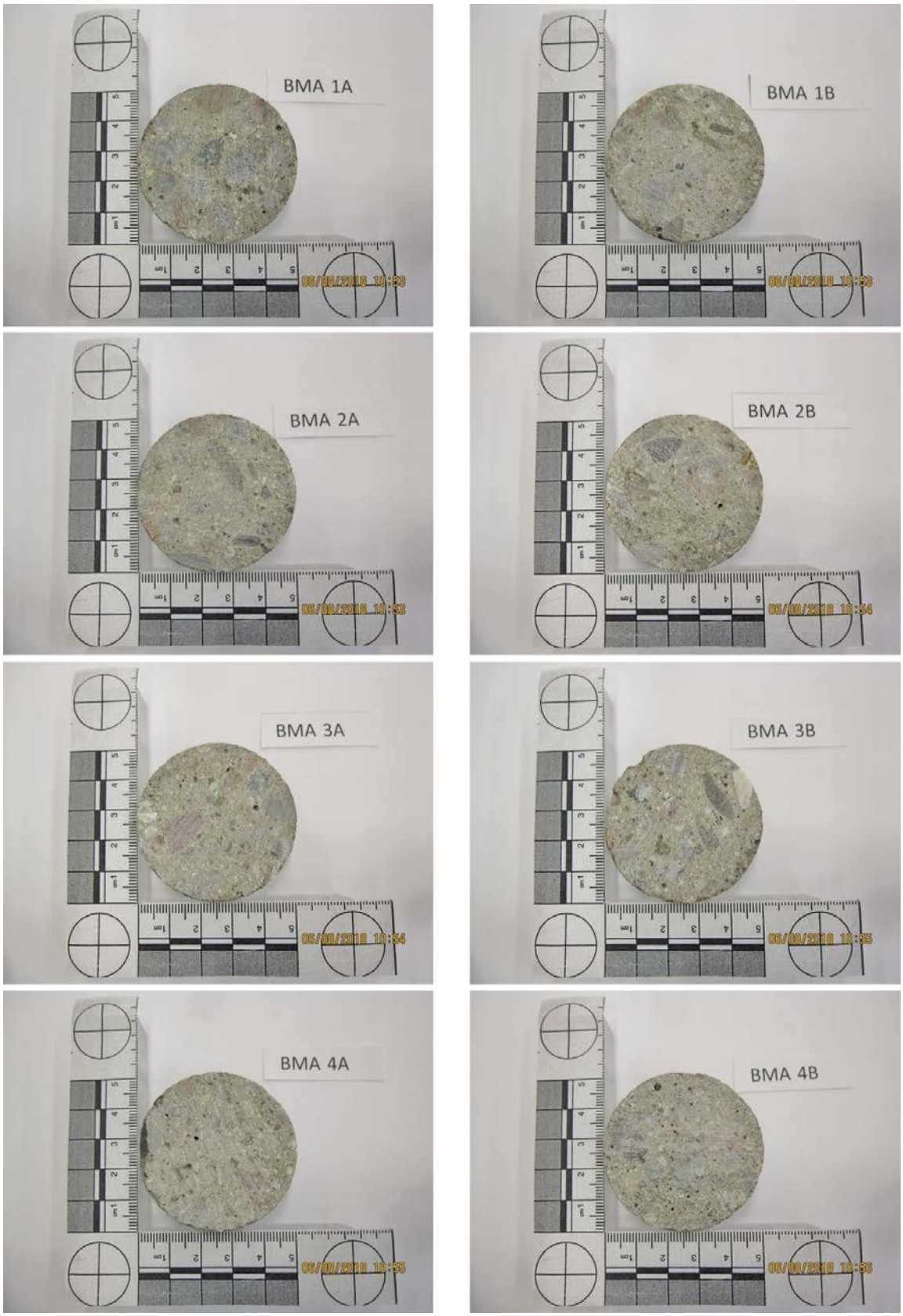

Figure D-1. *Sliced BMA sub-samples (a and b labels stand for opposite sides of the same sample).*

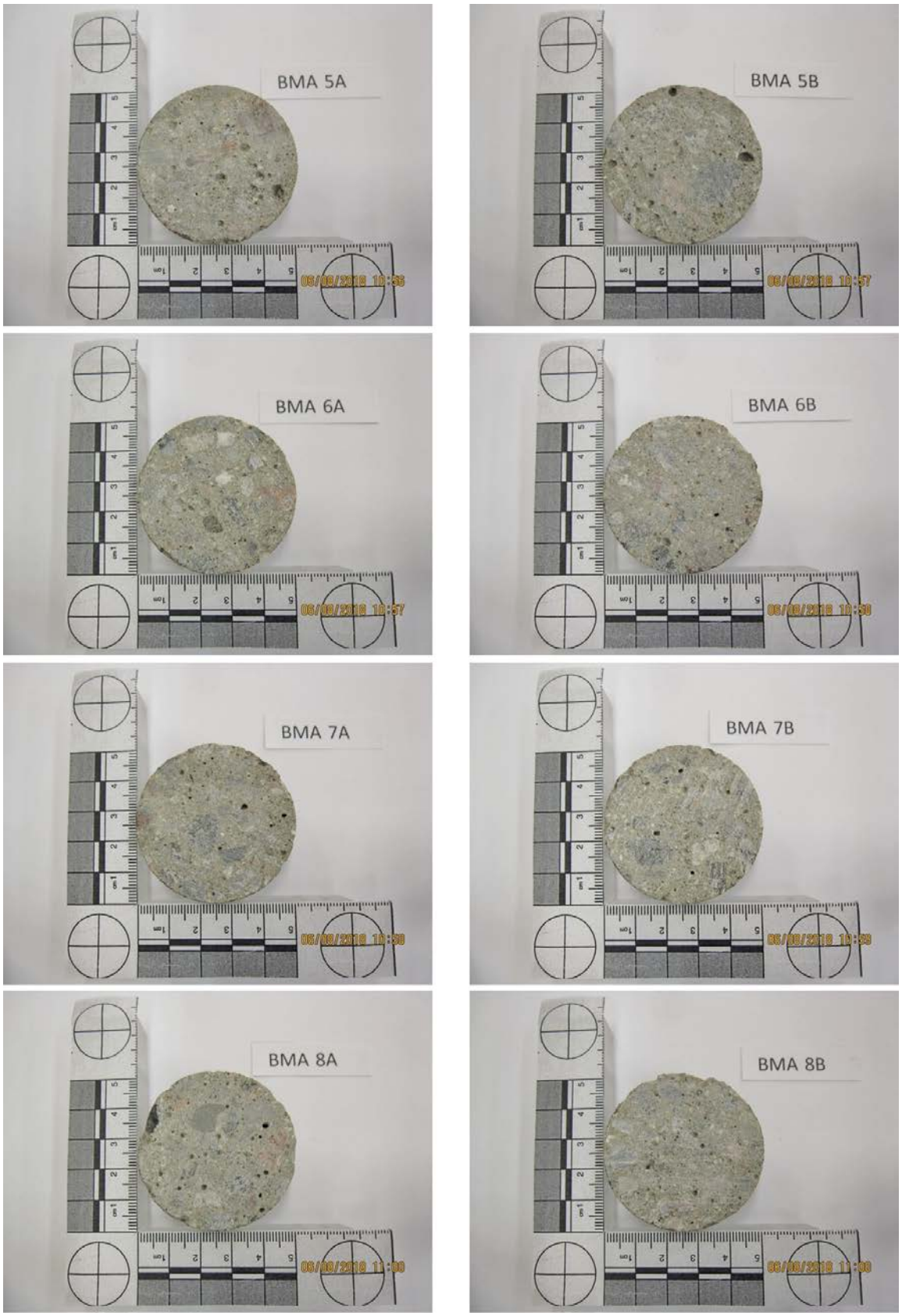

Figure D-1 forts. *Sliced BMA sub-samples (a and b labels stand for opposite sides of the same sample).*

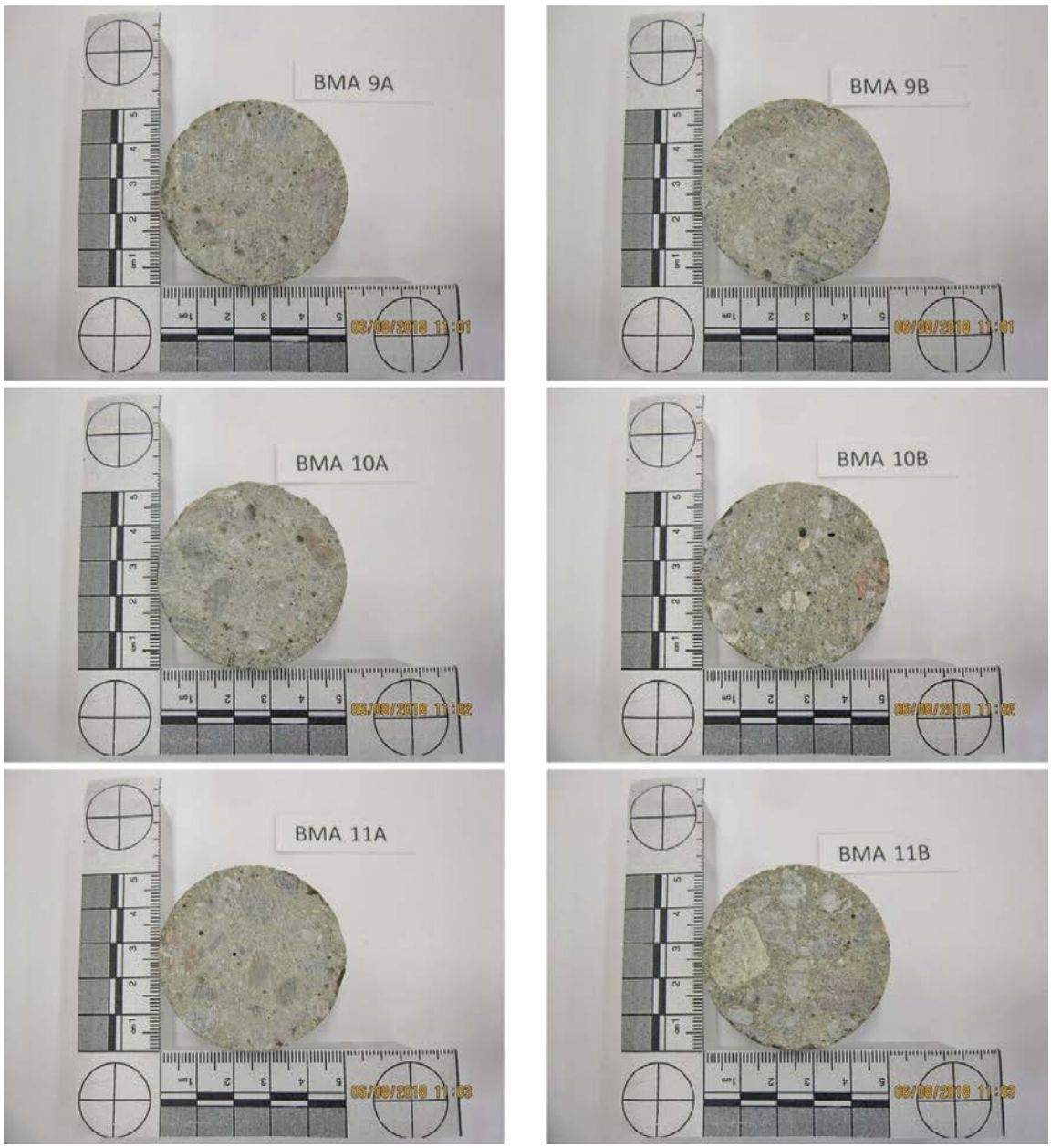

Figure D-1 forts. *Sliced BMA sub-samples (a and b labels stand for opposite sides of the same sample).*

Appendix E

Experimental data from diffusion tests

Table E-1. Experimental data for HTO TD experiments of ET1-8 and ET1-13 samples.

ET1-8			ET1-13		
Time (hour)	Flux ($cpm \cdot cm^{-2} \cdot h^{-1}$)	Cumulative mass (cpm)	Time (hour)	Flux ($cpm \cdot cm^{-2} \cdot h^{-1}$)	Cumulative mass (cpm)
0.00	0.00	0.00	0.00	0.00	0.00
24.00	0.00	0.00	75.33	0.00	0.00
48.00	0.00	0.00	243.25	0.00	0.32
72.00	0.00	0.00	411.25	0.03	104.90
144.00	0.00	0.00	579.25	0.10	449.43
220.50	0.01	9.60	747.25	0.14	934.79
387.50	0.03	106.29	915.25	0.18	1533.39
555.50	0.06	298.07	1083.25	0.18	2143.87
723.50	0.08	574.51	1246.75	0.18	2740.62
891.50	0.11	962.07	1414.75	0.18	3335.88
1059.50	0.13	1389.84	1583.00	0.18	3957.92
1227.50	0.14	1871.61	1751.00	0.19	4613.37
1395.50	0.14	2344.32	1919.00	0.20	5302.08
1563.50	0.15	2863.90	2087.00	0.19	5954.01
1727.00	0.16	3375.90	2255.00	0.20	6633.91
1895.00	0.14	3839.86	2423.00	0.20	7315.21
2063.25	0.14	4308.21	2591.00	0.21	8013.41
2231.25	0.15	4812.56	2759.00	0.20	8694.53
2399.25	0.15	5313.22	2927.00	0.20	9364.77
2567.25	0.15	5807.07			
2735.25	0.15	6307.04			
2903.25	0.16	6843.21			
3071.25	0.16	7374.04			
3239.25	0.16	7906.34			
3407.25	0.16	8431.92			

Table E-2. Experimental data for HTO TD experiments of ET2-2 and ET2-12 samples.

ET2-2			ET2-12		
Time (hour)	Flux ($cpm \cdot cm^{-2} \cdot h^{-1}$)	Cumulative mass (cpm)	Time (hour)	Flux ($cpm \cdot cm^{-2} \cdot h^{-1}$)	Cumulative mass (cpm)
0.00	0.00	0.00	0.00	0.00	0.00
51.75	0.00	1.84	51.25	0.00	0.00
218.75	0.00	5.10	219.25	0.00	9.30
386.75	0.01	55.27	387.33	0.02	92.05
554.75	0.04	189.77	555.25	0.05	262.11
722.83	0.07	438.31	723.33	0.07	486.26
890.75	0.08	709.13	891.33	0.08	752.84
1058.83	0.10	1046.63	1059.33	0.09	1054.46
1226.83	0.10	1392.06	1222.83	0.09	1334.13
1394.83	0.11	1762.36	1390.83	0.09	1626.92
1558.33	0.11	2119.24	1559.08	0.09	1933.96
1726.33	0.10	2473.66	1727.08	0.10	2281.27
1894.58	0.11	2859.60	1895.08	0.11	2656.88
2062.58	0.12	3252.52	2063.08	0.10	3006.85
2230.58	0.12	3663.03	2231.08	0.11	3364.58
2398.58	0.12	4057.04	2399.08	0.11	3744.30
2566.58	0.11	4440.80	2567.08	0.11	4103.52
2734.58	0.11	4828.67	2735.08	0.12	4501.49
2902.58	0.12	5246.20	2903.08	0.11	4884.44
3070.58	0.12	5643.67			
3238.58	0.12	6041.72			

Table E-3. Experimental data for HTO TD experiments of OPC-1 and OPC-2 samples.

OPC-1			OPC-2		
Time (hour)	Flux (cpm·cm^{-2}·h^{-1})	Cumulative mass (cpm)	Time (hour)	Flux (cpm·cm^{-2}·h^{-1})	Cumulative mass (cpm)
0.00	0.00	0.00	0.00	0.00	0.00
24.00	0.01	3.33	24.00	0.00	0.66
70.92	0.00	4.32	70.92	0.00	1.65
238.92	0.05	173.71	238.92	0.04	141.70
406.92	0.13	598.94	406.92	0.13	571.68
574.92	0.17	1159.09	574.92	0.18	1173.32
742.92	0.20	1840.21	742.92	0.22	1900.80
910.92	0.22	2574.66	910.92	0.23	2677.91
1078.92	0.22	3325.59	1078.92	0.24	3498.54
1246.92	0.22	4069.47	1246.92	0.24	4322.57
1414.92	0.22	4820.44	1414.92	0.24	5137.33
1582.92	0.22	5579.07	1582.92	0.24	5957.14
1750.92	0.23	6363.81	1750.92	0.25	6796.12
1918.92	0.22	7123.50	1918.92	0.24	7611.02
2086.92	0.23	7891.52	2086.92	0.25	8446.76
2278.92	0.23	8767.23	2278.92	0.24	9387.65
2447.00	0.23	9545.93	2447.00	0.25	10236.14
2615.00	0.23	10336.28	2615.00	0.25	11086.16
2783.00	0.23	11128.77	2783.00	0.25	11945.59
2951.00	0.23	11917.09	2951.00	0.26	12815.70
3119.00	0.24	12721.00	3119.00	0.25	13674.99
3287.00	0.24	13535.62	3287.00	0.25	14533.84
3455.00	0.24	14329.62	3455.00	0.25	15378.51
3623.00	0.23	15115.04	3623.00	0.26	16240.14
3791.00	0.23	15907.90	3791.00	0.26	17106.45
3959.00	0.23	16695.77	3959.00	0.26	17975.17

Table E-4. Experimental data for HTO experiments of TAS05_09 B2, B4 and B5 samples.

	B2		B4		B5	
Time (hour)	Flux (cpm·cm^{-2}·h^{-1})	Cum. mass (cpm)	Flux (cpm·cm^{-2}·h^{-1})	Cum. mass (cpm)	Flux (cpm·cm^{-2}·h^{-1})	Cum. mass (cpm)
0.00	0.00	0.00	0.00	0.00	0.00	0.00
96.75	0.00	8.21	0.01	22.24	0.01	15.95
264.75	0.02	80.44	0.03	128.69	0.03	114.27
432.75	0.07	325.43	0.08	402.97	0.06	329.54
600.75	0.10	669.82	0.11	775.19	0.13	783.31
768.75	0.14	1143.32	0.16	1306.73	0.14	1270.70
936.75	0.16	1671.99	0.16	1847.53	0.16	1803.18
1104.75	0.16	2210.65	0.15	2358.24	0.16	2342.36
1272.75	0.16	2764.49	0.16	2901.41	0.16	2891.23
1440.75	0.16	3302.25	0.15	3424.74	0.16	3434.65
1608.75	0.15	3811.64	0.14	3904.04	0.15	3943.81
1752.75	0.16	4273.76	0.14	4323.44	0.16	4412.92
1920.75	0.15	4775.51	0.14	4793.72	0.14	4895.97
2088.75	0.15	5266.03	0.15	5292.25	0.14	5365.31
2232.75	0.16	5728.85	0.15	5727.22	0.15	5802.07
2400.75	0.14	6205.92	0.14	6197.18	0.14	6263.32
2568.75	0.15	6706.34	0.15	6693.04	0.13	6716.62
2736.75	0.14	7190.87	0.15	7196.12	0.14	7198.27
2904.75	0.15	7714.07	0.16	7726.76	0.14	7678.47
3072.75	0.14	8188.92	0.14	8198.98	0.14	8146.37
3240.75	0.14	8664.78	0.15	8697.04	0.14	8614.51
3408.75	0.14	9147.58	0.15	9190.70	0.14	9079.10

Table E-5. Experimental data for HTO TD experiments of BMA samples.

	BMA 1		BMA 2		BMA 7	
Time (hour)	Flux ($cpm \cdot cm^{-2} \cdot h^{-1}$)	Cum. mass (cpm)	Flux ($cpm \cdot cm^{-2} \cdot h^{-1}$)	Cum. mass (cpm)	Flux ($cpm \cdot cm^{-2} \cdot h^{-1}$)	Cum. mass (cpm)
0.00	0.00	0.00	0.00	0.00	0.00	0.00
96.00	0.01	17.70	0.01	18.23	0.02	31.00
264.00	0.09	309.04	0.11	392.04	0.10	355.81
432.00	0.22	1047.12	0.23	1168.95	0.20	1024.10
600.00	0.26	1941.19	0.28	2108.74	0.26	1889.69
768.00	0.31	2977.37	0.31	3140.64	0.27	2789.28
936.00	0.29	3962.26	0.31	4198.23	0.27	3688.02
1080.00	0.30	4839.09	0.33	5157.81	0.29	4525.74
1248.00	0.28	5794.25	0.31	6215.59	0.27	5451.82
1416.00	0.28	6729.01	0.30	7226.21	0.26	6346.69
1560.00	0.30	7598.45	0.33	8179.35	0.29	7188.01
1728.00	0.27	8500.57	0.29	9163.18	0.25	8041.47
1896.00	0.27	9405.89	0.29	10151.09	0.28	9000.55
2064.00	0.28	10349.96	0.31	11184.92	0.28	9933.28
2232.00	0.28	11303.91	0.30	12188.52	0.28	10869.69
2400.00	0.26	12188.36	0.31	13226.03	0.28	11803.02
2568.00	0.27	13094.42	0.29	14198.86	0.27	12721.32
2736.00	0.26	13981.58	0.29	15171.83	0.27	13622.46

Arkitektkopia AB, Bromma, 2019

SKB is responsible for managing spent nuclear fuel and radioactive waste produced by the Swedish nuclear power plants such that man and the environment are protected in the near and distant future.

skb.se